

Metal-dielectric superlenses for ultraviolet and visible light

A dissertation

submitted to the Department of Photonics Engineering

at the Technical University of Denmark

in partial fulfillment of the requirements

for the degree of

philosophiae doctor

Rasmus Bundgaard Nielsen

December 31, 2010

Preface

This thesis is the product of my 3 years in the Department of Photonics Engineering at the Technical University of Denmark, from October 2007 to December 2010. The work was part of a larger research project called “On-Chip Nano-Imaging Using Superlens” (NanoMIUS), and started as a joint project between myself and Claus Jeppesen, a fellow PhD student, though our research later went down separate paths.

During these 3 years I have had the opportunity to work with a lot of brilliant and helpful people, who I will attempt to thank here. First and foremost I would like to thank my supervisors Jørn M. Hvam (DTU Fotonik), Anders Kristensen (DTU Nanotech) and Alexandra Boltasseva (DTU Fotonik and Purdue University) for their help, encouragement and advice during this work. I could not have done it without them.

I would to thank Claus Jeppesen (DTU Nanotech), who shared in this work at the beginning, was instrumental in achieving superlensing, and co-authored the first article with me.

I would also like to thank my many helpful colleagues at DTU Fotonik, Radu Malreanu in particular was of great help to me when it came to optical characterization, for which he graciously extended the use of his optical setup. I would also like to thank Andrei Lavrinenko for his help on the theory.

During my time as a PhD student I had the opportunity to spend 6 months at Purdue University, where I learned a lot, and met many interesting and intelligent people, who would later come to share in this work. I would like to thank Mark Thoreson who became a real friend, and provided invaluable expertise and aid. Paul West and Ji-young Kim who worked tirelessly helping me with the SNOM work, Zhengtong Liu who helped tremendously with the modeling, and Vladimir Shalaev who invited me into his group and shared his expertise.

I would like to thank the hardworking staff at Danchip, who were always there to help with the cleanroom equipment, and offer their suggestions for improvements, Valeriu Popescu and Peixiong Shi in particular.

And finally I owe a special debt of gratitude to my family and friends, without whom I would never have been able to complete this work.

This work was supported financially by The Danish Research Council for Technology and Production Sciences (grants no. 274-07-0057 and 274-07-0379).

Rasmus Bundgaard Nielsen

December 31, 2010

Abstract

This thesis describes a number of approaches towards improved superlensing, based on the use of single and multilayer silver lenses. These new designs offer the potential of improved resolution, along with the ability to tune the superlens operation wavelength.

A negative photoresist is used to capture the field distribution, when imaging a chrome grating with subwavelength features through a superlens. The results show that 80 nm resolution can be achieved with 365 nm light, which is well below the diffraction limit, thus validating the principle of near-field superlensing. The selection of materials for the superlens structure was based on suitability for lab-on-a-chip devices, and lead to the choice of chemically resist cyclo-olefin copolymers (Topas).

The use of a superlens to achieve near-field transfer of an optical hotspot was tested. Here a silver superlens was used to image the local field enhancement from an array of nanoantennas, and the results indicate a successful transfer, which opens up a number of applications for bio-, chemical- and medical-sensing applications, including surface enhanced Raman scattering and enhanced fluorescence.

The use of multilayer films to improve image quality is studied, and low roughness multilayer stacks consisting of silver and silicon dioxide were fabricated. However, problems with the underlying grating test structure led to inconclusive results.

Finally metal-dielectric composites were investigated to study their use as a superlensing layer, since their adjustable permittivity opens up the possibility of developing a superlens, that could be designed to work at any wavelength in the visible and near infrared. Various films were fabricated and characterized, with different materials, thicknesses and compositions, and the results show that the real part of the permittivity can indeed be tuned, as predicted by effective medium theory, but the loss is significantly higher than expected.

Resume

Denne afhandling beskriver en række forsøg på at opnå en forbedret superlinse. Forsøgene er baseret på brugen af enkelt og flerlags linser. Disse nye linsestrukturer gør det muligt at opnå bedre opløsning, og giver mulighed for at ændre hvilken bølglængde linsen skal fungere ved.

Et kromgitter med detaljer der er mindre end bølglængden bliver afbildet gennem en superlinse i en negativ resist. Resultaterne viser at 80 nm opløsning kan opnås ved en bølglængde på 365 nm, hvilket er et stykke under diffraktionsgrænsen, og dermed beviser at superlinseeffekten finder sted. Valget af materialer til superlinsen blev truffet med henblik på brug i lab-on-a-chip apparater, hvilket førte til brugen af polymeren Topas, som er meget kemisk modstandsdygtig.

Brugen af en superlinse til at overføre et kraftigt lokalt felt blev også afprøvet. Til dette formål blev en superlinse af sølv brugt til at overføre feltforstærkningen fra nanoantenner, og resultaterne indikerer en succesfuld overførsel, hvilket åbner op for en række muligheder inden for biologisk, kemisk og medicinsk diagnostik, inklusiv metoderne overfladeforstærket Raman-spredning og forstærket selvlysende effekt.

Brugen af flerlags linser til at forbedre billedkvaliteten bliver undersøgt, og det lykkes at fremstille en linse bestående af mange skiftende glas og sølv lag, der har meget lav overfladerugthed. Forsøget fik dog ikke nogen klar konklusion, da der var problemer med det lavere liggende gitterlag.

Endelig bliver en blanding af metal og dielektriske materialer også testet, for at undersøge muligheden for at bruge dem som superlinse materialer, da deres justerbare permittivitet åbner op for muligheden til at lave en superlinse, der kan bruges ved en vilkårlig bølglængde af synligt eller infrarødt lys. En række forskellige blandinger bliver fremstillet og afprøvet, med variation i valget af materialer, samt blandingsforholdet og den samlede tykkelse. Resultaterne viser at det ganske rigtigt kan lade sig gøre at ændre på den virkelige del af permittiviteten, sådan som teorien forudsiger, men at tabet er noget højere end forventet.

List of Publications

Journal Articles:

Michael G. Nielsen, Anders Pors, Rasmus B. Nielsen, Alexandra Boltasseva, Ole Albrektsen, Sergey I. Bozhevolnyi, "Demonstration of scattering suppression in retardation-based plasmonic nanoantennas," *Optics Express*, vol. 18, no. 14, pp. 14802-14811, 2010.

R. B. Nielsen, M. D. Thoreson, W. Chen, A. Kristensen, J. M. Hvam, V. M. Shalaev, A. Boltasseva, "Toward Superlensing with Metal-Dielectric Composites and Multilayers," *Applied Physics B*, vol. 100, no. 1, pp. 93-100, 2010.

C. Jeppesen, R. B. Nielsen, A. Boltasseva, S. Xiao, N. A. Mortensen, and A. Kristensen, "Thin film Ag superlens towards lab-on-a-chip integration," *Optics Express*, vol. 17, no. 25, pp. 22543-22552, 2009.

Conference contributions:

Rasmus B. Nielsen, Anders Kristensen, Jørn M. Hvam, Alexandra Boltasseva, "Metal-dielectric composites with tunable optical properties," *Proceedings of SPIE*, vol. 7711, p. 77111Q, 2010.

Claus Jeppesen, Rasmus B. Nielsen, Sanshui Xiao, Niels Asger Mortensen, Alexandra Boltasseva and Anders Kristensen, "An experimental investigation of Fang's Ag superlens suitable for integration," *Proceedings of SPIE*, vol. 7395, p. 73951I, 2009.

Contents

Preface	i
Abstract.....	iii
Resume.....	iv
List of Publications	v
List of Abbreviations	ix
Chapter 1 - Introduction.....	1
State of the Art.....	2
Project goals and methods	7
Thesis outline	9
Chapter 2 - Theory.....	11
Photonics.....	11
Diffraction limit	11
Plasmons	12
Near-field superlensing.....	14
Multilayer superlenses.....	17
Nanoantennas.....	18
Metal-Dielectric Composites	19
Fabrication	21
Ultraviolet Lithography	21
Electron-beam lithography	24
Reactive Ion Etching.....	27
Plasma Ashing	30

Physical Vapor Deposition	30
Electron-beam evaporation	31
Thermal evaporation	32
Sputtering.....	33
Lift-off.....	34
Characterization.....	35
Atomic Force Microscopy	35
Scanning Electron Microscopy	37
Energy Dispersive X-ray spectroscopy	39
Spectroscopic Ellipsometry	40
Scanning Near-field optical microscopy	42
Chapter 3 – Ultraviolet superlens.....	43
Key changes	43
Modeling	45
Pattern design	48
Fabrication scheme	50
Silver deposition	52
Substrate characterization.....	53
Exposure tests.....	55
AFM characterization.....	56
Chapter 4 - Near-field transfer of an optical hotspot	59
Superlens design	59
Pattern design	60
Structural characterization	62

Optical Characterization	65
Resonance shift	67
Near-field optical characterization	68
Chapter 5 - Metal-dielectric composites	75
Permittivity calculations	75
Fabrication method.....	78
Material choice	78
Fabrication details.....	80
Composition measurements.....	80
Film roughness	82
Optical characterization.....	84
Nanoantennas.....	86
Chapter 6 - Multilayer structures	89
Modeling	89
Multilayer fabrication	89
Planarization	90
Optical characterization.....	91
Chapter 7 - Conclusion	93
Outlook	94
Bibliography	97
Appendix A: Fabrication schemes.....	104
Ultraviolet superlens.....	104
Near-field transfer of optical hotspot.....	113
Appendix B: Comsol modeling.....	119

365 nm design	119
633 nm design	121
Appendix C: SNOM setups	123
Erlangen University setup	123
Purdue University setup	125

List of Abbreviations

AFM – Atomic Force Microscopy

APD – Avalanche Photo Diode

CVD – Chemical Vapor Deposition

DC – Direct Current

EBL – Electron-Beam Lithography

EDX – Energy Dispersive X-ray spectroscopy

EMT – Effective Medium Theory

FIB – Focused Ion Beam milling

FSL – Far-field Superlens

FWHM – Full Width Half Maximum

HMDS - Hexamethyldisilazane

MDC – Metal-Dielectric Composite

PMMA - Poly(methyl methacrylate)

PVD – Physical Vapor Deposition

QCM – Quartz Crystal Monitor

RF – Radio Frequency

RIE – Reactive Ion Etch

RMS – Root-Mean-Square

SCCM – Standard Cubic Centimeters per Minute

SEM – Scanning Electron Microscopy

SNOM – Scanning Nearfield Optical Microscope

SP – Surface Plasmon

UV – Ultraviolet

UVL – Ultraviolet Lithography

Chapter 1 - Introduction

The diffraction limit has traditionally been thought to impose a fundamental obstacle for optical imaging of nanoscale objects and molecules, but the emergence of a new class of materials is changing this paradigm. Metamaterials [1] are materials that have been artificially engineered to achieve properties not found in nature, an important example of which is negative refraction, which was first studied in 1968 by Veselago [2]. In the paper he showed that negative index is indeed possible, as long as the material exhibits both negative permittivity and negative permeability at a given wavelength. For a long time not much happened, since no such materials existed, but that changed in 2000 when Pendry proposed the superlens [3]. In his paper Pendry showed that it in the near-field only negative permittivity is required, and that such a material could be used to break the diffraction limit, and achieve deep sub-wavelength imaging. The design he proposed was based on the use of a single flat silver layer as the lens, a concept that was later realized by Fang et al [4] and nearly simultaneously Melville et al [5]. Both these designs use the silver lens in combination with a metallic mask, and demonstrate the improved resolution by imaging the subwavelength features of the mask onto a photoresist layer. Afterwards the exposed photoresist layer serves as a hardcopy of the light intensity distribution, and can be characterized with an atomic force microscope. With this technique Fang's group managed to resolve 60nm features using ultraviolet radiation at a vacuum wavelength of 365nm, a resolution of $\lambda/6$.

So far investigations have mainly focused on demonstrating sub-wavelength imaging capability [4] [5], and exploring the fundamental properties of negative index materials [6] [7], rather than developing actual applications for these devices. Such applications include improved optical microscopy [8] [9], ultraviolet lithography [5], surface enhanced Raman spectroscopy [10] [11] and the focusing of light for sensors or solar cells [12]. While many of the most promising potential applications are in the visible and near infrared, to date there have been few experimental demonstrations of superlensing in this range. This is due to the superlens matching condition [3], which requires that the permittivity of the lens be equal to minus the

permittivity of the surrounding layer. For dispersive materials this limits operation to a single wavelength, and for the commonly used silver/polymer combination, this wavelength is in the ultraviolet range.

In order to bring superlensing to the visible or infrared range, a number of solutions have been proposed, including the use of metal-dielectric composites (MDCs) [13] and multilayer lens structures [14] [15]. Using either MDCs or multiple layers as the superlens, makes it possible to tune the operational wavelength of the superlens, by selectively altering the volume ratio between metallic and dielectric components. Such tuning would take place prior to fabrication, and would not be dynamic, in the sense that the final device cannot be tuned, but it would enable superlens designs at any wavelength in the visible or near infrared spectrum.

State of the Art

Moving beyond the general introduction, this section will attempt to summarize the latest results in the field of negative index materials and subwavelength imaging. Since this is a very active research area, only a few examples will be given.

The best superlens resolution to date was achieved by Chaturvedi et al [16], when they successfully imaged a 30nm half-pitch grating with 380nm illumination ($\lambda/12$). They did so using a single 20nm silver layer, with a 1nm germanium adhesion layer to dramatically reduce roughness. The improved resolution was achieved in part by improving film quality, and in part by greatly reducing the distance between the object and image planes.

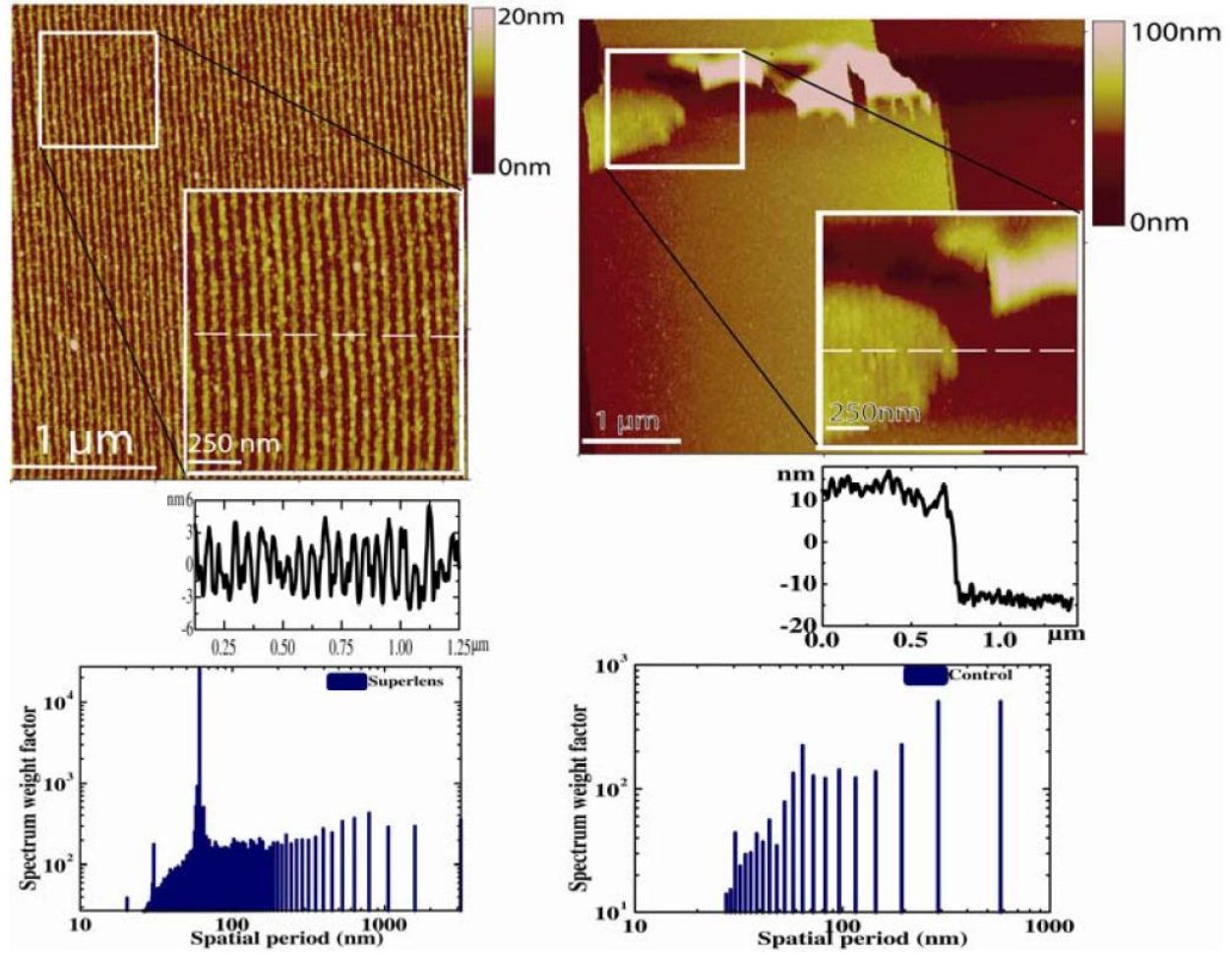


Figure 1. AFM scans of exposed photoresist with (top left) and without (top right) a superlens layer. Fourier analysis (bottom left and right) of the data shows that the lens successfully resolves the 30nm half pitch grating, while the control sample does not [16].

A different approach to superlensing was demonstrated by Taubner et al [17], who showed that SiC could serve as a superlens layer for infrared light, and achieved a resolution of 540 nm at 11 μm ($\lambda/20$). Rather than using a light sensitive material to detect the optical field, they chose to directly measure it with a scanning near-field optical microscope. In the experiment they used a gold mask layer with circular holes ranging from 540 to 1200nm in diameter, and a 440nm SiC lens layer covered on both sides by 220nm SiO₂ layers.

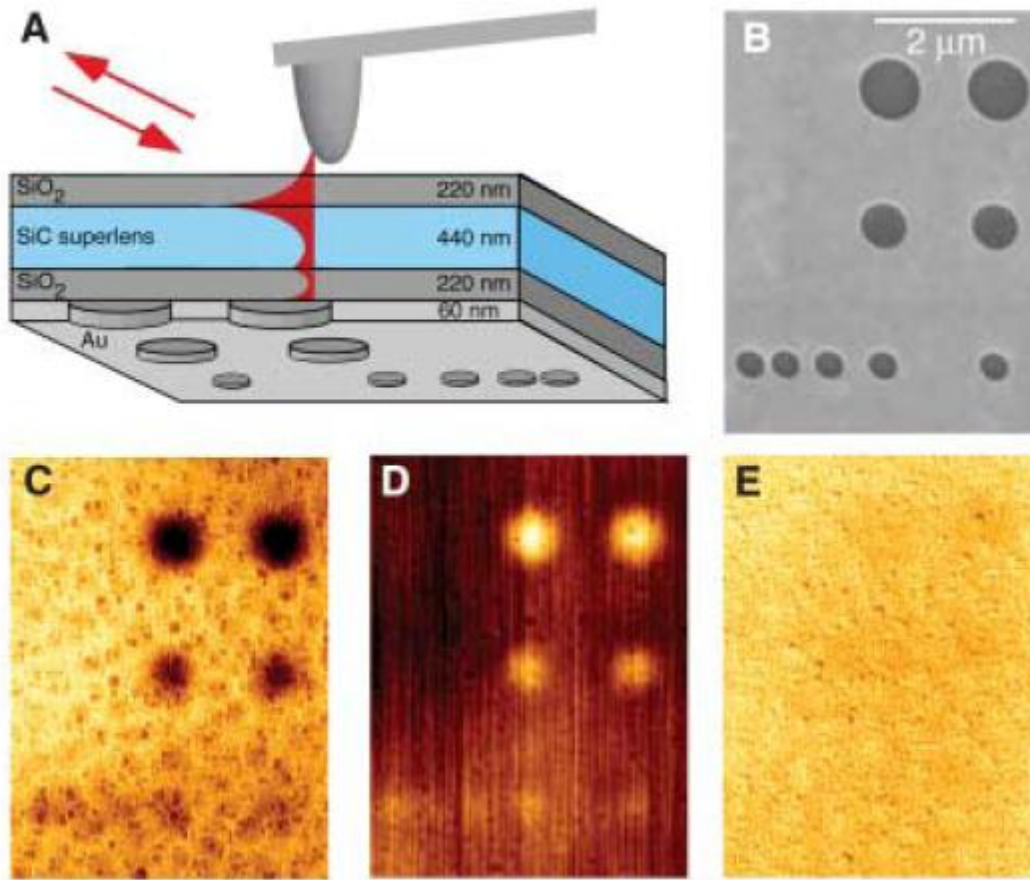


Figure 2. Near-field microscopy through an 880nm thick SiC/SiO₂ superlens: (A) Illustration of the experimental setup. (B) SEM image of the gold mask layer. (C) SNOM scan of the infrared amplitude at the image plane, taken at the resonance wavelength ($\lambda = 10.85 \mu\text{m}$). (D) Phase contrast at the image plane ($\lambda = 10.85 \mu\text{m}$). (E) Control image at an off-resonance wavelength ($\lambda = 9.25 \mu\text{m}$). [17]

In an attempt to move beyond the near-field, Liu et al [8] showed the first example of subwavelength resolution in the far-field. This was achieved by using a circular hyperlens consisting of alternating silver and alumina layer deposited on a circular groove in a quartz substrate. This geometry creates a highly anisotropic metamaterial with a hyperbolic dispersion, which causes evanescent waves to propagate along the radial direction, and effectively magnifies the image. The principle was validated experimentally by depositing a chrome layer on the inner surface of the lens, using focused ion beam milling to write a pattern in the chrome layer, shining light through the lens, and capturing the output signal with an

ordinary optical microscope. The results show, that a pair of 35nm wide lines spaced 150nm apart could be clearly resolved with the lens, while they blur into a single line without the lens.

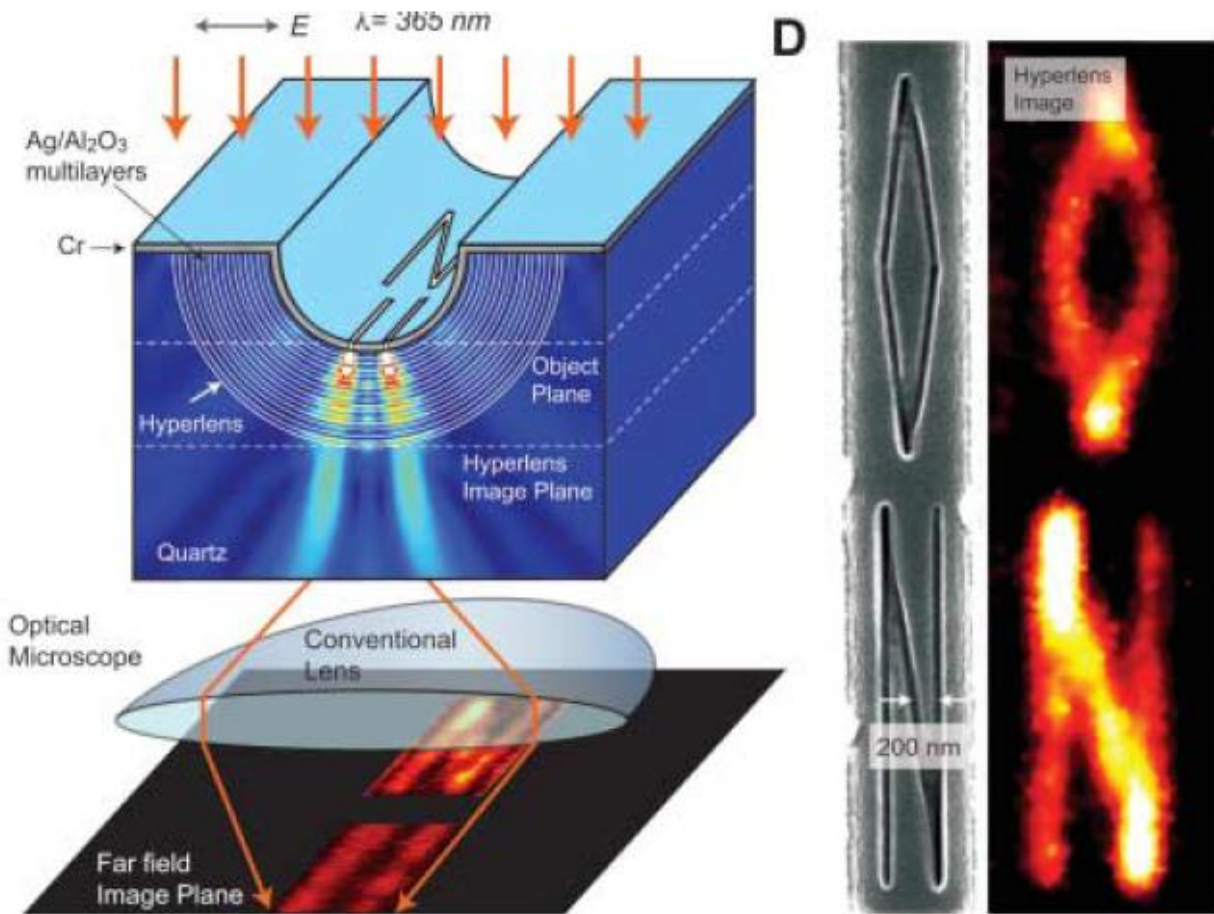


Figure 3. Illustration of a magnifying optical hyperlens, showing the experimental setup (left) and the hyperlens image (right). Alternating silver and alumina layer deposited on a semicircular groove magnify the image created by shining UV light through slits in a chrome mask layer. [8]

Later on Liu et al [9] demonstrated a new far-field superlens (FSL) design with improved resolution. This design consists of a thin silver film with a surface grating on the output plane. As in a normal silver slab superlens, the evanescent waves are enhanced inside the lens, and then converted into propagating waves by the periodic grating. The propagating waves can then be detected in the far-field, and the image can be reconstructed including the necessary subwavelength information. Using this setup they were able to distinguish two 50nm lines spaced 77nm apart. This new flat design has a key advantage: It can magnify any spot within a

relatively large area, unlike the previous circular design which can only image objects placed at the center of the groove.

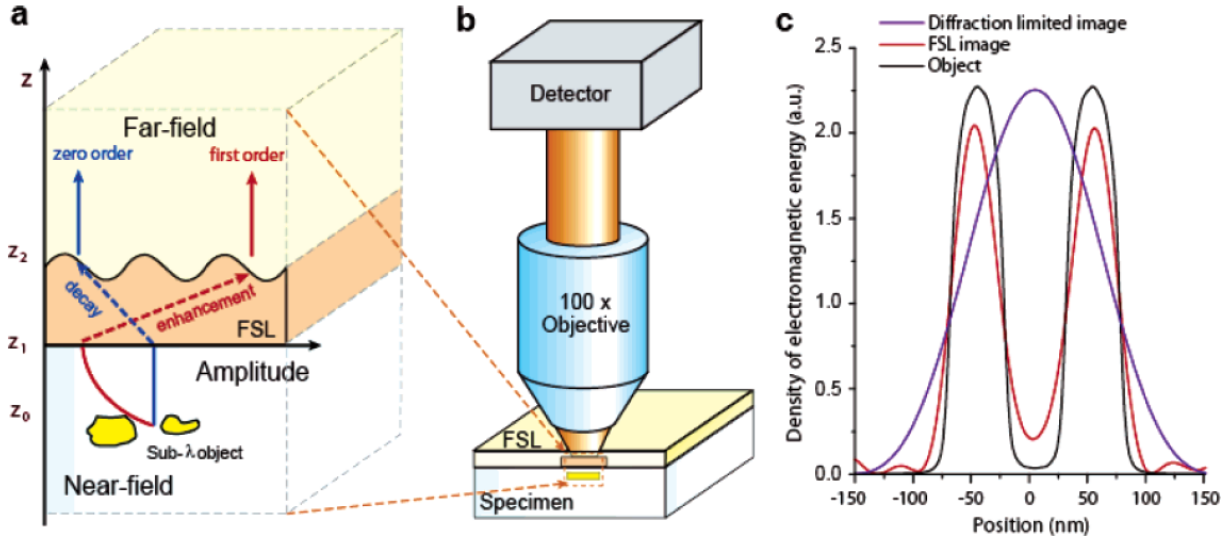


Figure 4. Schematic of the proposed far-field superlens design. (a) A corrugated silver film enhances the evanescent waves and converts them into propagating waves. (b) Illustration of the experimental setup. (c) Calculation comparing the object to the far-field image with and without a FSL. [9]

Plum et al [18] demonstrated a novel approach to achieving negative index, when they showed, that it can be found in materials with exceptionally strong optical activity. Their structure, which displays negative index due to 3D chirality, is a bilayered metamaterial based on pairs of mutually twisted planar metal patterns in parallel planes. The material shows negative electric and magnetic responses, as well as exceptionally strong optical activity and circular dichroism. Two separate resonances reaching negative index were found around 4.5 and 6GHz respectively.

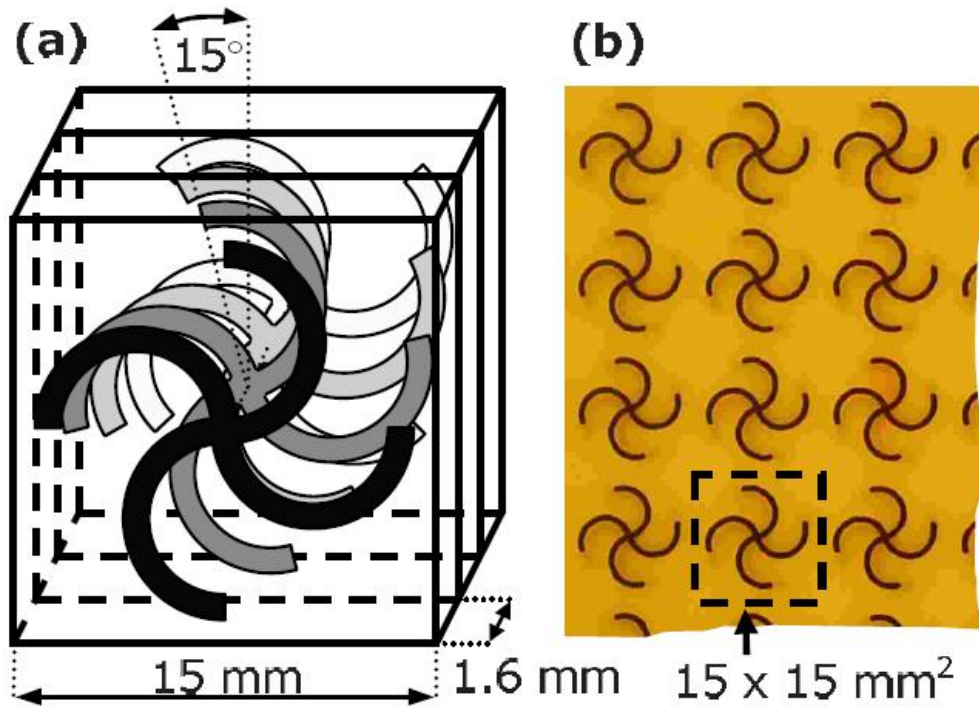


Figure 5. Illustration of the chiral metamaterial structure. (a) The material unit cell contains several layers of rosettes, with neighboring layers having a relative twist of 15° . (b) Photograph showing part of the metamaterials sheet. [18]

Generally the high losses associated with metallic components have been a key concern for metamaterials in general, and negative index materials in particular. A potential approach to solving this problem was demonstrated by Xiao et al [19], who showed that the loss could be compensated by incorporating a gain material into the structure. This was done by fabricating a multilayer fishnet structure consisting of alternating silver and alumina layers, then etching out the alumina, and replacing it with a polymer containing dye. The dye molecules can then be excited by an external source, and provide gain inside the negative index material itself, in order to offset losses. Experiments show that at wavelengths between 722 and 738 nm, corresponding to the emission peak of the dye, the sum of the light intensities in transmission and reflection actually exceed the intensity of the incident beam, while at the same time the material exhibits a negative refractive index.

Project goals and methods

The goal of this project was to investigate methods to improve superlensing in the ultraviolet range, and to achieve superlensing for visible light. In order to do this, we first set out to

fabricate a simple single layer silver lens, with an underlying chrome grating and a photoresist detection scheme, much like the previous work done by Fang et al [4]. Once this had been achieved, three different schemes for more advanced lenses were tested.

The first scheme uses a single silver lens, and a detection scheme consisting of nanoantennas and a scanning near-field optical microscope, see figure 6. The nanoantennas create high local field intensities at their resonance wavelength, and it is this resonance we attempted to image through the superlens, and then detect using the microscope.

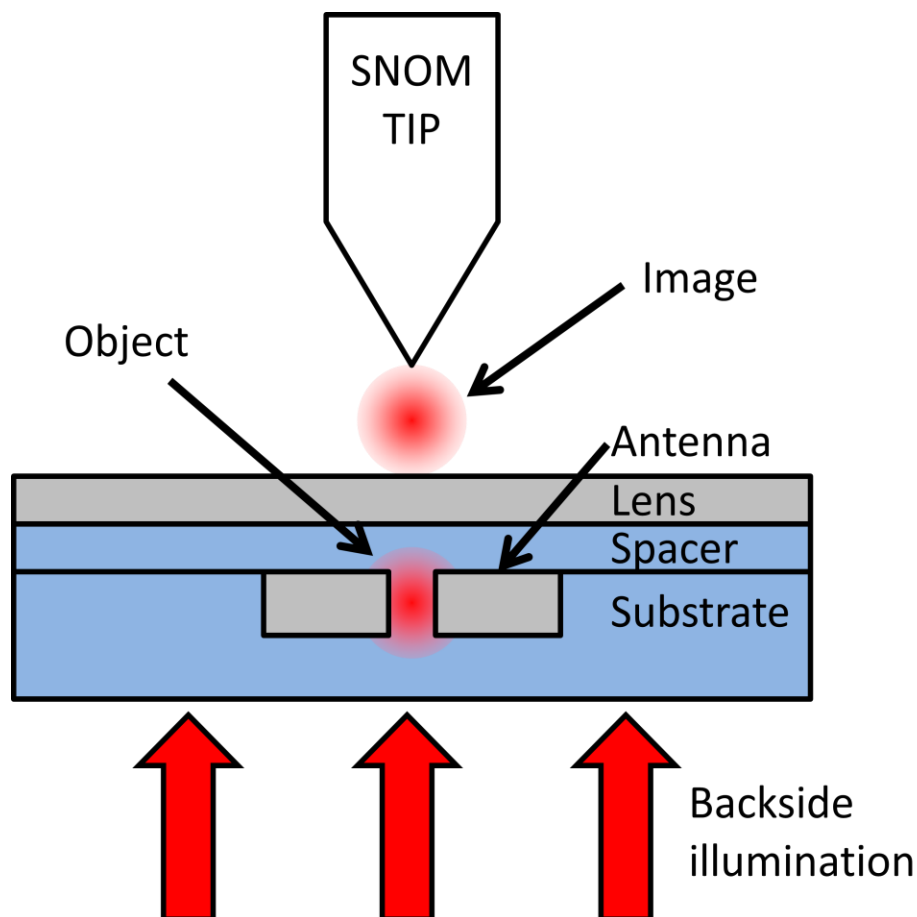


Figure 6. Illustration of the designed superlens structure. A pair of nanoantennas creates an optical hotspot when illuminated at the resonance wavelength, and this hotspot is imaged through the lens. A scanning near-field microscope is used to measure the intensity profile through the lens.

The inspiration for this work comes from an article by Liu et al [10], where they showed theoretically, that an optical hotspot can be translated through a superlens. The design was altered to change the operational wavelength from 1100nm to 633nm, which required

changing the lens composition, the spacer material, the substrate material and all the size parameters. Furthermore, the use of a scanning near-field optical microscope readout was added.

The second scheme uses metal-dielectric composites as the lens material. This composite material has a permittivity, which can be selective altered, thus opening up the possibility of creating a lens, that can be tuned to work at nearly any wavelength in the visible of near-infrared range [13]. A variety of metal-dielectric composites films were fabricated, and their optical properties were investigated by spectroscopic ellipsometry.

The third scheme replaces the conventional single silver layer with multiple thinner silver layers, which has been shown to theoretically improve the transfer function of the lens, and result in better imaging performance [20] [21]. Such multilayer lenses were fabricated from silver and silicon dioxide, and their performance was tested using a subwavelength chrome grating and a negative resist for detection.

Thesis outline

In addition to this introduction, the thesis will consist of six chambers:

Chapter 2 – Theory, sets out to provide the reader with a summary of all the background knowledge needed to understand the work presented here. This is not intended to be an in depth study of any particular subject, but rather a brief introduction to relevant theories and methods, as they relate to this project in particular. Topics include plasmonics, superlensing, micro fabrication and various characterization tools.

Chapter 3 - Ultraviolet superlens, explains the motivation for starting out with a simple silver slab superlens, and goes in depth with the fabrication methods developed here, since these will serve as a basis for the later chapters. Furthermore the quality and performance of the superlens is characterized.



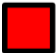








Chapter 4 – Near-field transfer of an optical hotspot, will describe the experiments on imaging a strong localized intensity through a superlens. The focus here is on how the test substrate was fabricated, and what the SNOM results show about the performance of such a structure.

Chapter 5 - Metal dielectric composites, is dedicated to the study of MDC films, with regards to their potential use as a tunable superlens. The work described here focuses on the composition and quality of the fabricated films, as well as their optical properties.

Chapter 6 - Multilayer superlens, will cover the attempts at improving superlens performance by using multiple thinner silver layers. This includes the fabrication methods used to create suitable test substrates, the deposition of a multilayer structure, AFM characterization of the lens, and characterization of the optical performance.

Chapter 7 - Conclusion and outlook, will summarize the results presented throughout the thesis, and discuss their importance within the field. Finally future prospects for this technology will be covered, as well as an outlook towards all the work yet to be done.

In the interest of clarity, a color scheme will be introduced here, which will be used throughout this thesis.

 Fused silica	 Aluminum
 Resist (Ebeam or UV)	 Chrome
 Exposed resist	 Silver
 Other polymer	 Germanium
 Zinc oxide	 Metal-dielectric composite
 Silicon	

Chapter 2 - Theory

The purpose of this chapter is to introduce the theoretical background for the thesis. As such the goal is to provide the reader with all necessary information, but not to study each topic in depth. The theory section will be divided into three sections, starting with photonics before moving on to fabrication and finally characterization.

In this section it is assumed, that the reader has a scientific background, so only aspects of particular importance to this project, will be covered.

Photonics

This section covers the photonics principles and structures used in the thesis.

Diffraction limit

All optical systems are fundamentally limited in the resolution, they can achieve by diffraction, often referred to as the diffraction limit [22]. This limit depends on the wavelength used, as well as the medium and the focusing angle.

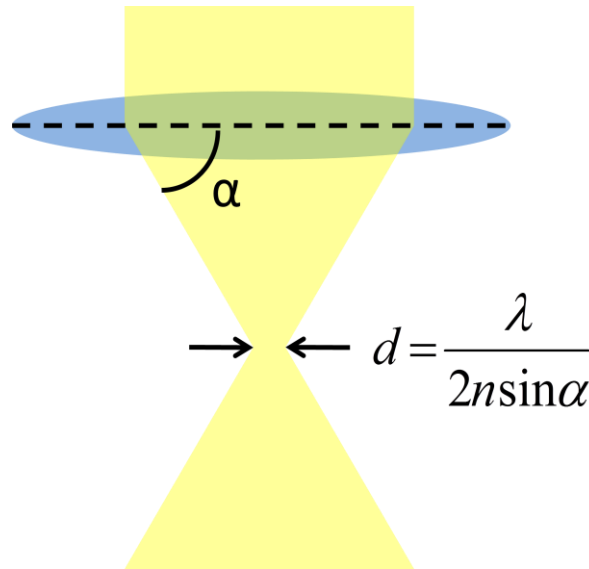


Figure 7. An Illustration of the diffraction limit. Even using an ideal lens, light cannot be focused below a certain size, which depends on the wavelength used as well as the refractive index and the focusing angle.

Usually measurements are done in air, so n equals 1, and the angle is large enough, that $\sin\alpha$ can be approximated as one, which leads to the common simplification that the diffraction limit is simply $\lambda/2$.

This fundamental limitation exists only in the far-field, and does not apply to near-field measurements, where the evanescent waves can carry subwavelength information. However, the evanescent waves decay exponentially away from the object, so the information is soon lost.

Plasmons

Plasmons are quasi-particles resulting from quantification of plasma oscillations, similar to photons in light waves, with most of their properties being derived directly from Maxwell's equations [23].

Plasmons play a major part in the optical properties of metals, by effecting the interaction with different wavelengths. Light below the plasma frequency is reflected, because the electrons in the metal screen the electric field of the light. Above the plasma frequency the electrons cannot react fast enough, and the light is transmitted. Since most metals have a plasma frequency in the ultraviolet, they have a blank shiny appearance (reflective). However, some metals have a plasma frequency in the visible range, thus altering their color, one such example being copper.

Surface plasmons are of particular interest in this project. These are plasmons that are confined to the surface and interact strongly with light. They occur at the interface between a material with a positive dielectric constant (or vacuum) and a material with a negative dielectric constant (typically the surface of a metal).

The interaction between the surface charge and an electromagnetic field has several consequences. One being that the momentum of the surface plasmon (SP) mode, k_{SP} , is greater than that of a photon in free space, k_o , with the same frequency. The frequency dependent SP

wave vector, k_{sp} , can be found by solving Maxwell's equation with the appropriate boundary conditions [23]:

$$k_{sp} = k_0 \sqrt{\frac{\epsilon_d \epsilon_m}{\epsilon_d + \epsilon_m}}$$

where the frequency dependent permittivity of the metal, ϵ_m , and the dielectric, ϵ_d , must have opposite signs for SPs to be possible at the interface. The resulting increase in momentum is associated with the binding of the SP to the surface.

Another consequence of the interaction is that unlike the propagation of the SP along the surface, the field perpendicular to the surface decays exponentially. Such a field is usually called evanescent or near-field in nature, and is a consequence of the bound nature of SPs, which prevents power from radiating away from the surface.

Since the momentum of a SP is greater than that of a photon in free space, it is necessary to bridge that gap, if a SP is to be created. This can be done in one of several ways, including coupling through a prism, scattering from a surface topological defect, or a periodic corrugation in the metal. The reverse is also possible, that is the coupling of a bound SP mode to light, which is critical in developing SP based devices.

Once light has been converted into a bound SP mode, it will propagate along the surface, but diminish slowly due to ohmic losses in the metal, with a speed determined by the dielectric function of the metal at the oscillation frequency of the SP. The propagation length can be found by looking at the imaginary part, k''_{sp} , of the complex SP wave vector [24].

$$\delta_{sp} = \frac{1}{2k''_{sp}} = \frac{c}{\omega} \left(\frac{\epsilon'_m + \epsilon_d}{\epsilon'_m \epsilon_d} \right)^{\frac{3}{2}} \frac{(\epsilon'_m)^2}{\epsilon''_m}$$

where, ϵ'_m , and, ϵ''_m , are the real and imaginary parts of the metal dielectric function.

Propagation length depends greatly on the specific metal and light wavelength. Silver has the lowest losses in the visible spectrum with a propagation distance in the 10-100 μ m range,

increasing to upwards of 1mm as the wavelength moves to the 1.5 μm near infrared telecom band.

In addition to the absorption loss in metals, there is another key source of loss: The unwanted coupling of propagating SPs to freely propagating light, which can occur in surface defects.

Near-field superlensing

By looking at Snell's law [25]:

$$n_1 \sin \theta_1 = n_2 \sin \theta_2$$

it can be seen, that materials with a negative refractive index will refract light at a negative angle compared to the surface normal. For a parallel slab of negative index material, this means that convergent light will be focused [3], an illustration of which can be seen in figure 8.

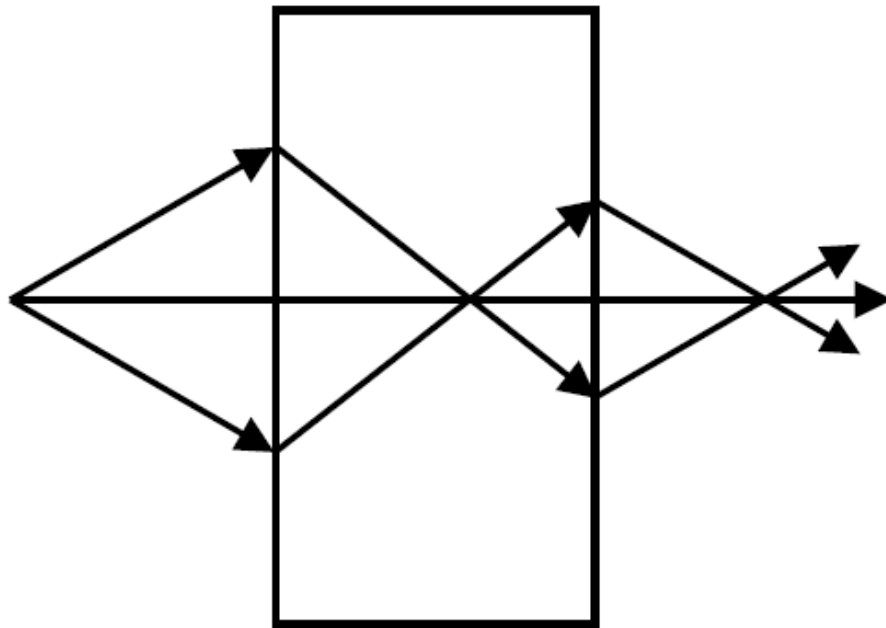


Figure 8. Light incident on a slab of negative refractive index material will be refractive at a negative angle compared to the surface normal, which has the effect of focusing divergent light from a nearby source. [3]

The use of such a material as a lens was first proposed by Veselago [2], and later studied by Pendry [3], who showed, that subwavelength resolution could be achieved, and dubbed it a

“superlens”. In his design the requirement is not just that $n = -1$ as Veselago specified, but that $\varepsilon = \mu = -1$.

The reason such a lens can achieve subwavelength resolution, is that the evanescent wave amplitude actually increases inside the lens, which helps to restore the information, that would otherwise be lost, and allows the lens to reproduce the image including all the spatial frequencies, even those for which the spatial frequency is larger than k_0 (evanescent waves) [26].

While theoretically interesting, such lenses are difficult to realize in practice, and they have an inherent drawback, since the best possible resolution is given by the periodicity of the metamaterials structure [27], which at present is tens of nanometers. However, when considering a system in the electrostatic limit, with all dimensions smaller than the wavelength, the electrostatic and magnetostatic fields can be decoupled, and the requirements for the lens are eased. For p-polarized light the dependence on permeability disappears, and only the permittivity needs to be negative [3]. As a result many metals now meet the requirements, and silver in particular is promising.

The enhancement of evanescent waves in slab with negative permittivity is caused by coupled surface plasmons at the two interfaces of the lens.

In order to achieve impedance matching between the lens and its surroundings, and thus avoid reflection at the interface, a simple requirement must be met [4]:

$$\varepsilon_{lens} = -\varepsilon_{host}$$

which is commonly referred to as the superlens matching condition. For dispersive materials this condition is only met at one particular wavelength, which is referred to as the superlens operation wavelength.

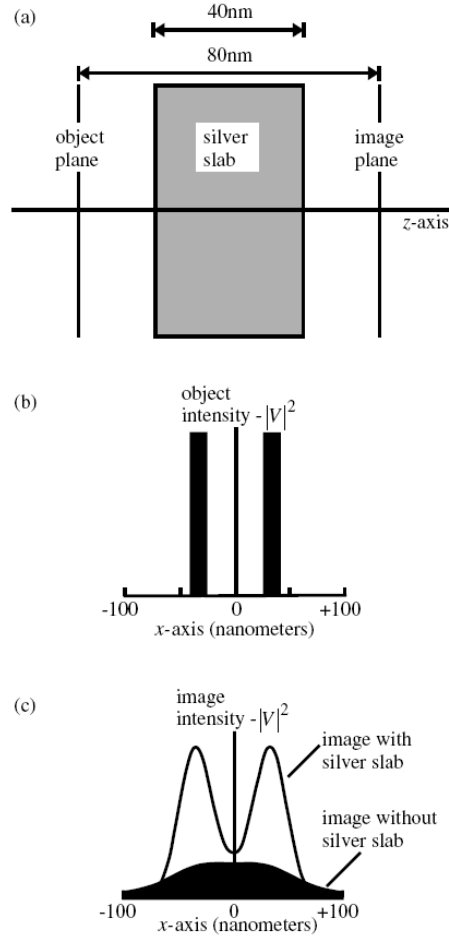


Figure 9. Illustration showing the design of a silver slab superlens (a), the object intensity profile (b), and the image with and without the lens (c). With the lens it is possible to resolve the two closely spaced intensity peaks, while they blur into one without the lens. [3]

The inherent loss in real materials has the effect of introducing a cutoff frequency, above which the various spatial components die out before reaching the image place, thus resulting in a loss of image quality. This cutoff frequency can be estimated as [26]:

$$k_x^{cutoff} \approx \frac{1}{d} \ln \frac{2}{e''}$$

where d is the thickness of the lens, and e'' is the imaginary part of the permittivity. Thus as one might expect, thinner lenses with lower loss more faithfully reproduce the image. However, in addition to the cutoff frequency, losses also have the effect of dampening the surface plasmon resonance, which can otherwise distort the image [26].

Ideally superlens designs use a perfectly flat surface, but such geometry cannot be realized in practice. As a result, a key limiting factor in the resolution of a real superlens is the surface roughness, which has a linear relationship with the image line edge roughness, and starts to cause serious distortion at values above 0.8nm root-mean-square (RMS) [28].

Multilayer superlenses

The excitation of coupled surface plasmons at both interfaces is a necessary condition for near-field superlensing, but such coupling only takes places, if the interfaces are sufficiently close. This has the effect of limiting the possible thickness of a single layer superlens, and thus the distance over which a subwavelength image can be resolved. A solution to this problem can be found by using multiple thinner lens layers, which are separated by layers with positive permittivity [26].

An additional advantage of using multiple thinner layers as oppose to a single thicker one, is that the cutoff frequency can be increased substantially, as shown in figure 10.

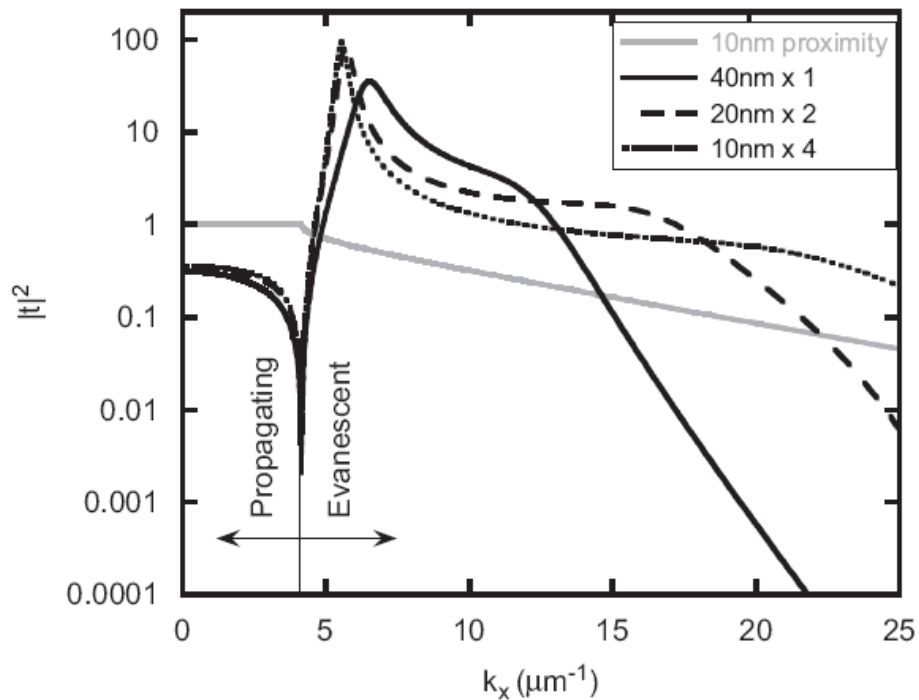


Figure 10. Graph showing the transfer function for 3 different lens configurations with a total silver thickness of 40nm. [21]

However, increasing the number of layers is not without drawbacks, since the transfer only improves for a certain range of frequencies, meaning no single lens design will provide the best solution for all objects.

An alternative multilayer superlens design was proposed by Belov [14], who proposed the use of a multilayer metal-dielectric lens operating in the canalization regime, and works by transmitting the image, rather than using negative refraction and amplification of the evanescent waves to restore the image. His design allows for a much thicker lens, but places very strict requirements on the thickness, which has to be an integer number of half wavelengths.

The superlens matching condition for multilayer lenses differs from that of a single layer lens, and several different matching conditions have been proposed depending on the specific lens geometry [8] [14] [15].

Nanoantennas

Metal nanoparticles, gold and silver in particular, interact strongly with visible light due to resonant excitation of surface plasmons. As a result the incident light is scattered very strongly, and local electromagnetic fields can reach intensities several orders of magnitude higher than the incident field. The resonance frequency of such an excitation is dependent on the size, shape, material and surrounding medium. The resonance frequency undergoes a red shift as the size of the individual particles increase, which, for particles larger than 10nm, can be attributed to phase retardation [29].

If two metal particles are sufficiently close, they can form a coupled oscillation, which can be described as a dipole-dipole interaction. Such pairs are usually referred to as nanoantennas.

The resonance wavelength of a pair of nanoantennas will be shifted compared to that of the individual particles, with the shift increasing exponentially as the distance between them decreases [29]. The direction of the shift depends entirely on the polarization of the incident light. If the light is polarized parallel to the long axis of the particle pair, the resonance will be strongly red shifted, while an orthogonal polarization results in a slight blue shift [30].

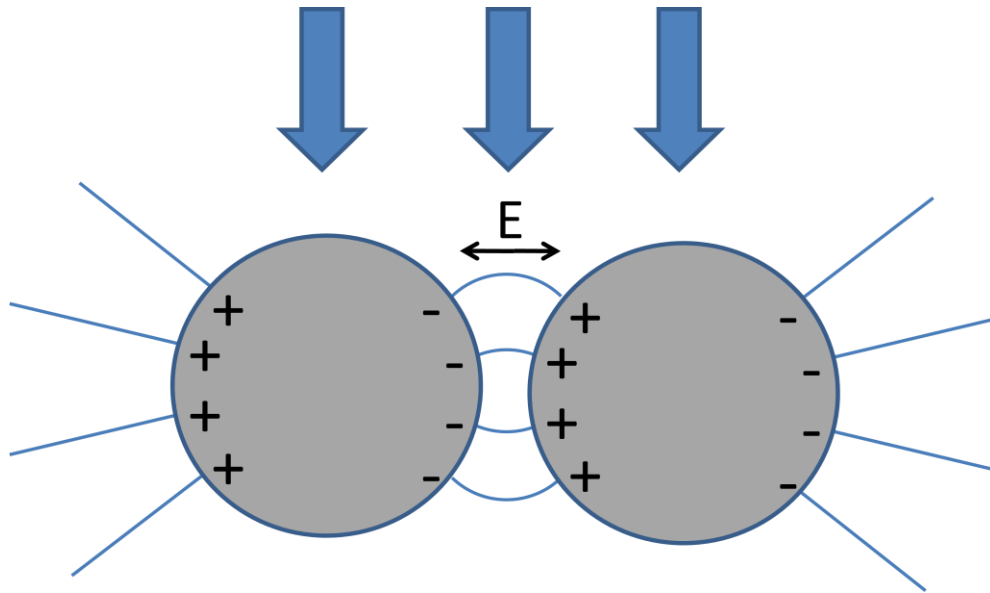


Figure 11. Illustration showing a pair of circular metal nanoantennas. When illuminated at the right wavelength and polarization, a resonant dipolar interaction can be excited. This resonance results in high local field intensities, particularly across the gap.

By altering the shape of the individual antennas, it is possible to change the localized field distribution around the antennas. Sharp corners or points increase the local intensity in that area, but decrease the spatial extent of the resonance, while wide or rounded shapes have the opposite effect.

Metal-Dielectric Composites

Metal-dielectric composites (MDCs) are random mixtures of metallic and dielectric particles [31]. The individual particles are still pure, containing either metal or dielectric, but the overall mixture takes on properties somewhere in between those of its constituent parts.

In order to describe this class of materials, a number of effective medium theories (EMTs) have been developed. Inherent in these theories is the requirement, that the individual particles are large enough to be described by macroscopic properties like permittivity, yet small enough to avoid behaving like a pattern of individual particles. A requirement that results in slightly

different sizes depending on the specific material, but is generally in the range of several nanometers to a few tens of nanometers [32].

The two most commonly used EMTs are known as Maxwell-Garnett [33] and Bruggeman [34], named after the people, who first developed them. Both theories are based around the notion, that an effective medium can be described, with properties that depend on those of the individual constituents as well as the mixture ratio. The requirement for such an effective medium is, that an individual particle surrounded by it would have no forward scattering, and thus blend perfectly with its surroundings. If this requirement is met, the medium will appear homogeneous to optical fields.

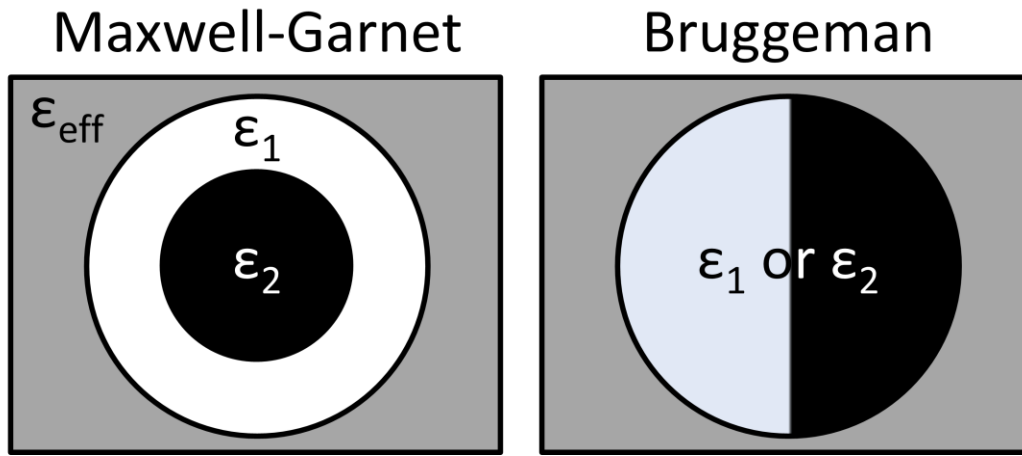


Figure 12. Illustration of the models used in Maxwell-Garnett and Bruggeman EMT theories, both of which involve a spherical particle surrounded by an effective medium.

In Maxwell-Garnett's theory the particle has a metallic core with a dielectric coating, and the dimensions are determined by the filling factor [32]:

$$p = \left(\frac{r_2}{r_1}\right)^3$$

In Bruggeman's theory the particle is either metallic or dielectric, with a probability given by the filling factor [32]:

$$p = P(\epsilon_2)$$

The main difference between the two, is that Maxwell-Garnett is inherently limited to describing only mixtures below the percolation threshold for the metallic components, since it is based on a spherical metal particle with a dielectric coating. For this reason it is best suited to describe a situational, where individual metal particles are suspended in a dielectric matrix, and thus not suited to describe the mostly metallic composites needed for superlensing purposes. For this reason Bruggeman's theory was chosen, which predicts the following relationship between the individual permittivities and the effective permittivity [32]:

$$p \frac{\epsilon_m - \epsilon_{eff}}{\epsilon_m + (d-1)\epsilon_e} + (1-p) \frac{\epsilon_d - \epsilon_{eff}}{\epsilon_d + (d-1)\epsilon_e} = 0$$

where the subscript m refers to the metal, d is the dielectric, and e is the effective medium, while the letter d stands for the dimensionality. As seen the theory predicts a very simple relationship, where no material properties other than the permittivity are considered.

The predicted optical properties for MDCs will be covered in greater detail in chapter 5.

Fabrication

This section will focus on the various fabrication methods used, and cover their operating principle as well as key advantages and disadvantages.

Ultraviolet Lithography

Ultraviolet lithography (UVL) is a commonly used fabrication method, which serves to transfer designed patterns onto a surface. It works principally by illuminating selected areas of a photosensitive material (usually called a photoresist) through a mask consisting of a patterned metal film on glass.

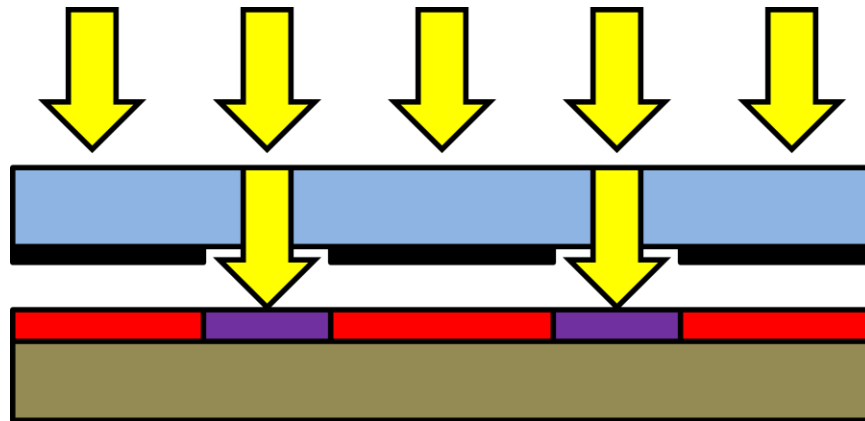


Figure 13. Illustration of photolithography. A photo sensitive material (red) is exposed to ultraviolet light through openings in a chrome film (black) on a glass plate (blue). Exposed areas (purple) are altered chemically.

Photoresists are typically polymers dissolved in an organic solvent, though some solvent free liquid pre-polymers also exist. Chemical amplification is often used to increase sensitivity to UV exposure. This is done by adding a photoactive acid compound that degrades photoresist, making it easily soluble in a developer such as NaOH.

A typical photo lithography process consists of a number of steps:

- **Surface preparation:** Typically either dehydration bake or deposition of an adhesion promoter such as Hexamethyldisiloxane (HMDS).
- **Photoresist deposition:** This is done by pouring the photoresist onto a spinning wafer at low speed to create a uniform layer, then increasing to a higher speed to achieve the desired thickness of the photoresist layer.
- **Pre-exposure bake:** Used to remove solvent and promote adhesion to the surface.
- **Alignment:** Using a mechanical stage and microscope the mask is correctly placed over the substrate. If multiple layers are used, they can be accurately aligned by using dedicated surface markings consisting of interlaced geometric shapes.
- **Exposure:** The photoresist is exposed to UV light for a specified period of time.
- **Post-exposure bake:** Used to complete dissolution of exposed areas.
- **Photoresist develop:** The exposed photoresist is removed in a wet process, typically using NaOH.

In addition to positive photoresist as described so far, negative resists are also commonly used. These resists have the opposite behavior, meaning polymers in areas exposed to light are crosslinked to become insoluble, and thus remain after the developing step, while unexposed resist is easily removed.

Once the photoresist layer has been patterned with the desired design, it can be used either as a mask for a subsequent process, or as a part of the final device itself.

Due to the wave nature of light, exposure profiles are not as ideal as designed, which has the effect of degrading of the pattern fidelity due to diffraction effects. This becomes increasingly problematic as dimensions shrink, and patterns are more closely spaced.

One consequence of this is seen, when considering the resolution of a particular system, which can be estimated with the following equation [35]:

$$R = k \sqrt{\lambda \left(s + \frac{z}{2} \right)}$$

where k is a set-up specific parameter, λ is the light wavelength used, s is the distance between mask and photoresist, and z is the photoresist thickness.

Thus resolution decreases with spacing between mask and surface, which is why these are often brought into hard contact. However, for some substrates it may be necessary to use a proximity exposure instead, to prevent mask contamination and sticking.

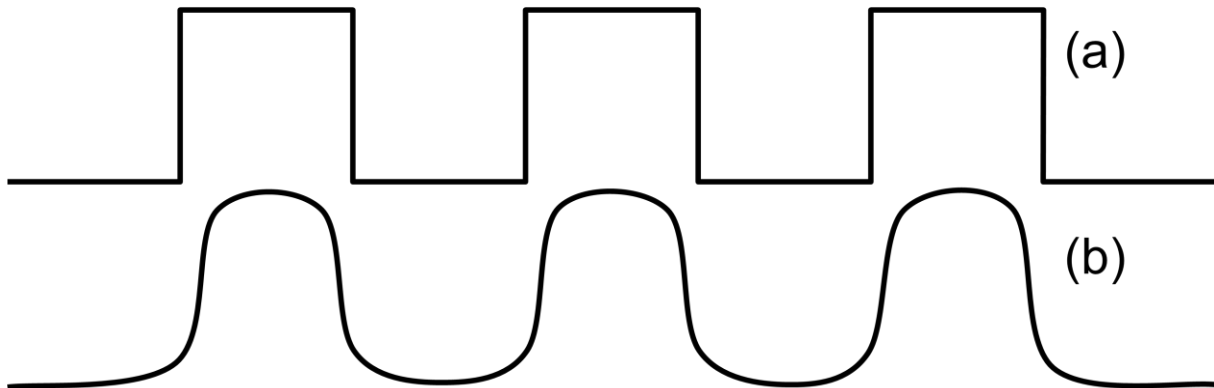


Figure 14. Illustration of an ideal exposure profile (a) versus that of a real system (b).

Additionally photoresist behavior is also non-ideal, meaning there is no sharp transition from unexposed to exposed resist. Instead the amount of resist remaining after the developing step changes gradually with dose.

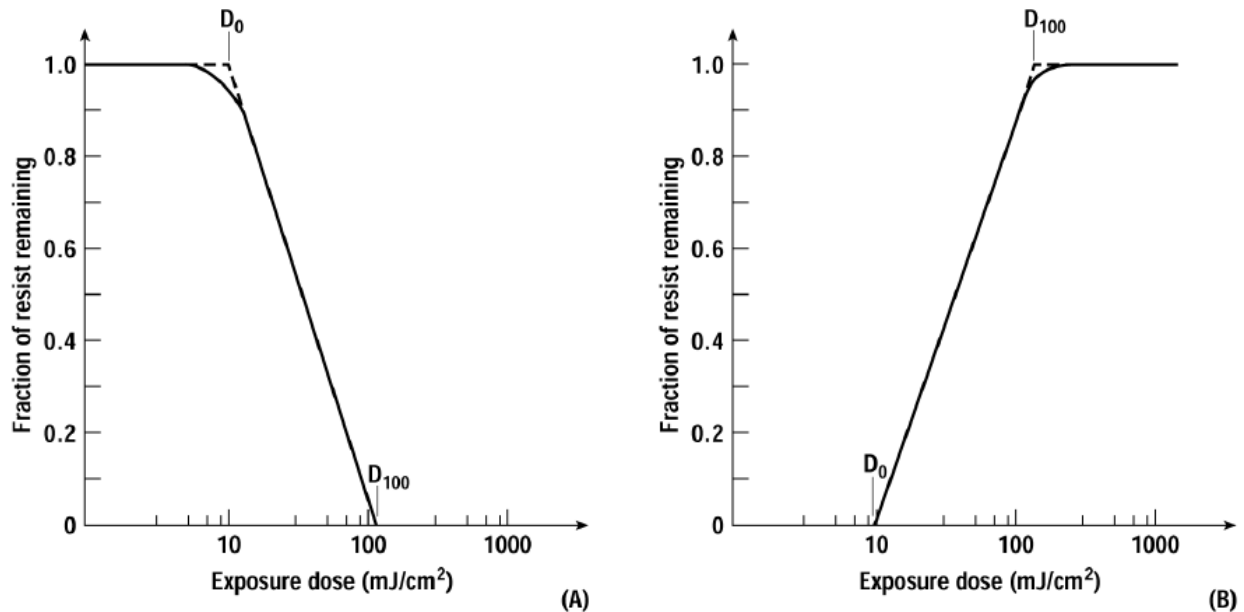


Figure 15. Contrast curves for typical positive (a) and negative (b) resists, values shown are arbitrary [35]

Typical resolution for photo lithography is around a micron, though higher precision systems, using deep or extreme ultraviolet light, can achieve a resolution up to 2 orders of magnitude lower.

After use a photoresist mask can be removed either with a powerful solvent like acetone, often using ultrasonic sound to help with agitation and speed up the process, or in an O_2 plasma (see Reactive Ion Etching).

Electron-beam lithography

Electron-beam lithography (EBL) [36] is a fabrication method, which works by using a focused beam of electrons to chemically alter a polymer film. It is a higher resolution alternative to UVL, but is less commonly used because of the drastically lower throughput. The key difference between the two is that while UVL exposes everything at once through a physical mask, EBL

targets only a single point at a time, and moves the beam by using computer controlled magnetic fields. As a result it is unfeasible to write pattern covering an entire wafer, since doing so would take months or even years.

The electron-beam can only be moved over a short distance using the magnetic deflectors, typically a few hundred microns, which means it is necessary to divide the pattern into so-called write fields, and moving the sample physically before writing each new field. This has to be done with extreme accuracy, since the pattern would otherwise become misaligned at the boundaries of these fields. As a result the whole chamber has to be isolated from all vibrations, and kept at a very exact constant temperature.

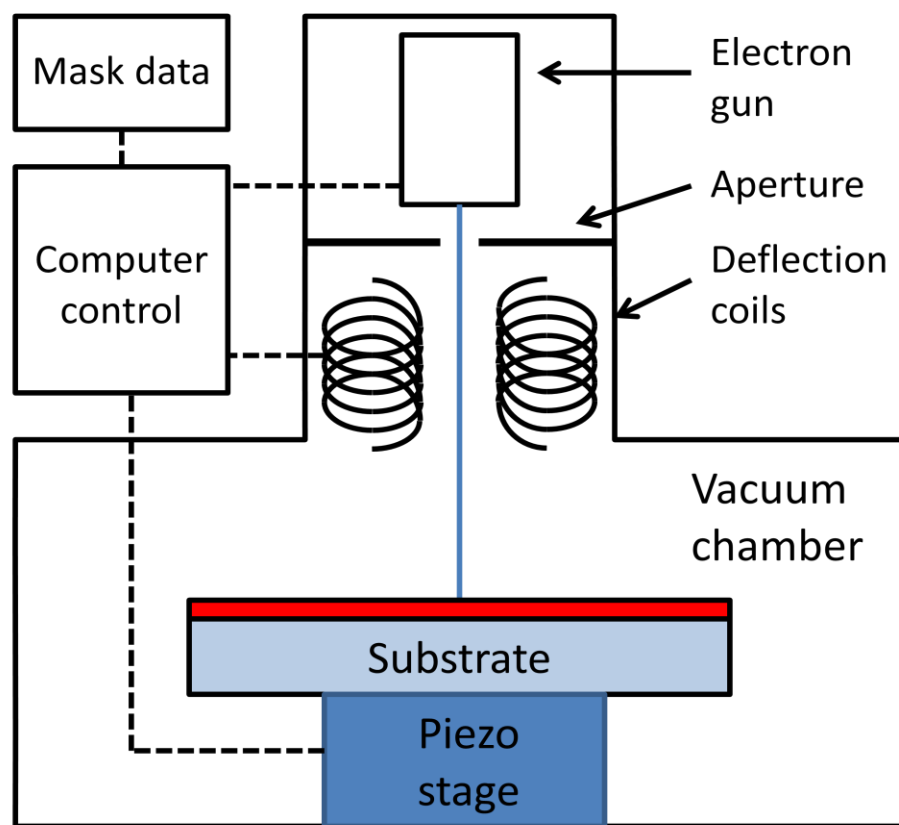


Figure 16. Schematic design for an electron-beam writer.

When the electrons hit the polymer film, they cause what is known as chain scission, which is the breaking of a molecular bond, effectively splitting the long carbon chains in two pieces. The

shorter fragments can be dissolved in an organic solvent, while the longer chains in unexposed areas remain unaffected. These collisions cause the electrons to lose some of their energy, as well as change their direction of travel. As a result two key processes occur, which ultimately determine the resolution of the EBL:

- **Forward scattering** – Due to collisions the electron-beam widens as it penetrates the film. This causes the initial Gaussian shape of the beam to be distorted, and worsens with penetration depth, which leads to the need for very thin polymer films, typically around 100 nm. The forward scattering width is called α , and depends on the acceleration voltage.
- **Back scattering** – Some of the electrons are turned around by their collisions inside the substrate, and end up being re-emitted through the polymer film. As a result of the many collisions, the electrons will not be re-emitted at the same point they entered, but rather in a wide Gaussian distribution around the point. The backscattering distance is called β , while the relative amount of electrons that are re-emitted is called η . These parameters depend on the acceleration voltage as well as the substrate material.

Both forward and backward scattering are undesirable, since they distort the pattern. In order to minimize this effect very high electron energies can be used, up to around 100keV. Higher energy electrons are less affected by each collision, thus reducing forward scattering.

Furthermore they penetrate deeper into the substrate, which lowers the amount of backscattered electrons, and widens the area they re-emit from, thus resulting in a lowered back scattered dose. Using a higher energy does however have a drawback, since it also increases the dosage required, and thus lengthens the write time.

The amount of backscattering is also affected by the substrate material, since large nuclei have a larger scattering radius, which lowers the penetration depth.

The combination of forward and backwards scattering is usually referred to as proximity effects, and can significantly change the pattern created. Because of this models are used to take these

effects into account, and calculate what the dose distribution should look like, in order to achieve a desired pattern. This is called proximity correction software, and is mainly used for very dense patterns, or patterns with a large size distribution.

In addition to accelerating voltage, the key parameters for EBL are the beam current and the distance between individual points, called the grid size. These are somewhat interconnected, since the current determines the width of the Gaussian beam, and thus how far apart the individual points can be, while still overlapping to create a continuous exposure area.

Furthermore, there is an inherent tradeoff between the increased accuracy that can be achieved with smaller current and grid, and the increased throughput that can be achieved with larger values. The current is normally on the order of 0.1-10 nA, and the grid size is between 4 and 10 nm.

Resist for EBL has a non ideal contrast much like that for UVL, and several different types are available, including some negative resists. The main differences between resists are their resolution, how large a dose is required per unit area, and which processes they are compatible with.

The resolution of EBL is typically down to a few tens of nanometers, though demonstrations of sub-10nm resolution have been made.

Since EBL works by bombarding the substrate with electrons, it is vital that the substrate is conductive, otherwise charge will build up and interfere with the electron-beam. This is not an issue for silicon, which is conductive enough, but for silica substrates it becomes a problem. A solution can be found by coating the substrate with a conductive film.

Reactive Ion Etching

Reactive Ion Etching (RIE) [37] is a fabrication method, which uses chemically reactive plasma to selectively remove material. Gas enters through a small inlet at the top of the etching chamber, at a constant flow rate, and exits through a vacuum pump below the wafer, which help maintain a constant low pressure. The plasma is generated in a strong radiofrequency (RF) electromagnetic field, typically operating at 13.56 MHz, which ionizes the gas. Ions are then

accelerated in an electric field, and striking the surface with a lot of energy. This results in either knocking off material (sputtering), or reacting chemically with the surface.

Typical gases used include O_2 , SF_6 , CF_4 etc, depending on the material to be etched.

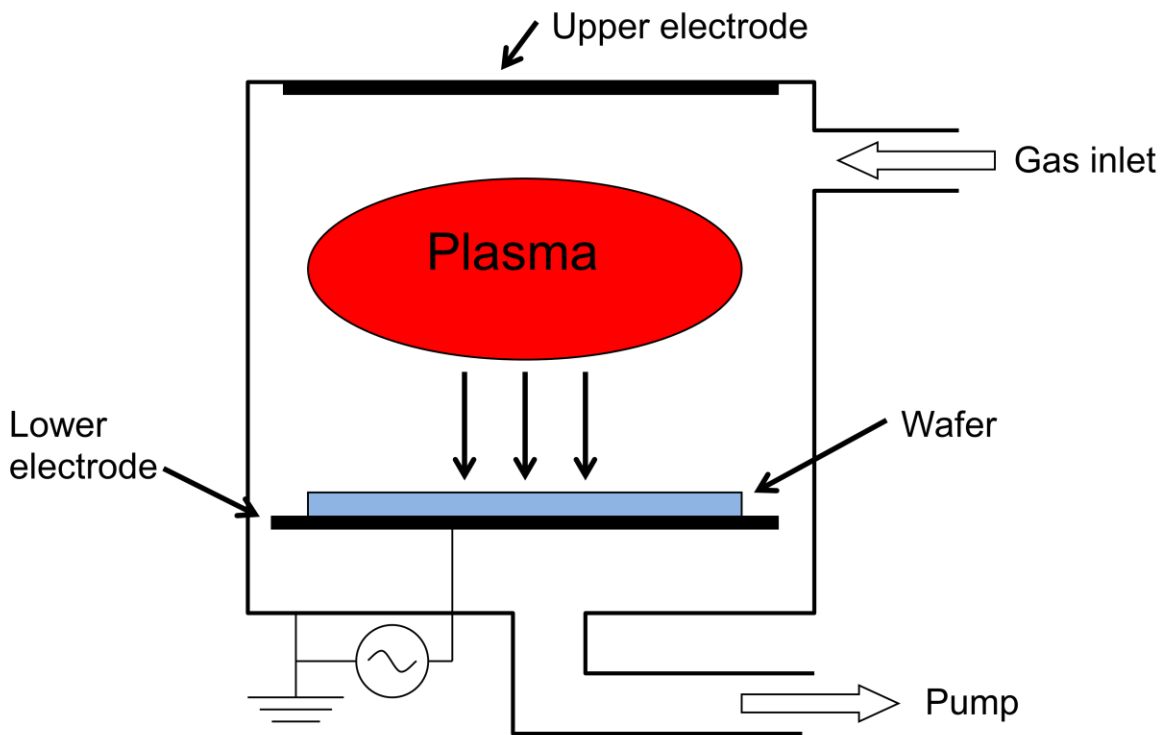


Figure 17. Schematic of a typical RIE chamber. Reactive gas is ionized by the application of an RF field, and accelerated towards the surface, where it will etch away material.

Depending on the specifics of the process used, RIE can be either anisotropic or isotropic in nature, often a combination of the two. Etches that are physical (sputtering) in nature tend to be highly anisotropic, as the yield depends greatly on impact angle, while more chemical etches are isotropic.

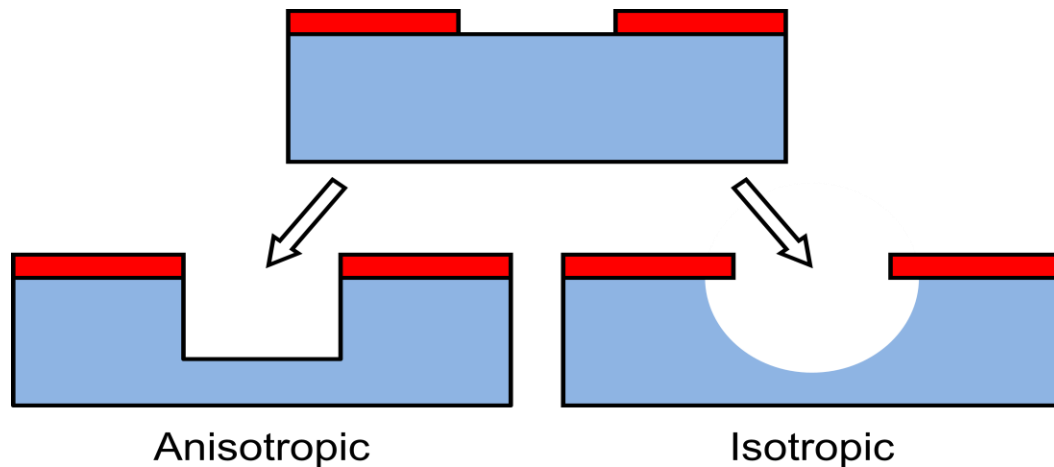


Figure 18. Illustration of an anisotropic etch versus an isotropic etch. Only material in areas unprotected by a mask layer will be removed.

Key process parameters are:

- **Power:** Higher power typically increases anisotropy.
- **Gases used:** Determines the specific etch chemistry, for example SF_6 is typically used for silicon, and O_2 for polymers.
- **Gas flow rate/Chamber pressure:** Determines the amount of reactants available, and affects uniformity across the wafer. Typically measured in standard cubic centimeters per minute (sccm)

So-called loading effects are often observed in RIE, which is a variation in etch rate across the wafer. Due to the finite amount of reactants present, concentration in some areas may be higher than others, which can be a problem in deep structures or masks with a variation in coverage across the wafer. Large amounts of material exposed to the etch, also known as high wafer load, reduces the amount of reactants available, thus altering the etch profile.

Photoresist is commonly used as a RIE mask, though it offers relatively poor selectivity. For cases where a higher etch selectivity is needed, metals or SiO_2/SiN can be used.

Plasma Ashing

Plasma ashers [37] can be thought of as simplified RIE chambers. They use RF to generate a plasma like RIEs, but no bias voltage is applied, so the etch is purely isotropic. Furthermore they typically operate at lower vacuums.

Because no bias is present, there is no risk of sputtering during an etch, and thus very limited risk of cross contamination, which often leads to less strict rules concerning the materials allowed in the chamber.

Physical Vapor Deposition

Physical vapor deposition (PVD) [38] is a group of techniques used to deposit thin films, all of which share some key aspects. Deposition takes place in a vacuum chamber, it is achieved by condensation of vapor on a surface, and it is surface independent. As such it is fundamentally different from competing chemical vapor deposition (CVD) techniques, which rely on surface specific chemical reactions to form thin films.

PVD is most commonly used to create thin metallic coatings, though it can also be used for some dielectrics and semiconductors. Material suitability for PVD is mainly limited by the need for the material to exist in vapor form, which excludes complex molecules like polymers. Typical deposition thicknesses for PVD range from a few monolayers up to several microns

PVD is done in vacuum, typically on the order of 10^{-6} mbar, for several reasons. One reason is to avoid contamination of the deposited films, since many of the materials deposited react with atmospheric air. Another reason is to allow the particles to travel as freely as possible, with as few collisions as possible, which is desirable, because it makes the deposition directional rather than conformal. When combined with the fact that the distance between source and substrate is much larger than the source, the result is that deposition only occurs in the vertical direction. The reason this is important will be discussed later in the lift-off section.

When using PVD it is usually desirable to monitor the exact rate of deposition, as well as the total thickness. This is done by placing a sensor in close proximity to the substrate. This sensor contains an oscillating quartz crystal monitor (QCM), which vibrates at a mass dependent

resonance frequency, thus allowing it to accurately sense how much material is deposited into its surface.

Certain types of metal, like gold or silver, have a relatively poor adhesion to many materials, including Si and SiO₂, meaning an intermediate layer is often needed to promote adhesion. The materials most commonly used for this purpose are Titanium and Chromium.

The main variation between PVD methods is the way in which material is evaporated, which has a large impact on film quality and material availability. In this section only three of the many available PVD methods will be covered, since these are the methods relevant for this thesis.

Electron-beam evaporation

In electron-beam evaporation [39] a target anode is bombarded with an electron-beam extracted from a charged filament. The electron-beam creates intense localized heating, which causes material on the target to evaporate. Due to the intense heating it is necessary to continuously cool the target material. This is achieved by placing the material in a water cooled copper crucible.

The crucible is usually designed with multiple pockets for different materials, and rotated in between depositions to access the material needed.

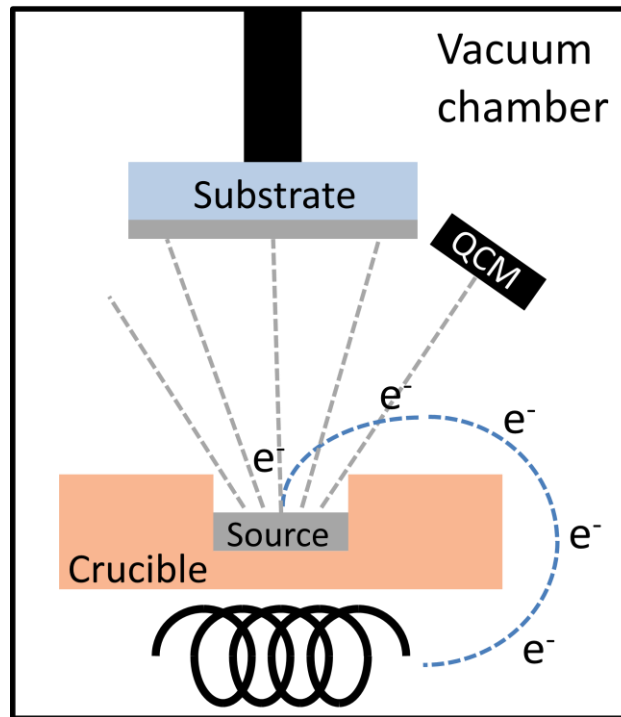


Figure 19. Schematic design for a typical electron-beam evaporator.

In order to avoid material buildup on the filament, it is placed out of line of sight from the source, and strong magnetic fields are used to bend the electron-beam towards the source.

The key deposition parameters for electron-beam evaporation are extraction voltage and beam current, with typical values of 5-10 kV and 50-500 mA. The voltage is generally kept constant for a particular chamber, while the current varies depending on the material to be deposited, and the desired deposition rate.

Some oxides like zinc oxide or titanium dioxide are not suitable for e-beam evaporation, since they dissociate when heated, which creates a difference in stoichiometry between the target and the deposited thin film. This problem can be alleviated to some degree by using an oxygen flow during deposition, but such methods can lead to other problems, particularly if other materials that might react with oxygen are present in the chamber.

Thermal evaporation

Thermal evaporation [39] works by placing the source material in a crucible, which is suspended between two electrodes, and then passing a current through it to achieve ohmic heating.

Inherent in this heating method is the fact that the crucible will reach the same temperature as the source material, which limits compatible materials to those with a melting point far below that of the crucible. Furthermore the high temperature and intimate contact between source and crucible can result in the formation of various alloys, which can be destructive to the crucible structure, or cause contamination of the deposited material. Thus in addition to the thermal considerations, it is necessary to consider chemical compatibility between the source material and crucible material, leading to the use of various different crucible materials depending on the source material used.

The limitations on material choice, as well as the fact that thermal evaporations usually requires both source material and crucible to be replaced after every evaporation, limits the uses for thermal evaporation. However, it does have one key advantage when compared with electron-beam evaporation, which is the reason, it is used in this project. This advantage is that no free electrons are present in the deposition chamber, thus allowing it to be used for depositing metal onto electron-beam resist without exposing the resist.

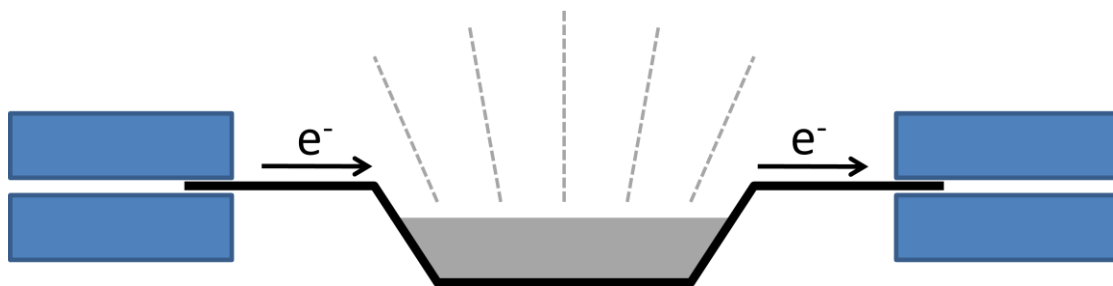


Figure 20. Illustration of the operating principle for thermal deposition. A crucible filled with metal is clamped at either end by electrodes. The metal is melted by passing a current through the crucible, which heats up the crucible, and starts the evaporation process.

Sputtering

Sputtering deposition [40] differs fundamentally from electron-beam and thermal evaporation by not using heat to extract atoms from the source. Instead an inert gas, typically argon, is introduced to the deposition chamber, where it is ionized, and accelerated in a strong electric field. The charged argon ions then collide with the source, where they knock loose some

material, and transfer some of their kinetic energy to these free atoms. The sputtered atoms are not charged, which allows them to escape the electric field and reach the substrate.

By using this non-thermal deposition method, sputtering can be used for materials with any melting point. Furthermore sputtered films generally have a composition very close to that of the source, even for oxides or other materials than can be difficult to deposit by alternative methods.

One of the limitations of sputtering is that the chamber pressure is much higher than other methods, due to the Argon flow needed for plasma formation. As a result the chances of collisions occurring are far higher, thus making the deposition less directional.

When sputtering non-conductive materials, charge buildup can occur on the surface of the source. In order to avoid this, it is necessary to use a sputtering method where the anode-cathode bias is switched at a high frequency, which is referred to as RF sputtering. Another class of materials that can be problematic to deposit are those with strong ferromagnetism, since their innate magnetic field can disturb that of the sputter gun, thus requiring specialized guns with a stronger than normal magnetic field.

This need for multiple types of material specific sputter guns usually leads to the design of deposition systems with several independent guns. As a side effect this allows the simultaneous deposition of multiple materials onto the same target.

Lift-off

If a particular pattern of metal is required, rather than simply a uniform coverage, this can be achieved by depositing metal onto a patterned photoresist surface. Once the metal has been deposited, the resist is removed with an organic solvent, leaving behind metal only in the areas where no resist was present, thus reversing the pattern. This is known as a lift-off process [41].

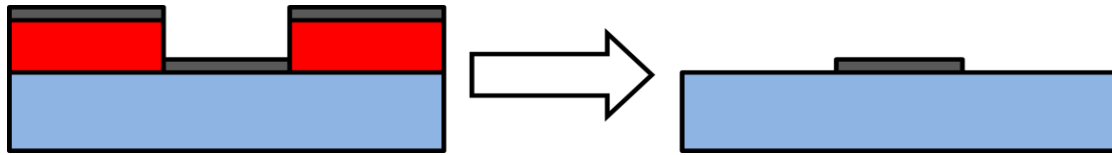


Figure 21. Illustration of a simple lift-off process. Metal (grey) is deposited onto a patterned photoresist surface (red). Once the resist is removed, metal remains in areas where no photoresist was present.

In order for a lift-off to work as intended, all metal deposited on areas without resist should remain, while all metal deposited on areas with resist should be removed. This however is not trivial to achieve. If enough metal is present on the resist sidewalls, it will connect the two areas, and prevent a successful lift-off. To avoid this, it is necessary for the deposition to be highly directional.

Depositing metal causes heating of the substrate surface, especially when depositing on materials with poor thermal conductivity such as photo resist. The heating is the result not only of vapor condensing on the surface, but also of radiated heat from the source. As such it is necessary to take into account thermal limitations when doing lift-off, especially for large metal thicknesses. Most PVD chambers have no active substrate cooling, so passive means like placing the substrate on a large heat sink are needed. Alternatively it may prove necessary to do the deposition in small steps, with time in between for the substrate to cool down.

If overheating of the resist does occur, it can cause several problems. For mild cases the resist will simply become harder to dissolve, thus requiring additional time in the organic solvent, or the use of ultrasound to provide agitation. In more severe cases the resist will heat to the point where it becomes liquid or chemically unstable, which has the effect of severely distorting, or in some cases entirely destroying, the pattern.

Characterization

This section will focus on the characterization tools used, and cover their operating principle as well as key advantages and disadvantages.

Atomic Force Microscopy

Atomic force microscopy (AFM) [42] is a very high resolution surface measurement technique, capable of creating a quasi-3D surface map with sub-nanometer resolution. It works by

scanning a cantilever with a very fine tip across the surface in a raster pattern, while measuring tip deflection with a laser setup.

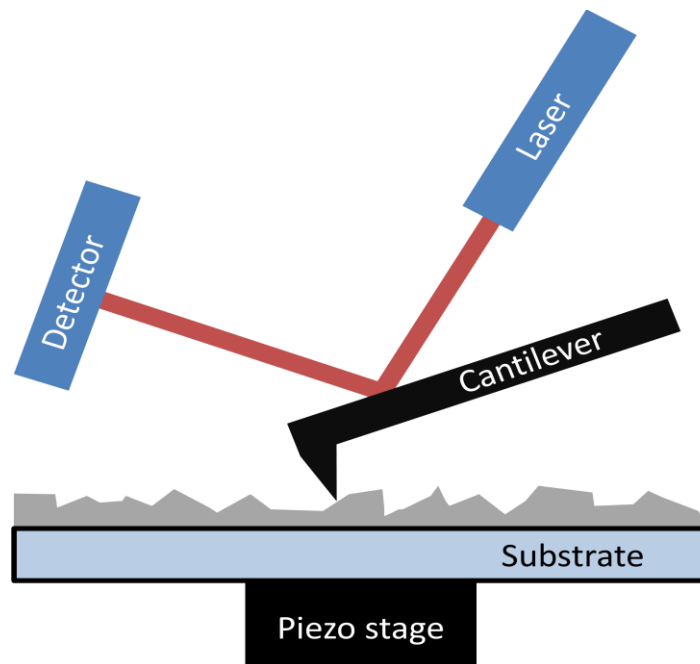


Figure 22. Schematic of a typical Atomic force microscope. Topological information about the sample is captured by using a laser setup to measure the deflection of a scanning cantilever.

The image created contains a single z value for every point in the (x,y) -plane, which can be claimed as 3D, but only contains information about the surface.

The tip is of crucial importance for AFM, since the depiction you get, is directly limited by the probe you use to obtain it. It is possible to image individual atoms, but doing so requires a tip with a single atom at the end, and such tips are both expensive and prone to wear. For most purposes less ideal tips are used, with a radius of curvature around 10nm for the tip, thus limiting x - y resolution to this same value, since the tip will not be able to fit inside smaller details. Furthermore the tip has a triangular shape, which will be replicated in the image data. So even if the surface contains vertical walls, they will still appear to have the same slope as the tip.

The resolution in the z-direction is not affected by tip size, and will retain sub-nanometer precision.

AFMs can be operated either in contact or non-contact mode. In contact mode the tip is dragged across the surface, and the topography is obtained directly from tip deflection. However, such measurements are prone to noise, and they can be problematic, since the cantilever tends to stick to the surface due to inter-atomic forces. Alternatively AFMs can be operated in non-contact mode, where the cantilever oscillates near the surface, at a frequency close to its resonance frequency. In this mode short range interactions with the surface can be monitored, by looking at changes in the amplitude, phase and frequency of the oscillation. Using non-contact mode reduces the wear to both the tip and the substrate.

The need to physically scan over the sample limits the possible imaging area for AFM, with the maximum being around 50x50µm. Due to this limitation, it is necessary to have an optical microscope included in the AFM setup, which is used to find the area of interest.

Scanning Electron Microscopy

Scanning electron microscopy (SEM) [43] is a common type of electron microscopy, which works by scanning a high energy beam of electrons across the sample in a raster pattern, and capturing an image by measuring the resulting emissions. SEM images have the advantage of being able to achieve a resolution on the order of a few nanometers, while at the same time offering a very large range of magnifications, all the way from 10x to 500000x (equipment dependent).

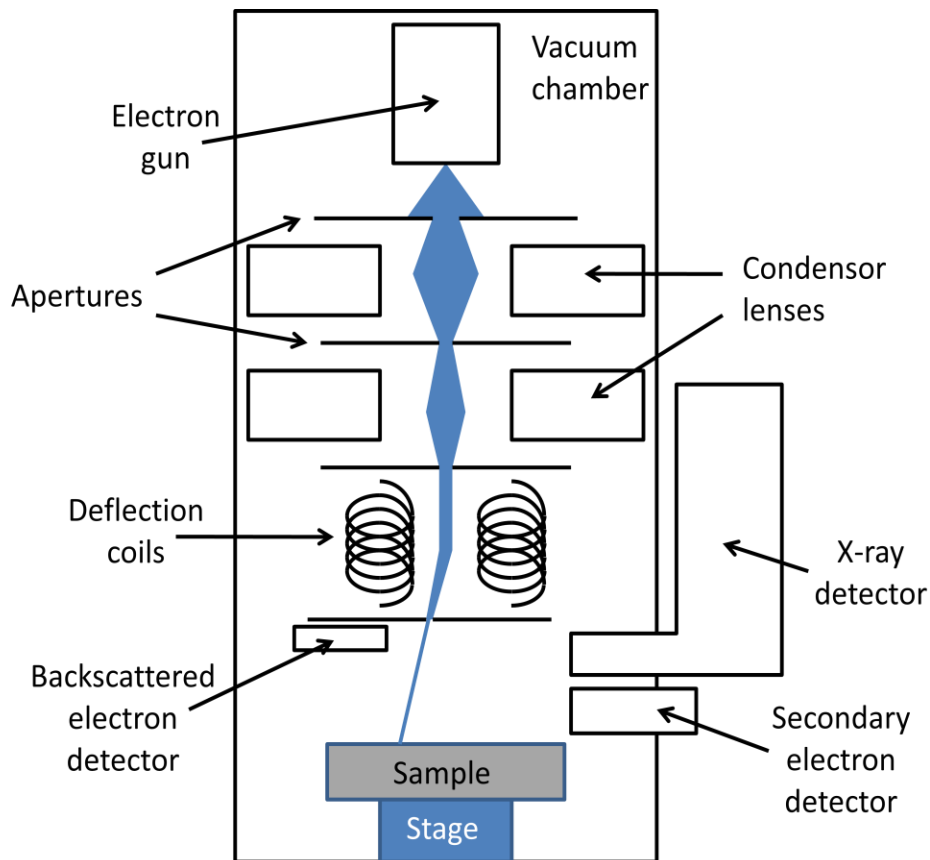


Figure 23. Schematic of a typical SEM. The electron-beam is focused by magnetic lenses before being scanned over the sample surface. The resulting emission is captured by a variety of detectors.

Conventional SEMs use hot tungsten filaments to thermionically emit electrons, while more modern SEMs have replaced the tungsten filament with a field emission source. Field emission sources offer the advantage of more coherent and concentrated beams, as well as being lower maintenance, since they forego the frequent need to replace the filament.

Three main detection methods are used, capturing secondary electrons, backscattered electrons and x-ray emissions respectively, each of which requires its own dedicated sensor. Secondary electrons are the result of inelastic scattering, while backscattered electrons are the result of elastic scattering, and x-rays are produced by electron excitation.

Capturing quality images on non-conductive substrates can be difficult due to charge buildup on the surface. This can be alleviated somewhat by using lower vacuum conditions and detectors designed for the purpose.

Energy Dispersive X-ray spectroscopy

Energy dispersive x-ray spectroscopy (EDX) [43] is an analytical technique used to identify the elements present on a sample. It works by analyzing the x-rays emitted, when atoms in the sample are hit by a beam of high energy free electrons. Since this method requires a beam source, it is commonly found as an add-on in SEMs.

At rest, atoms in the sample contain ground state electrons bound in various energy levels around the nucleus. When hit by high energy free electrons, some of these bound electrons are excited to higher energy levels, which leaves behind a hole in the level, they previously occupied. An electron from a higher energy level will then move in to fill up the hole left behind, and in doing so it will emit X-ray radiation, with energy equal to the difference between the two levels. These energy levels are unique to each element, thus by measuring the x-ray radiation with an energy dispersive spectrometer, it is possible to identify the atomic element it came from. Atoms have multiple energy levels, which results in more than one specific radiation energy for each element.

The accuracy of an EDX spectrum has some limitations, the first of which is, that low energy radiation is absorbed before reaching the detector, which prevents the detection of elements with an atomic number below 4 (H, He and Li). Furthermore the acceleration voltage used for the electron-beam has an effect on measurements, since the measurable spectrum only extends up to this energy (in eV), and raising the voltage will cause decreased sensitivity at lower energies. Finally, energy levels from different elements may have an overlap, which can make them difficult to distinguish between.

The nature of the samples used also has some influence on the measured spectra, since the chance of emitted radiation reaching the detector, is dependent on the amount and density of material it has to pass through, so the sensitivity declines with penetration depth. This means it will be difficult to accurately measure, if the sample composition changes with depth.

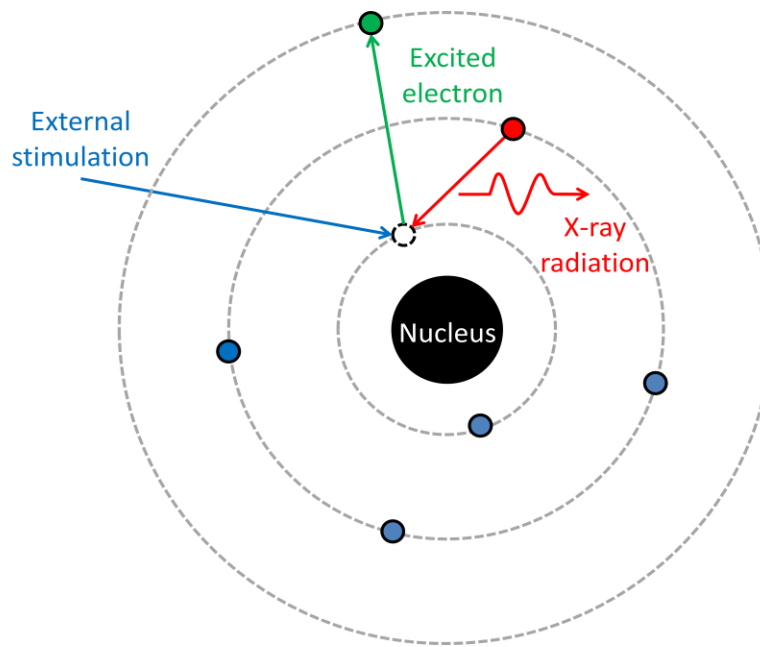


Figure 24. Schematic of the working principle behind EDX. External stimulation causes the excitation of an electron from one of the lower energy levels, thus leaving behind a hole in the level where the electron was. An electron from a higher energy level can then fill this whole, which results in the emission of X-ray radiation with energy equal to the difference between the two levels.

When performing an EDX measurement, the beam scans over a specified area, and data is collected on the amount of atoms of each element present in this area. Since the EDX is integrated into a SEM, the imaging capability can be used to find specific areas or structures of interest. Thus it is possible not only to determine, which elements are present on the sample, but also how it varies across the sample.

Spectroscopic Ellipsometry

Ellipsometry [44] is an optical characterization method used to investigate the dielectric properties of thin films. By looking at the reflected light from a sample, ellipsometry can yield information of layers much thinner than the wavelength used, in some cases even reaching atomic resolution. This is done by looking not only at the amplitude of the reflected light, but also the polarization and phase, and can be extended to include multiple angles of measurement and wavelengths, thus yielding further information about the sample.

For ellipsometry to be valid the sample generally has to be homogeneous and isotropic, otherwise the standard assumptions used to model the behavior will not be valid. Samples with

multiple layers can be analyzed, as long as the number of layers is relatively small, and the light penetrates deep enough to access all interfaces. In addition to yielding information about the dielectric properties of each layer, it is also possible to determine their thicknesses using ellipsometry.

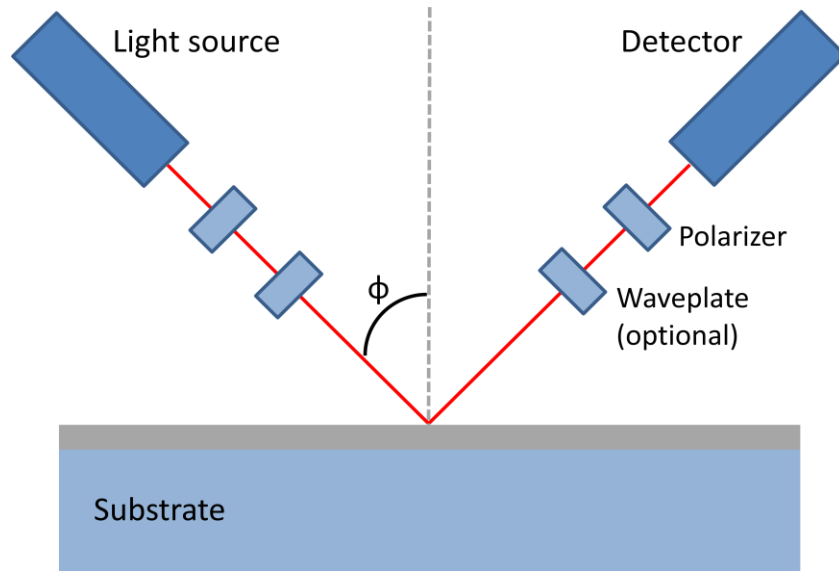


Figure 25. Schematic of a typical ellipsometer.

Ellipsometry measures the complex reflectance ratio, ρ , which is given by [44]:

$$\rho = \frac{r_p}{r_s} = \tan(\Psi)e^{i\Delta}$$

where the polarization of the incident light has been decomposed into an s (perpendicular to the plane of incidence) and a p (parallel to the plane of incidence) component. The normalized amplitude of the reflected light is denoted by r , and the complex ratio between r_s and r_p is parameterized by Ψ and Δ .

In order to convert the measured Ψ and Δ values into the desired permittivity of the substrate layers, it is necessary to fit the data to a model. This method is indirect, and exactly only in cases of isotropic, homogenous and infinitely thick films.

Scanning Near-field optical microscopy

Scanning near-field optical microscopy (SNOM or NSOM) [45] is a microscope technique used for nanostructures, which is capable of breaking the diffraction limit by using the information found in evanescent waves. This is done by placing the detector at a distance of less than one wavelength from the object, which enables the capture of information that might otherwise be lost, since the evanescent field decays exponentially away from the surface. The resolution that can be achieved using this method, is limited not by the wavelength, but rather by the size of the detection aperture.

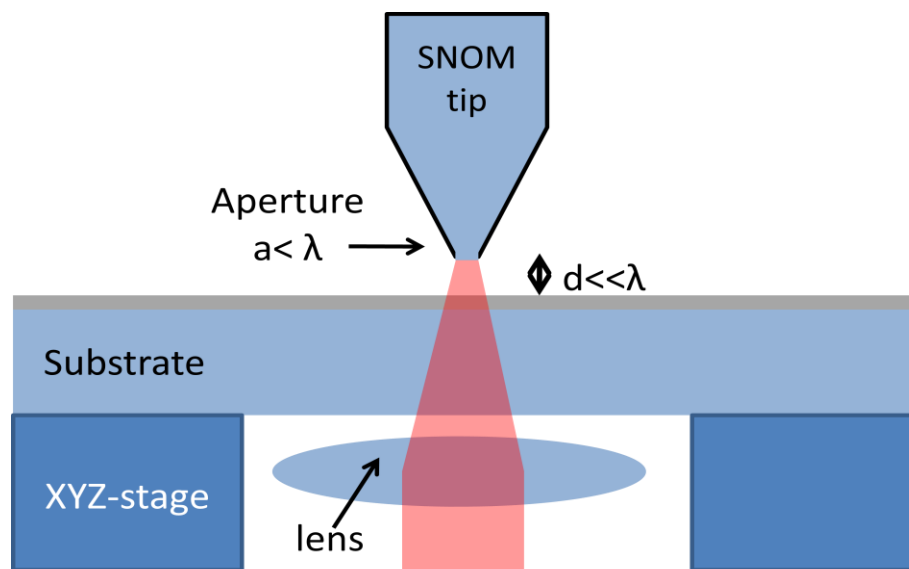


Figure 26. Illustration of a SNOM operating in collection mode, where light is transmitted through the substrate, and collected by the tip.

In addition to the optical information, SNOMs can generate topographical or force data from the surface, in the same manner as the atomic force microscope. After a scan, the two separate data sets (optical and topographical) can be compared to determine the correlation between the physical structures and field distribution.

Chapter 3 – Ultraviolet superlens

This chapter will deal with the experiments performed in an effort to establish and verify a fabrication scheme for ultraviolet superlensing using a simple silver slab. This particular approach uses photoresist to create a physical image of the field intensity, and was inspired by the studies of Fang et al. [4]. The main purpose of this work was to develop the necessary experience and expertise for further superlensing studies. Additionally, our investigation was targeted towards eventual integration in lab-on-a-chip systems [46], which affects the choice of materials.

The work included in this section was performed in collaboration with Claus Jeppesen from DTU Nanotech.

Key changes

While the work described in this section was inspired by previous studies, there are some key differences which will be explained here.

#1. Changing the lithographic method

The lithographic method used to define the grating pattern was changed from focused ion beam milling (FIB) to EBL. This was done in part because no FIB was available in the cleanroom, and while one was available nearby, the resolution was not satisfactory. Additionally the use of EBL is advantageous from a planarization standpoint.

#2. Embedding the metal grating

Using EBL rather than FIB to write the pattern allows us to embed the metallic lines in the substrate, rather than simply placing them on top. This is done by use an RIE step after EBL but prior to metal deposition, in which holes are etched with a depth matching that of the intended metal height.

A key advantage of embedding the structure by using our fabrication method is, that the initial height variation is much lower, which means the thickness of the polymer planarizing layer can be reduced. The result is that the object is closer to the lens, which will drastically increase the transmissivity of evanescent waves [47]. Our testing shows, that the polymer thickness can be reduced to below 40 nm without compromising the surface roughness, with 30 nm being a possibility. Below that, however, the planarizing effect starts to be lost.

#3. Adding an aluminum surrounding layer

Since the lift-off process used when using EBL to define the grating is negative, only areas which were exposed, will be covered in metal. This being the case, the area around the grating structure will not have any metal coverage, as exposing it would require too long a write time. Therefore, during the UV exposure light can pass through the substrate, until it reaches the photoresist layer, at which point it will expose the resist. Ideally this would not be a problem, as it would only occur outside the area of interest. However, initial experiments showed, that the photoresist layer itself can act as a waveguide and re-direct light into the grating area, where it will greatly distort the observed pattern.

In order to avoid this problem, a non-transparent aluminum surrounding layer was added, through the use of a secondary lift-off step, with the pattern being defined through UV lithography.

#4. Changing the polymer used for planarization

The polymer planarization layer was changed from PMMA to mr-I T85 (otherwise known as Topas or cyclo-olefin copolymer). This change proved necessary because PMMA is very easily soluble, and will dissolve when it comes into contact with the organic solvent used in the final photoresist layer, and when it is submerged during the final development step. As a result the structure will completely degrade, and no useful measurements can be made. How this problem was avoided previously remains unknown, though we attempted to contact the authors for clarification.

Using Topas solves the issue, since this particular polymer is nearly insoluble, and can be submerged in most organic solvents without any problems.

The choice of Topas ($\epsilon=2.415$) has an additional advantage, since it a closer match for minus the permittivity of silver ($\epsilon = -2.401$) at 365 nm, than PMMA is ($\epsilon=2.301$).

Compared to PMMA, Topas is highly chemically resistant, more heat resistant, and has lower water absorption [48]. Furthermore, it has been shown that Topas has very low losses in the ultraviolet range [49]. The combination of these properties makes Topas more suitable for lab-on-a-chip applications than PMMA.

#5. Using multiple etch steps

Rather than etching the Topas down to 40 nm in a single RIE step, we opted to use multiple shorter etch steps, as well as brief plasma ashes to reduce surface roughness. This was done in order to improve the accuracy, with which a 40-nm layer can be achieved, since both the etch rates and initial polymer thickness varies from time to time, by a few percent, and measuring the thickness several times along the way, helps to ensure that the correct thickness is reached.

Modeling

In order to investigate the properties of our grating structure and superlens design, we performed full-wave simulations of the transmitted field. This was done using a commercially available finite-element method (Comsol Multiphysics). The program solves the wave equation:

$$\nabla \times \nabla \times \mathbf{E} = \frac{\omega^2}{c^2} \epsilon \mathbf{E}$$

with an incident electric field E_0 polarized perpendicular to the grating lines. In the model perfectly-matched layers were used for the horizontal domain boundaries, while periodic boundary conditions were used for the vertical domain boundaries.

An illustration of the modeled system can be seen in figure 27. The figure combines a schematic of the geometric design, with an intensity distribution for 365 nm light normally incident on the grating with a half pitch of 80 nm. The intensity distribution shows six clear maxima, each of

which is associated with an opening in the chrome mask, thus demonstrating the superlensing principle. For dosages above the threshold value, this should create a periodic pattern in exposed photoresist, which can be used to experimentally validate the properties of the lens.

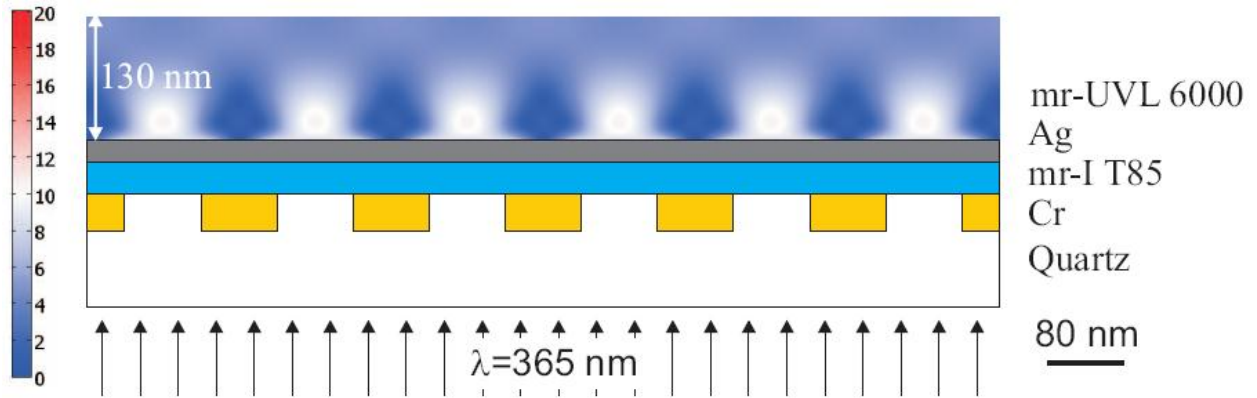


Figure 27. Comsol finite-element simulation of the normalized intensity distribution through a superlens for six grating periods illuminated at 365 nm. The grating has a half pitch of 80 nm.

The material properties used were $n=1.475$ for quartz, $n=1.4+i3.25$ for Cr, $n=1.554$ for Topas ($\epsilon=2.415$), $\epsilon=-2.401+i0.2488$ for silver and $n=1.649$ for mr-UVL6000. While Al is present on the sample, it was not included in the model, since it is only found in areas outside the modeled area.

The geometry of the design corresponds to those of the final fabricated structures, as discussed later on in the fabrication section.

Further modeling was performed on gratings with periods of 60-80 nm in order to study the size dependency. A summary of the results can be seen in figure 28.

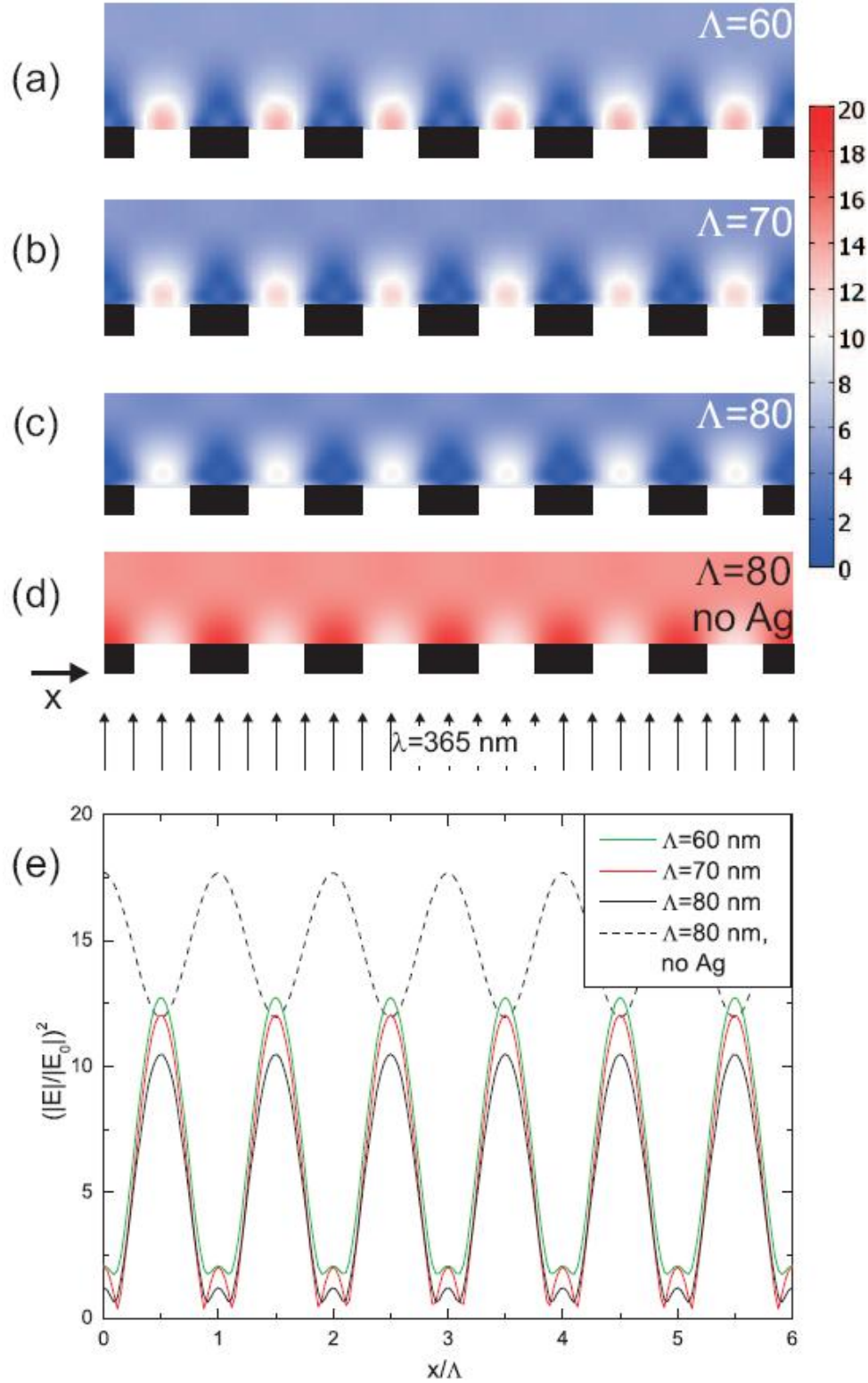


Figure 28. Comsol finite element simulation of the normalized intensity distribution for various gratings. For simplicity the planarizing layer and silver superlens are not shown, and the x-axis is varied so each plot shows six periods. Panels (a)-(c) show simulations with a superlens layer and gratings with a periodicity of 60, 70 and 80 nm, respectively. Panel (d) shows a

reference sample with a periodicity of 80 nm and no superlens layer. Finally panel (e) shows a comparison of intensity profiles 15 nm into the photoresist film.

As seen in Figure 28, an increase in the grating period results in a lowering of the peak intensity. For periods larger than 80 nm half pitch this makes it hard to identify the individual peaks.

For comparative purposes a control structure was also modeled, in which the 35 nm silver superlens layer had been replaced with an equivalent thickness of Topas. The results show, that the six peaks are still visible, with an intensity that is higher overall due to the decreased loss, but the contrast is much lower, and due to diffraction the highest intensity is now found in areas directly behind the chrome mask.

Pattern design

In order to create and test the grating patterns described, we developed a matching set of UV and electron-beam lithography masks. These masks contain three main components: A test pattern for electron-beam dosage and proximity correction, a pair of alignment marks to ensure correct overlay, and a number of grating patterns with varying periodicity.

The test patterns are necessary in order to ensure optimal pattern fidelity for the electron-beam exposures, which can be difficult to achieve, since the grating design is high density, and has an extent smaller than the backscattering distance. Because of this, the backscattering dose will be significant and very non-uniform across the pattern, which means that proximity correction must be performed. This was done using Beamer software designed for the JEOL tool we used. The parameters used for proximity correction were $\alpha=50\text{nm}$, $\beta=35\mu\text{m}$ and $\eta=0.6$, which seemed to work well with the fused silica substrate.

The grating itself is not a good test structure for the exposure, since the lines are spaced too closely for an AFM tip, thus making it difficult to properly characterize the exposure prior to lift-off. Instead a dedicated test pattern was used, which can be seen in figure 29.



Figure 29. Schematic of the dose test pattern used, blue areas are exposed while white areas are not. The pattern contains 10 lines of ascending widths spaced 1 μm apart, with line widths ranging from 30 nm to 250 nm. The widely spaced single lines allow full AFM characterization, and the high area coverage requires very accurate proximity correction for the smallest lines to show up.

Using this pattern, a successful exposure could be easily verified simply by observing ten full height lines in an AFM scan, while a less successful exposure would result in some lines having reduced height or being absent.

In order to correctly align the UV and electron-beam patterns, alignment marks consisting of a set of crosses were used, as seen in figure 30.

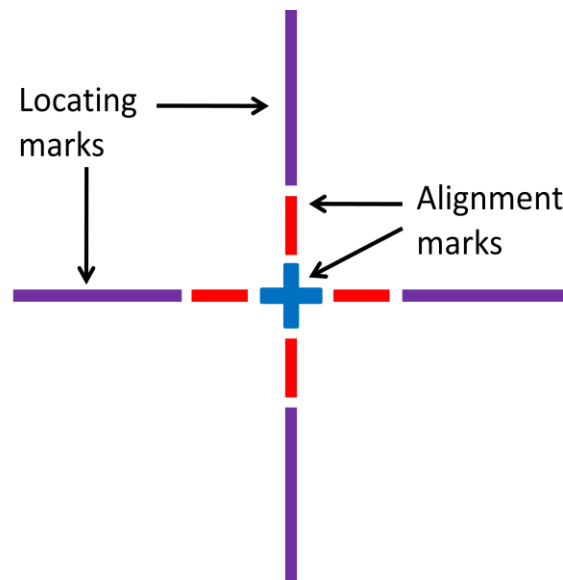


Figure 30. Schematic of the alignment marks used to ensure proper placement of the UV patterns relative to the electron-beam patterns. Blue marks are present on the UV mask, red marks are present on the electron-beam pattern, and purple

marks are present on both. The cross pattern used allows for very exact alignment, both in xy-directions and in rotation. The locating marks were added since the field of view in the microscope is very small compared to the wafer, and it can be difficult to find the alignment marks otherwise.

If correctly aligned the final test structure consist of overlapping squares, as seen in figure 31. One square is made up of EBL-patterned chrome gratings, while the second square is the UVL-patterned aluminum masking layer.

On each substrate, we placed 10x10 such structures, with a variety of grating periods ranging from 40 nm to 100 nm, and some dose test patterns.

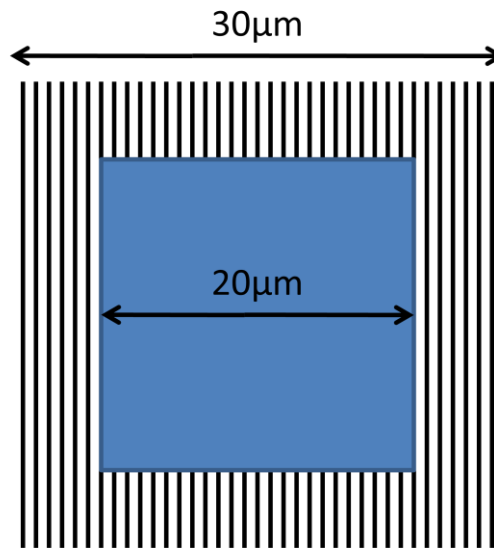


Figure 31. Schematic of the electron-beam (black) and UV (blue) patterns. The UV pattern is reversed during lift-off, so everything outside the blue square will be covered with aluminum. In order to allow for possible alignment inaccuracy, the electron-beam pattern extends 5 μm beyond the UV pattern in all directions.

The grating pattern is $30 \times 30 \mu\text{m}^2$, while the aluminum mask opening is only $20 \times 20 \mu\text{m}^2$. This creates a 5 μm overlap on all sides, which allows for some degree of miss alignment, and ensures that only central parts of the grating pattern is used, since the edges can include some pattern distortions due to proximity effects.

Fabrication scheme

The fabrication process consists of two parts: The fabrication of the mask, and the subsequent fabrication of the superlens stack. A 100 nm ZEP520A (3.6%, Zeon Corp., Tokyo, Japan) layer is

spin coated onto a 4 inch fused silica substrate, followed by thermal evaporation of a 15 nm aluminum, which helps to prevent charge accumulation during the EBL step. The grating pattern was proximity corrected, and exposed using a 100 kV JEOL JBX-9300FS EBL tool, with a dose of $150 \mu\text{C}/\text{cm}^2$, a current of 0.6nA and a spot size of 4 nm. After exposure, the aluminum layers was removed by a 1 minute submersion in undiluted MF-322 (Rohm and Haas, Coventry, UK), and the ZEP resist was developed for 2 minutes in ZED-N50 (Zeon Corp.) developer, followed by an IPA rinse. A brief O_2 descum process was carried out to remove any residual resist. Subsequently, an RIE process based on fluoride chemistry was used to etch 50 nm into the silica. Then 50 nm Cr was embedded into the fused silica by electron-beam deposition, and the wafer was immersed into Remover 1165 (Rohm and Haas) with ultrasound for 2 hours, which dissolves the ZEP layer. Next, the wafer was placed in an HMDS-oven, and 1.5 μm of the positive photoresist AZ5214e was spin coated on. The resist was exposed in an I-line aligner with a dose of $70 \text{ mJ}/\text{cm}^2$ through a mask with $20 \times 20 \mu\text{m}$ windows, and subsequently developed. A 40 nm aluminum cover was thermally deposited to block all light that does not go through the quartz/chrome mask from reaching the mr-UVL 6000 layer, and an AFM measurement was performed to find the exact thickness of the aluminum layer. The AZ5214e layer was removed in acetone, which marks the conclusion of the mask structure. The next step is the superlens stack, which consists of a 40 nm Topas planarization layer, a 35 nm silver layer and 70 nm mr-UVL 6000. The thickness of the mr-UVL 6000 is chosen to minimize waveguiding within the resist layer. First 300 nm of Topas was spin coated onto the wafer. It was then etched in an oxygen-based RIE process for 2 minutes, and given a 1 min oxygen plasma treatment in a plasma asher to planarize the surface and to reflow the Topas. The thickness of the Topas layer was measured by ellipsometry, and the profile across the mask areas was measured by AFM. By combining this information with the height of the aluminum layer and the etch rate, the remaining etch time was estimated. The wafer was then RIE etched again, and given 1 min oxygen plasma. The thickness was measured by ellipsometry to $40 \text{ nm} \pm 2.5 \text{ nm}$, and the RMS roughness over a $5 \times 5 \mu\text{m}$ area was measured by AFM. Finally a 35 nm silver layer was deposited by electron-beam deposition at a rate of $1.5 \text{ \AA}/\text{s}$, and 70 nm of mr-UVL 6000 was spin coated on top, which concludes the fabrication process.

A schematic of the fabrication process, along with all the process parameters, and an explanation of the individual steps, can be found in Appendix A.

Silver deposition

Since the quality of the silver thin film is a key aspect of the superlensing, we carried out a series of experiments to improve it. The first thing we tested was the dependence on deposition rate, which turned out to be a key parameter. In order to do this, we deposited a 35 nm silver layer on a silicon substrate, which we had covered with a PMMA film, in order to replicate the surface properties of the final structure as closely as possible. (Note: these experiments took place before PMMA was replaced by Topas as the planarization layer of choice, but proved accurate even after the change). The depositions were carried out by electron-beam evaporation. The deposition rate was varied between 0.5 Å/s and 10 Å/s, and showed a global minimum in the roughness at a rate of 1.5 Å/s, as seen in figure 32

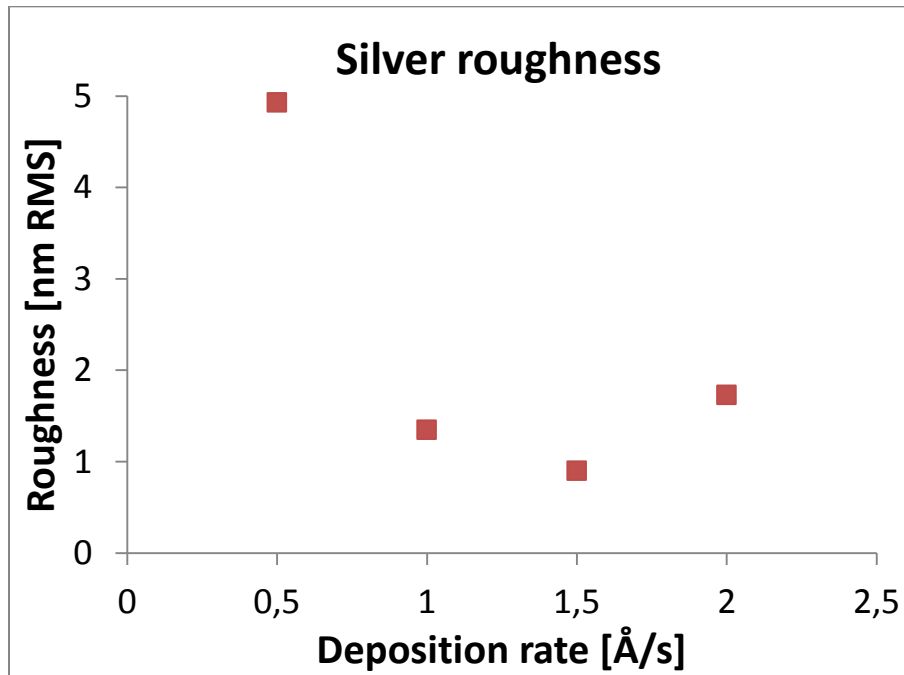


Figure 32. Graph showing the RMS roughness as a function of deposition rates. The experiments were carried out by electron-beam evaporation on a PMMA surface.

Since the deposition rate is such an important parameter, it is very important to accurately control it during deposition. As a result, only chambers with the quartz crystal monitor placed in front of the shutter could be used, since changing source conditions make it otherwise

impossible to establish a precise deposition rate prior to opening the shutter. Furthermore, it proved necessary to use a dedicated silver source for these experiments, since previous use at high deposition rates was found to significantly degrade the source material, which resulted in a poor film quality.

Changing the deposition pressure below the chamber requirements of $2 \cdot 10^{-6}$ mbar had no noticeable effect, and it was not possible to use substrate heating or cooling in the process chamber.

In addition to the use of electron-beam evaporation, we also tested thermal evaporation, but ultimately abandoned it. This decision was made because the result, though quite nice, proved to have poor reproducibility.

Substrate characterization

At various steps during the fabrication process, the substrate was characterized in order to verify that the parameters were within specifications, and to optimize the process to ensure that this was the case.

In order to check the uniformity of the chrome grating, SEM scans were performed, an example of which can be seen in figure 33. As seen, the grating is very uniform over the entire $20 \times 20 \mu\text{m}^2$, which is due in part to successful proximity correction, and in part to the fact that the design does not utilize the outer edges of the chrome grating, which is covered with the aluminum surrounding layer.

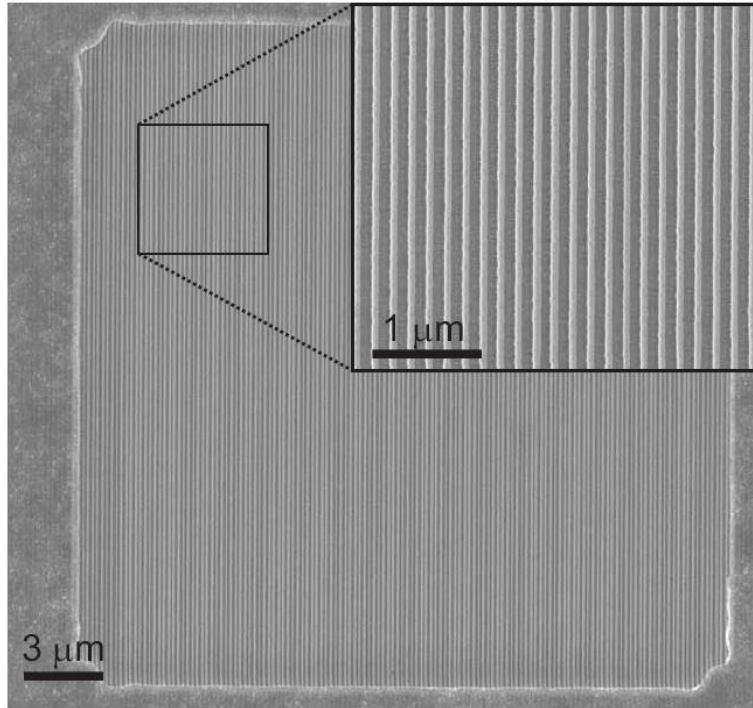


Figure 33. SEM image showing the embedded chrome gratings and surrounding aluminum layer. The chrome grating has very high uniformity and low line-edge roughness. Some corner defects can be observed in the aluminum layer, but these are not relevant to future measurements, which take place in the center of the exposed grating pattern.

Furthermore, AFM scans were carried out to get a detailed look at the surface morphology, some examples of which can be seen in figure 34.

The chrome gratings would normally display a height variation of 50 nm, but with the use of the RIE step to embed them, this has been reduced to 12 nm. Further reduction is possible with careful optimization of the process, but was not necessary for this particular application. After spinning on the Topas and etching it down to 40 nm, a second AFM scan was performed, which shows that the grating structures are no longer visible, and the roughness is fairly low at only 0.4-0.5 nm RMS. In order to achieve this low roughness, it proved necessary to use ultrasound on the polymer solution immediately prior to spinning it on. This is due to the fact that the cyclo-olefin copolymer molecules consist of two different parts, each with its own polarity, which leads to the formation of large micelles structures over time, and substantially increases roughness. The ultrasound treatment works by dispersing these micelle structures.

Finally, a third AFM scan was performed after depositing the silver layer, in order to confirm that the metal roughness was within tolerances before proceeding with further tests. A cutoff value of 1 nm RMS was used, with poorer quality samples being discarded.

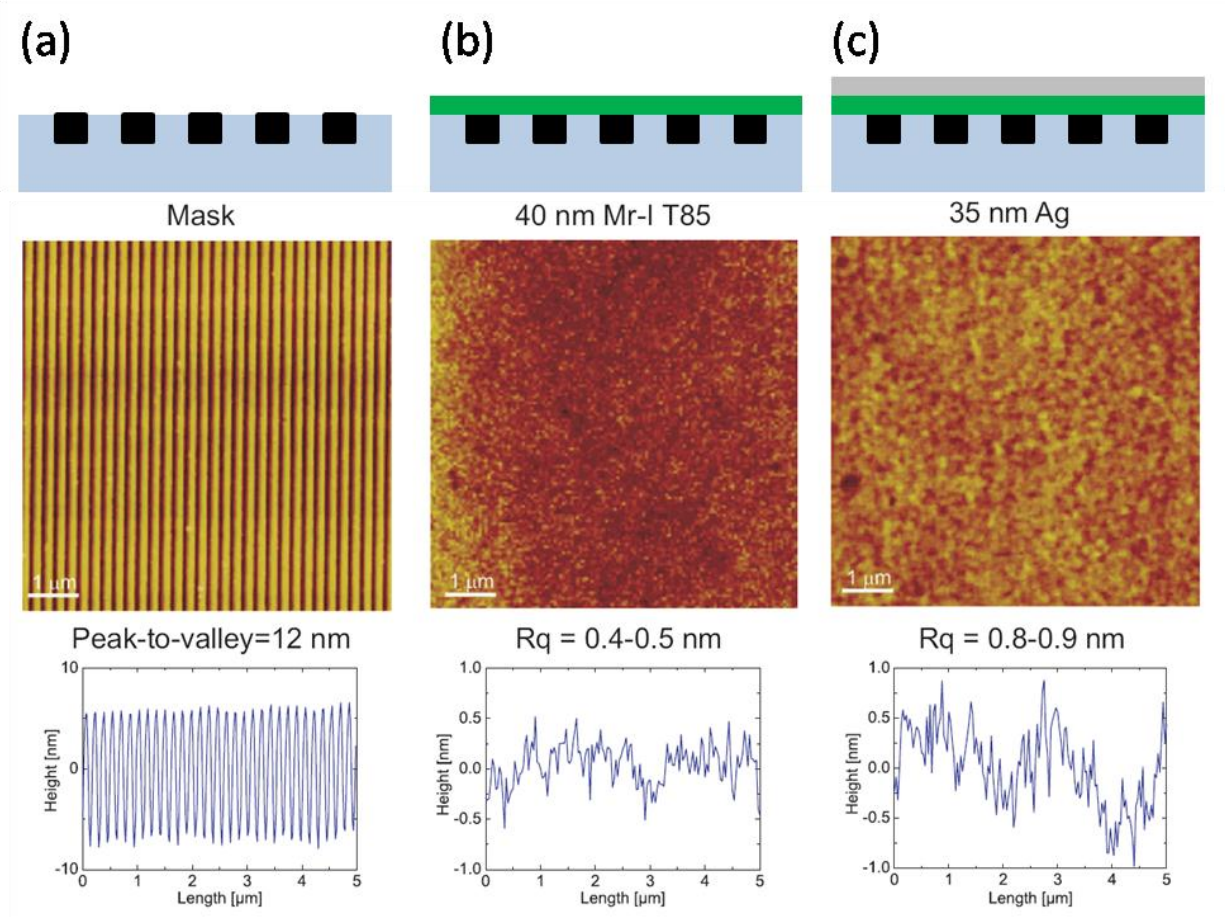


Figure 34. AFM scans showing the surface morphology at three steps of the fabrication process. The height variation for the 50-nm chrome grating (a) was greatly reduced by embedding it, though it is still clearly visible with a peak-to-valley height of 12 nm. After adding the planarizing Topas layer (b), the grating structure is no longer visible, and the roughness is below 0.5 nm RMS. Adding the silver layer (c) increases the roughness moderately, though it still remains below 1nm RMS.

Exposure tests

We measured the dose-response curve through a 35 nm silver layer by determining the retention height for various exposure doses. The result can be seen in figure 35.

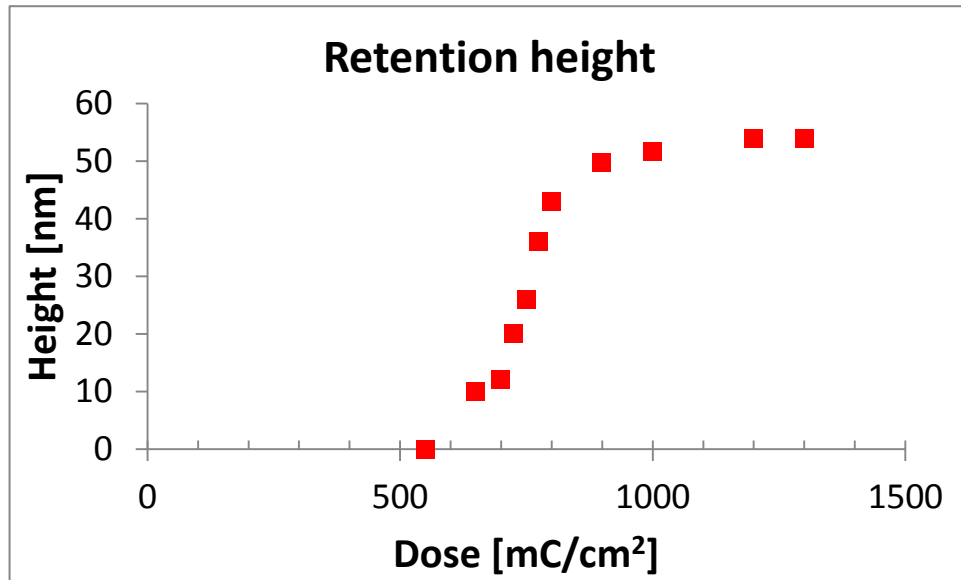


Figure 35. Graph showing the retention height for mr-UVL 6000 as a function of dose. The experiments were carried out using I-line (365 nm) UV lithography, and the exposure was done through a 35 nm silver layer in order to replicate the final structure as closely as possible.

In an effort to improve the imaging, we chose a dose corresponding to a retention height of half the initial photoresist thickness, since this coincides with the maximum slope of the dose curve, and should give us the largest contrast. We also tested different doses around this point, but did not observe any improvements in contrast as a result thereof.

AFM characterization

AFM scans were carried out in tapping mode, with a constant field size of $2 \times 2 \mu\text{m}^2$, and a frequency of 1Hz. The scans show areas located centrally over the grating areas.

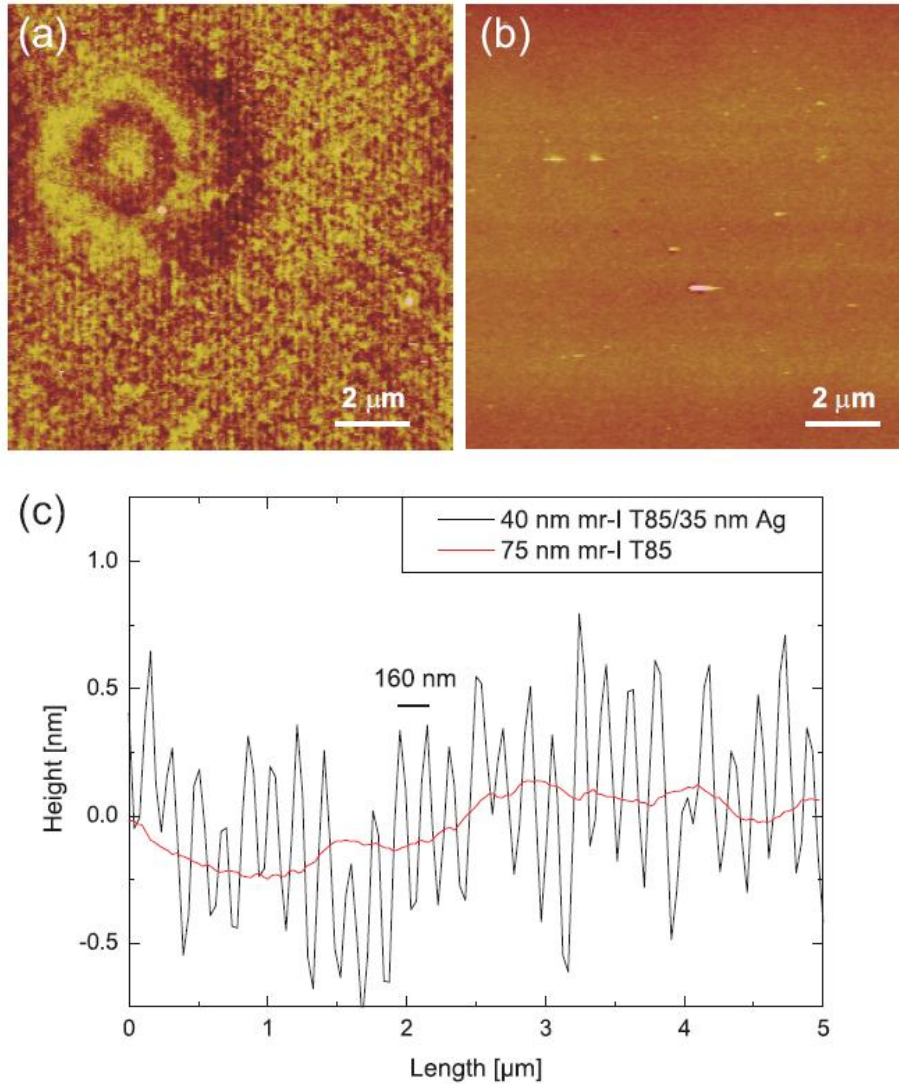


Figure 36. AFM scans of the superlens sample (a) and control sample (b). Comparing the two it can be seen that the superlens is clearly able to resolve the subwavelength grating pattern, while the control sample is not. Panel c shows a comparison of cross-sections averaged over the entire scan.

AFM characterization of the exposed photoresist shows a line pattern with a periodicity equal to that of the grating. To verify that this periodic structure is achieved through the superlensing effect, a control wafer was made where the silver layer had been replaced by Topas. The control samples have an identical distance between mask and resist, yet no periodic pattern could be observed.

The evanescent wave has a characteristic decay length:

$$Z = \frac{1}{4\pi} \frac{1}{\sqrt{a^{-2}\epsilon\lambda^{-2}}}$$

where a is the period, ϵ is the dimensionless permittivity, and λ is the free-space wavelength. Using the parameters of the final structure ($a=80$ nm and $\lambda=365$ nm) we get a decay length of 17 nm, meaning that the field intensity is reduced to $1/e = 0.37$ of its original value within the first 17 nm of the mask. After 75 nm the evanescent wave intensity will be negligible, and all subwavelength information will be lost. Thus the presence of the periodic pattern in the photoresist proves, that the subwavelength information has been restored by the superlensing effect, and can therefore be observed much further from the object.

Out of the different patterns exposed, the 80-nm grating was the easiest to identify, while the 70-nm grating was less clear, which might be caused by the silver roughness, since there is an inverse proportionality between resolution and surface roughness [28].

While the periodic grating is clearly visible in the exposed resist, the grating is of a lower quality than the original mask, which indicates that the superlens was unable to fully restore all the Fourier components, likely due to decaying higher order components. Furthermore, the photolithographic method used here represents a less than ideal means of capturing the light intensity at the object plane, since the resist dose-response curve is not linear. Additionally the image is degraded by the roughness of the silver layer and local substrate defects.

As seen from the AFM scan the peak to valley distance of the exposed photoresist is only around 1 nm, which can be attributed to several factors. Much of it is due to residual layer exposure, which is expected to account for more than half of the resist height, assuming that the threshold of the resist is reached at half the maximum intensity. Furthermore, some diffusion of the generated photo acid is expected during exposure and the subsequent baking steps, which will have the unavoidable effect of blurring the image. Finally, pattern defects will occur as a result of height variations in the Topas layer and surface roughness.

Chapter 4 - Near-field transfer of an optical hotspot

This chapter will cover the fabrication and testing of plasmonic nanoantenna arrays, the subsequent deposition of superlens layers, and finally optical characterization of the coupled nanoantennas-lens system at the visible wavelength of 633 nm via scanning near-field microscopy.

Optical hotspots are essential for a range of important bio-, chemical- and medical-sensing applications, including surface enhanced Raman scattering [11] and enhanced fluorescence [50], and it has been shown theoretically that an optical hotspot can be translated through a near-field superlens [13]. Such a setup would be preferable to direct contact, which has been shown to cause structural and functional changes in biomolecules [51], including denaturation of proteins [52]. Furthermore, too close proximity with metal nanoparticles can cause the fluorescence to be quenched rather than enhanced [53].

It should be noted that chronologically this chapter represents the final work in the thesis, and that it differs from the rest, by not being designed to achieve impedance matching between the lens and host. This choice was made since there is still some dispute over the exact matching condition (see superlens theory section), so we chose to proceed with a design based on numerical modeling.

Superlens design

The superlens design was based on Comsol modeling performed by Zhengtong Liu at Purdue University. This modeling used a chrome grating to simulate lens performance at a resolution of 100 nm (the grating half pitch).

The results from numerical simulations indicate that subwavelength resolution might be possible without impedance matching, with $\lambda/6$ resolution achieved for a single layer silver lens with a SiO₂ host (see appendix B).

The highest contrast was achieved for a 3 layer design, but the transmission is very low for this configuration. As a result, a single layer design was chosen, since it provided the best compromise of contrast and transmission. This design consists of a 20 nm silver layer covered on both sides by 21 nm SiO₂ layers.

While not in the model, a 1 nm germanium adhesion layer was added, in order to lower the silver roughness and decrease loss. The germanium layer itself is not expected to add much loss, due to the very low thickness and relatively low loss at 633 nm [54].

Along with the superlens covered samples, a number of reference samples were made, where the silver layer had been replaced with an equivalent thickness silicon dioxide layer, in order to check the near-field distribution without a lens at the same distance.

Pattern design

In order to test the near-field transfer of optical hotspots, a nanoantenna pattern was designed, which produces very high local field intensities, when illuminated with correctly polarized light. The antenna design is based on pairs of identical rhombus shaped metal structures, with a narrow gap between the two, in which the highest intensity is found. This choice of design was due to existing expertise from previous work [50].

The nanoantenna pairs were fabricated by electron-beam evaporation of silver, with a thin germanium adhesion layer to improve metal quality. They were embedded in a fused silica substrate, by means of the same RIE process used earlier for the chrome grating, but with the metal thickness and etch depth changed to 40 nm. A schematic of such an antenna pair can be seen in figure 37.

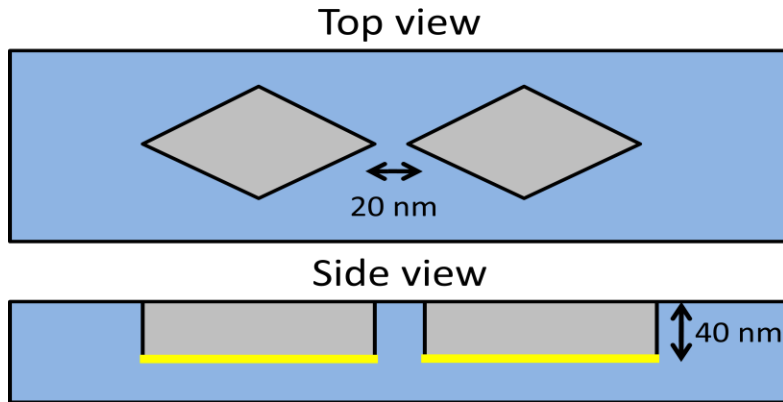


Figure 37. Schematic of the basic nanoantenna design. Two 40 nm thick rhombus shaped antennas form a single pair, and are spaced 20 nm apart.

Each individual antenna has a characteristic size X , which is the length of the minor axis. The major axis is twice as long, and the second antenna is placed along this axis, with a gap of 20 nm separating the two. For simplicity, light polarized along the major axis (across the gap) will be referred to as parallel, while light polarized along the minor axis will be referred to as perpendicular.

The antennas pairs were arranged in large $500 \times 500 \mu\text{m}^2$ arrays, in order to enable far-field characterization of the optical resonances. Within such an array, the antennas are spaced with a periodicity of $4X$ along the minor axis, and $8X$ along the major axis, an illustration of which can be in figure 38.

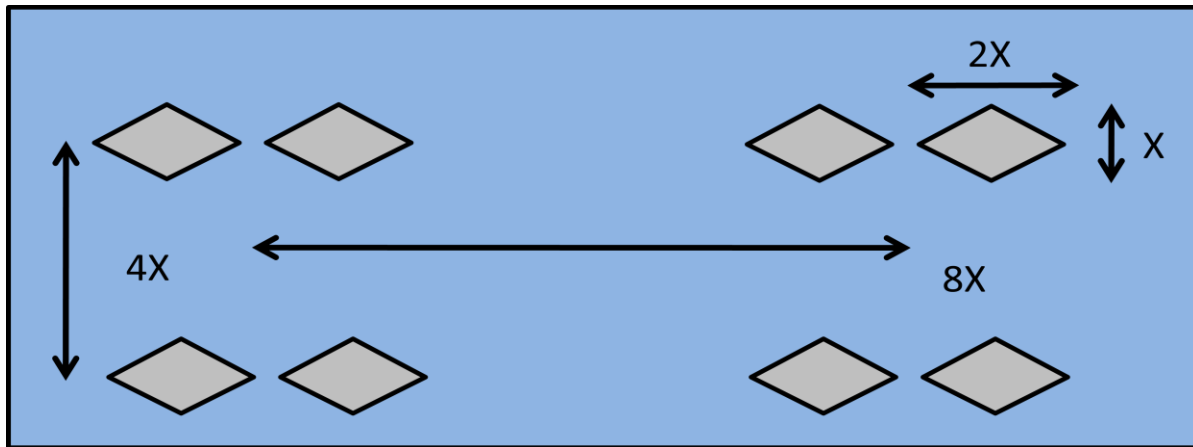


Figure 38. The individual antennas pairs are part of larger arrays, which is necessary to allow for far-field characterization. The size of individual antennas is related to the spacing of the array, which is done to keep area coverage constant. The size parameter X can be varied in order to achieve different resonance wavelengths.

The decision to make the spacing proportional to the antenna size, was based on a desire to keep the total metal coverage constant for arrays of differently sized antennas. This is important because it keeps the strength of the observed optical resonance nearly constant, thus making it easier to compare different arrays.

Arrays with a variety of antennas sizes are needed, in order to cover a range around the design wavelength of 633 nm, which is why the pattern was designed with 12 individual arrays on each sample. The 12 arrays are arranged in two groups of 6 arrays, with the antenna sizes ranging from 50 to 100 nm in 6 steps. The two groups use identical mask designs, but they were exposed with different dosages during EBL, in order to create slightly different sizes in the final fabricated devices. The result is a small shift in resonance frequency between the two. A schematic of the sample design can be seen in figure 39.

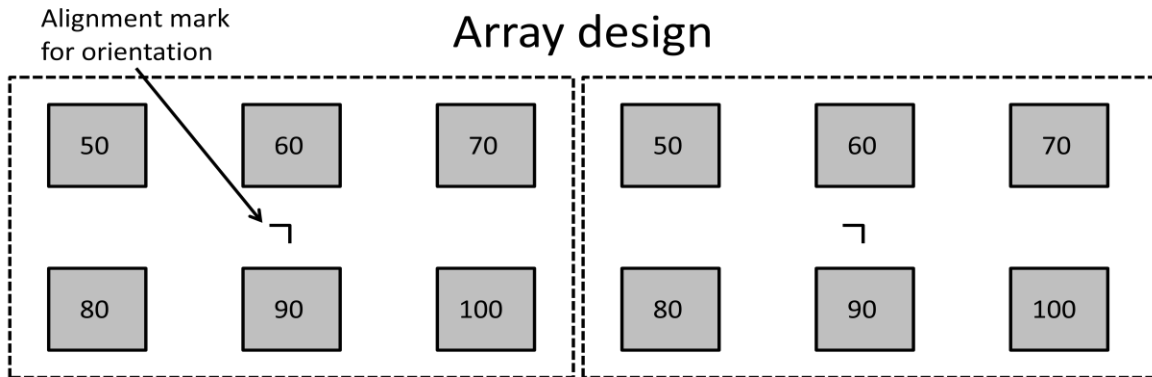


Figure 39. Each $2 \times 2 \text{ cm}^2$ sample contains a total of 12 arrays. The arrays are $500 \times 500 \text{ }\mu\text{m}$, and X ranges from 50 to 100 nm in 6 steps. Two geometrically identical groups of 6 arrays are included, with the left one having an exposure dose of $300 \text{ }\mu\text{C}/\text{cm}^2$, while the right one has a dose of $350 \text{ }\mu\text{C}/\text{cm}^2$. Alignment marks are added to indicate the correct rotation.

A complete recipe for the nanoantennas fabrication, as well as subsequent deposition of superlens/reference layers, can be found in appendix A.

Structural characterization

In order to verify the quality of the fabricated samples, a number of tests were performed, which focused on the antenna shape, the planarization and the quality of the silver layer.

The first such test was SEM imaging of the antenna arrays, an example of which can be seen in figure 40. The antenna shape was generally well reproduced, though the finite size of metallic

grains does lead to a rounding of the edges, particularly for the smallest antennas ($X = 50$ nm). This also causes some variation in the gap size, which varies between 10 and 30 nm.

The arrays are generally very uniform, with no missing antenna pairs.

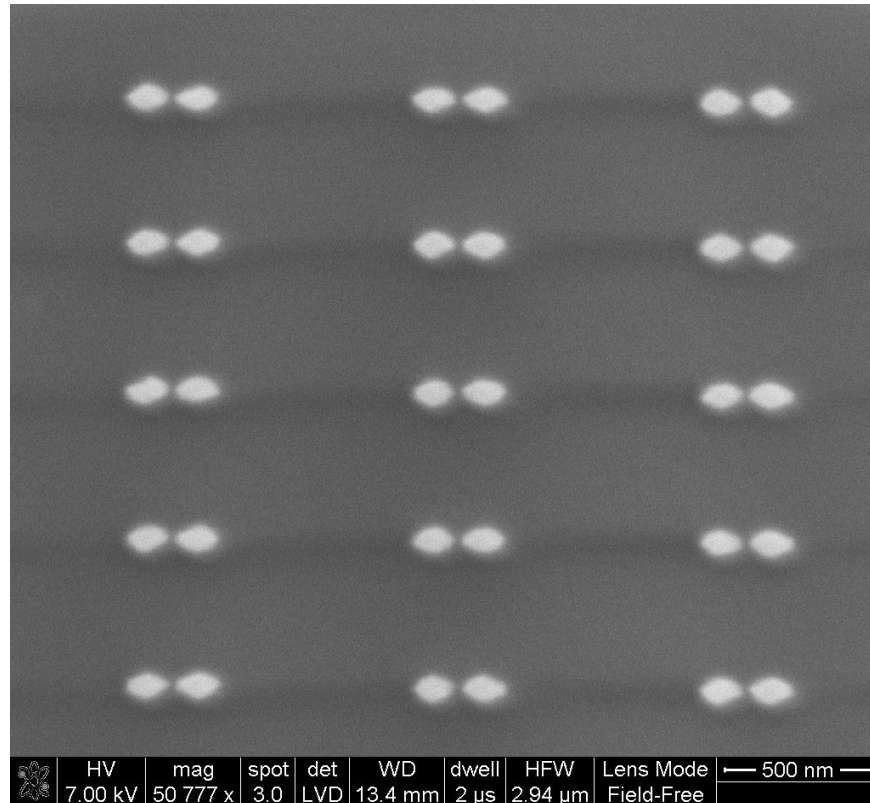


Figure 40. SEM image of a nanoantenna array ($X = 80$ nm). The pattern is well reproduced, with a gap size around 20nm, though some variation in antenna shape can be observed, which can be ascribed to the grain size.

The second test was AFM imaging of the embedded nanoantennas. The embedding was generally very good, with the average height variation between antennas and substrate being less than 5 nm. However, some lift-off defects could be observed, an example of which can be seen in figure 41. In these areas, metal defects around the edges of the antennas can be seen, with height variations of 10-20 nm.

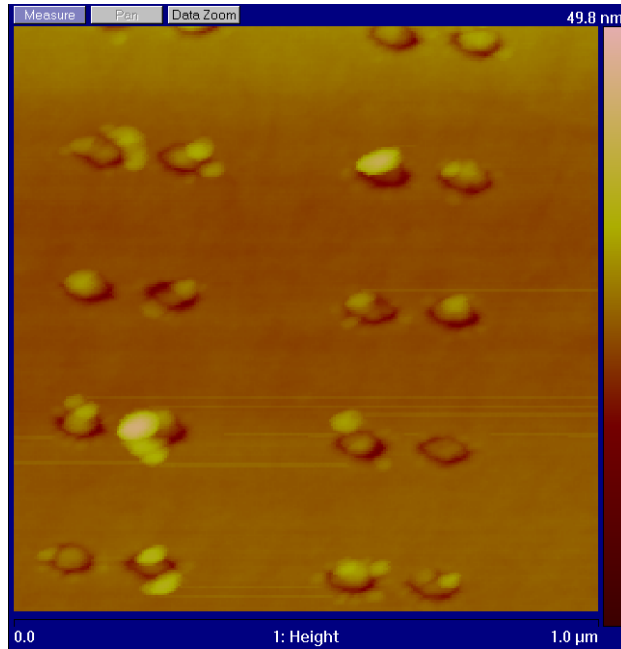


Figure 41. AFM image of a nanoantenna array ($X = 80$ nm). Some defects can be observed around the edges of the antennas.

Finally the quality of the deposited superlens layer was tested, by performing AFM scans of the silver surface. This was done on a test sample with no SiO_2 cover layer, in order to allow direct access to the silver. The results, which can be seen in figure 42, show good film uniformity, with a small grain size and a low roughness of 0.5 nm RMS.

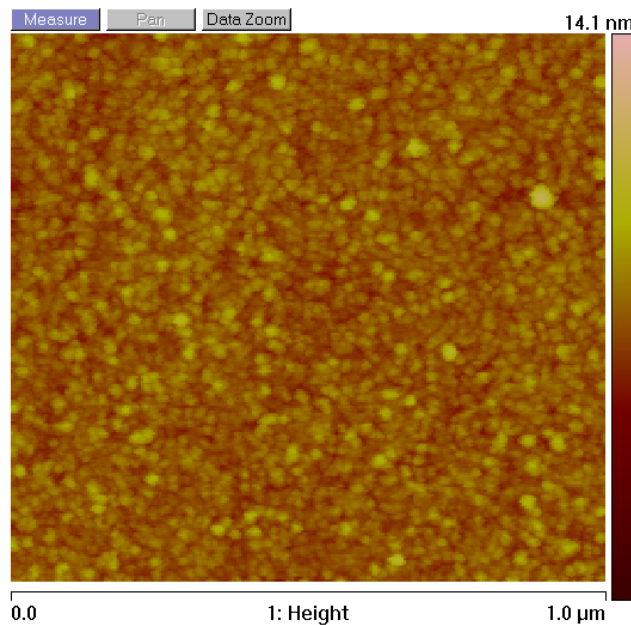


Figure 42. AFM image of the silver lens layer. The film shows good uniformity, and has a low roughness of 0.5nm RMS.

For test purposes, silver films with the same thickness were also deposited directly on SiO_2 , with no germanium adhesion layer, and the results show a much higher surface roughness of 2.7 nm RMS.

Optical Characterization

The nanoantenna resonances were characterized optically, through the use of a far-field setup in transmission mode. The setup used a supercontinuum light source from Koheras, which emits light over a broad range from 500 to 2000 nm. The light was output through a photonic crystal fiber, and focused by a parabolic mirror. The focal point was directly on the sample surface, with a spot size of 2-300 μm .

A linear polarizer was placed in the light path between the mirror and the samples.

After passing through the sample, the light was refocused by a second parabolic mirror, and coupled in to a photonic crystal fiber, which was connected to a spectrometer.

The sample was mounted on an XYZ-stage with micrometer controls.

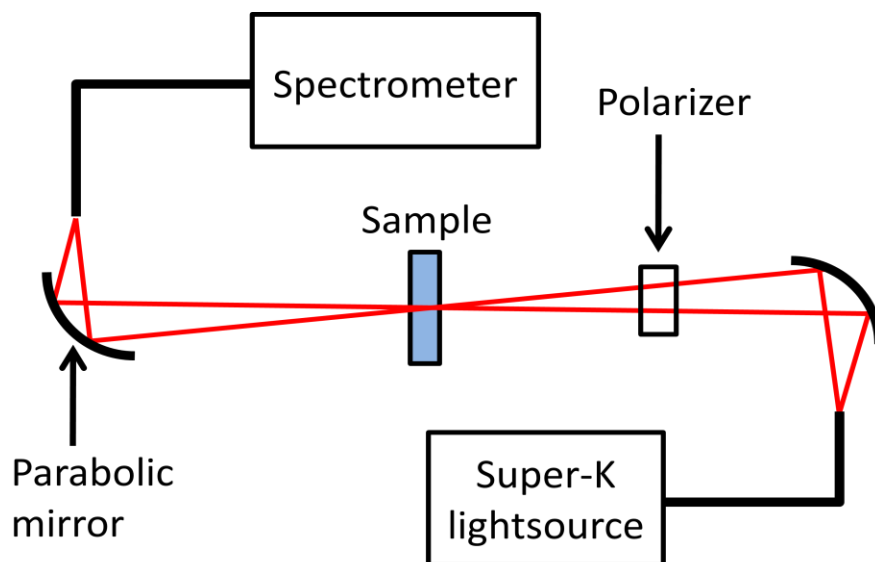


Figure 43. Schematic of the optical setup. A supercontinuum light source was used to provide coherent light across a broad spectral range. Twin parabolic mirrors were used to focus the beam at the sample surface, and to couple it in and out of the photonic crystal fibers.

When measuring, the individual arrays were aligned in two steps: First the beam was centered on the array by eye, which was followed by an initial broadband measurement. Once the

resonance wavelength had been determined, a continuous measurement at the resonance wavelength was performed, and the micrometer screws were to align the array, in such a way as to maximize the size of the resonance peak. Afterwards, a final broadband measurement was taken.

Reference measurements were taken through the sample, in an area free of visual defects, and outside any of the arrays. The reference intensities (in dB) were then subtracted from the array intensities, in order to give a relative transmission measurement.

The results show that each of the twelve nanoantennas arrays has a distinct resonance peak, with a position that depends strongly on size and polarization. As expected from theory [29] [30], a strong resonance was seen for light polarized parallel to the long axis of the antennas, and it this resonance, that is of interest here. A weaker resonance was seen for light polarized orthogonal to the long axis of the antennas pairs, with a resonance wavelength that was blue shifted compared to the strong resonance. The wavelengths of the primary resonance can be seen in table 1, with values ranging from 490 to 730 nm, which covers a wide range around the design wavelength of 633 nm.

Table 1. Measured resonance wavelength for each of the twelve nanoantenna arrays.

X [nm]	Dose [$\mu\text{C}/\text{cm}^2$]	Resonance [nm]
50	300	490
	350	500
60	300	510
	350	570
70	300	560
	350	590
80	300	610
	350	620
90	300	660
	350	680
100	300	700
	350	730

The spectra for all six arrays with a dose of $300 \mu\text{C}/\text{cm}^2$ can be seen in figure 44.

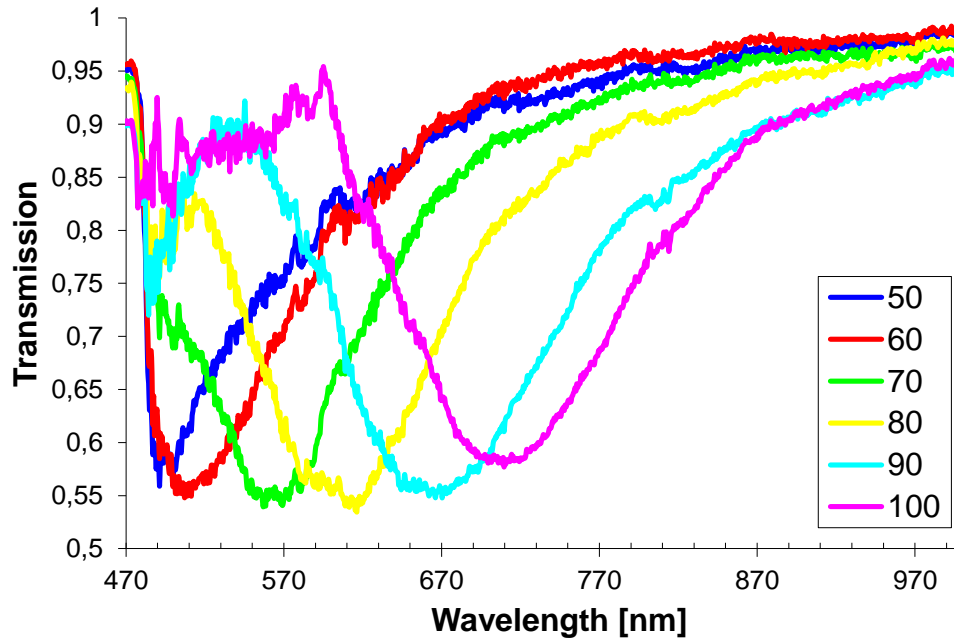


Figure 44. Transmission spectra for six different nanoantennas arrays, with X ranging from 50 to 100 nm. Each of the six spectra shows a strong resonance, at a wavelength which depends on the antenna size.

The full width half maximum (FWHM) of the resonances varied from 50 to 100 nm, with larger antennas generally having a broader resonance.

Resonance shift

A second set of optical measurements were performed after deposition of the superlens/reference layers, and they revealed a significant change in the spectra. For the reference samples, a moderate red shift was seen. This is to be expected, since the SiO_2 covering increases the refractive index around the antennas (compared to air). The red shift was around 40 nm for all the arrays.

For the superlens covered samples, a different phenomenon was observed, as shown in figure 45. Here the red shift depends on the resonance frequency of the antennas. Antennas with a resonance around 500 nm underwent no resonance shift, while antennas with a resonance around 700 nm shifted by as much as 100 nm, due to coupling between the antennas and superlens.

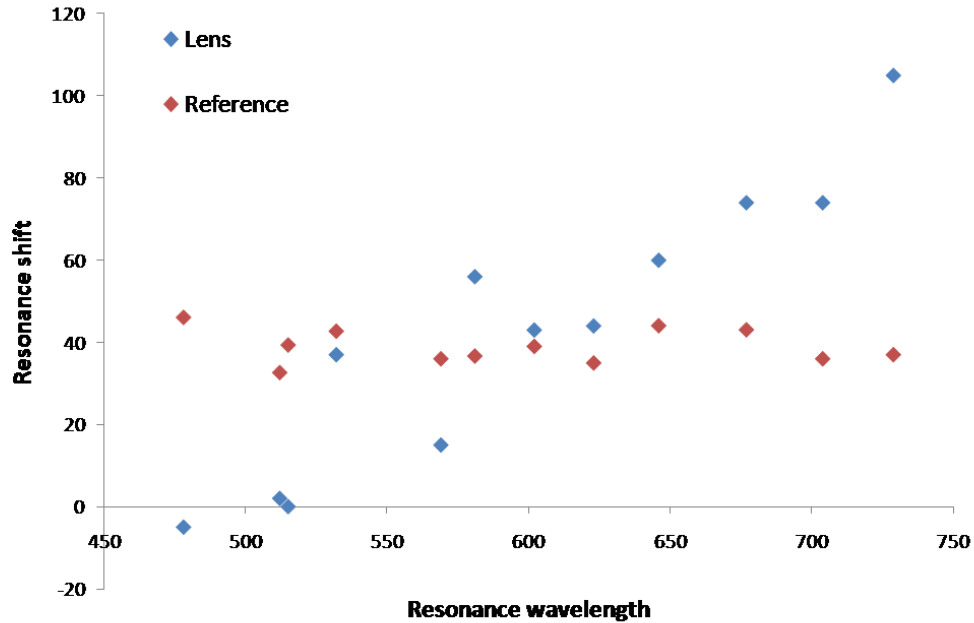


Figure 45. Graph showing the resonance shift for various antenna arrays, as a function of their resonance wavelength. A clear wavelength dependence can be seen for the lens samples, while the shift appears constant for reference samples.

As a result of this shift, the reference samples have a different resonance wavelength than the superlens samples, even for otherwise identical antennas. Around the area of interest (~633 nm) the difference is slight, but for antennas outside this range the difference is significant, which complicates direct comparisons between lens and reference samples.

Near-field optical characterization

The SNOM scans shown here were carried out by other project members Mark Thoreson at Erlangen University and Paul West at Purdue University.

The setup at Erlangen University used an acusto-optic tunable filter, in combination with a supercontinuum light source, to enable the selection of any wavelength from 450 to 700 nm. Furthermore, this setup included a linear polarizer. The setup used at Purdue University had a higher spatial resolution, but was limited to 633 nm light, and the polarization could not be controlled.

Schematics of these two setups, as well as the measurement procedure, can be found in Appendix C.

The SNOM measurements focused mainly on the array with $X = 80$ nm and a dose of $350 \mu\text{C}/\text{cm}^2$, since its 620 nm resonance is closest to the design wavelength of 633 nm. Scans were also performed on the array with $X = 80$ nm and a dose of $300 \mu\text{C}/\text{cm}^2$, but only at Purdue.

For the array with a resonance wavelength of 620 nm, scans were taken at wavelengths ranging from 530 to 680 nm, in steps of 30 nm. These measurements were done on superlens samples as well as reference samples and bare nanoantenna samples, and both parallel and perpendicular polarization was used, in addition to non-polarized light. The array with a resonance of 610 nm was only measured at 633 nm with non-polarized light.

Due to the gradual degradation of SNOM tips over time, and issues with the alignment of the tip relative to the center of the incident laser spot, the measured intensity values cannot be compared directly between scans. Furthermore, the SNOM software performs an automatic linear shift of the intensity scale, in order to center the data at zero.

When scanning the antennas under perpendicularly polarized light, no resonance can be seen, which is consistent with earlier far-field measurements, and the antennas simply block part of the incoming light. Thus antennas appear as regions with lower intensity, an example of which is shown in figure 46. The resolution is sufficient to see individual antenna pairs, but not individual antennas.

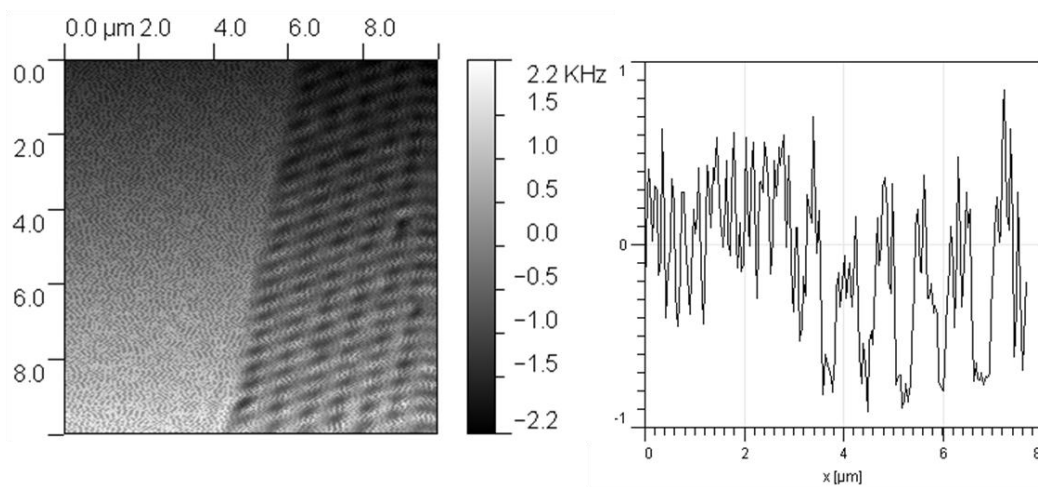


Figure 46. SNOM scan (left) and cross-section (right) of an off-resonance antenna array (620 nm light with perpendicular polarization). The individual antenna pairs can be observed as dark regions, since they block some of the transmitted light.

When illuminating the array with parallel polarization, a periodic enhanced of the intensity is observed. This resonance has a periodicity equal to the array periodicity, it overlaps with the light that is simply transmitted through the sample, and its peak intensity is well above that of the incident light. However, this is not the nanoantenna resonance, which can be seen in two ways. Firstly, comparing the AFM and SNOM data, shows that the highest intensity regions are in the areas between antennas. Secondly, when looking at the edge of an array, it can be seen, that the periodic enhancement extends well beyond the boundaries, as seen in figure 47. This behavior shows that the resonance is actually a propagating mode, and thus not the nanoantenna resonance, which is highly localized.

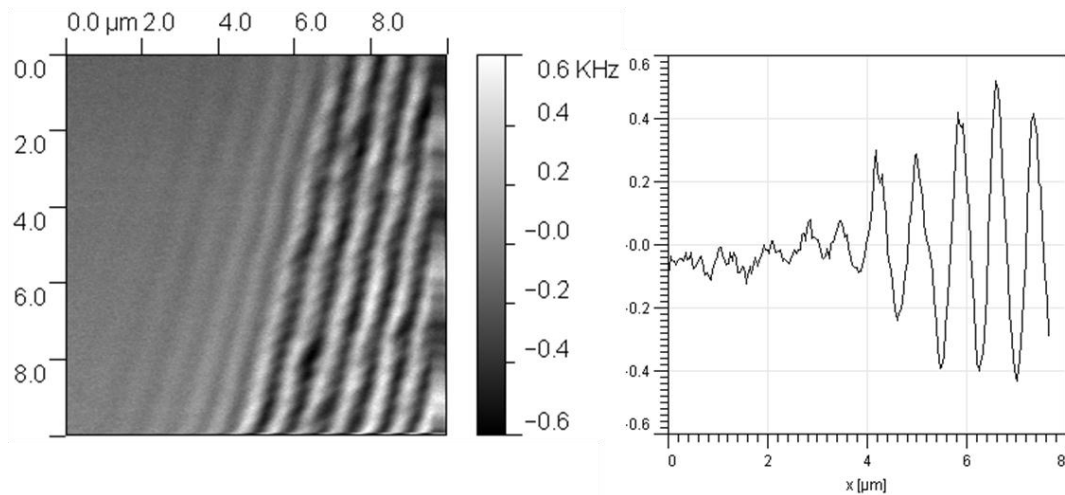


Figure 47. SNOM scan (left and cross-section (right) of an antenna array. A periodic resonance can be seen, which extends well beyond the boundaries of the array, and decay from it. The peak intensities are significantly higher than that of the incident light.

It has been shown that coupled nanoantenna resonances die out when the distance between particles exceeds 2.5x the particle size [29], which is why the nanoantenna arrays used here, have a spacing of 3x the particle size (corresponding to a 4X distance from center to center). However, for silver nanoantennas this had the unintended consequence of producing a periodicity ($8 \times 80 = 640$ nm), that is very close to the resonance wavelength. As a result, the nanoantenna array is essentially a grating with a periodicity of λ in one direction, and $\lambda/2$ in the

other direction, and such gratings have been shown previously to couple light from free space into propagating surface or waveguided modes [55] [56].

Furthermore, during earlier far-field measurements, it was noted that when illuminating one of the arrays with white light, colored light was emitted at the edges of the sample. This is consistent with a grating effect, which would couple light with a certain wavelength into a propagating mode on the sample. An illustration of this effect can be seen in figure 48.

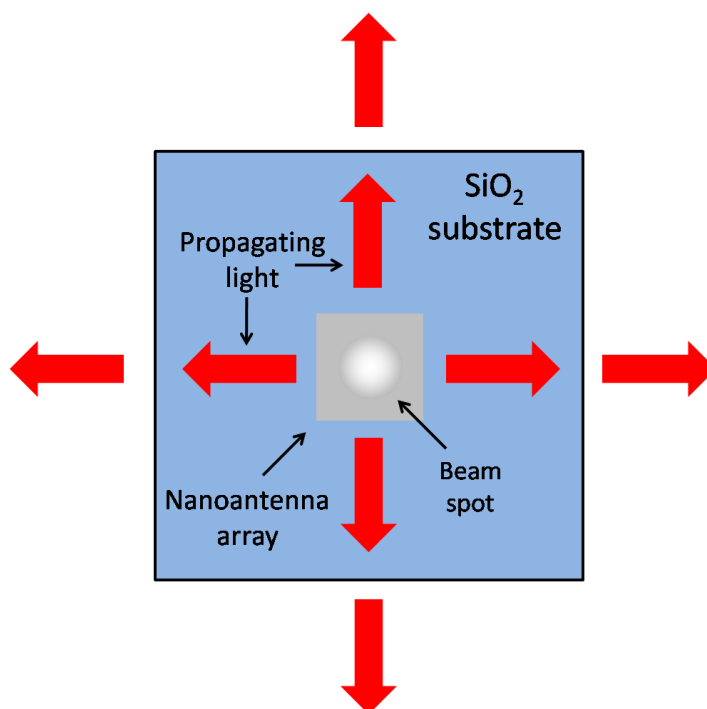


Figure 48. Illustration of the observed grating coupling effect, showing a top view of the sample. A beam of white light hits the nanoantenna array at an angle perpendicular to the surface plane, and causes the emission of colored light at the sample edges.

This mode seems to be propagating inside the silica sample itself, which acts as a waveguide due to its high refractive index compared to the surrounding air.

A different field enhancement was observed near the expected resonance wavelength of 664 nm (620 nm + 44 nm shift). Here a second resonance seems to appear, with the same spacing as the periodic mode described earlier, but shifted half a period. As shown in figure 49, this resonance is not present at 620 nm, it can be seen as very low intensity peaks at 650 nm, and it

grows in strength at 680 nm. At 680 nm it reaches roughly the same intensity as the propagating mode, which gives it the appearance of a simple doubling in frequency.

No scans were performed at longer wavelengths, since the limit of the setup had been reached, so it is not know if the intensity grows further at longer wavelengths.

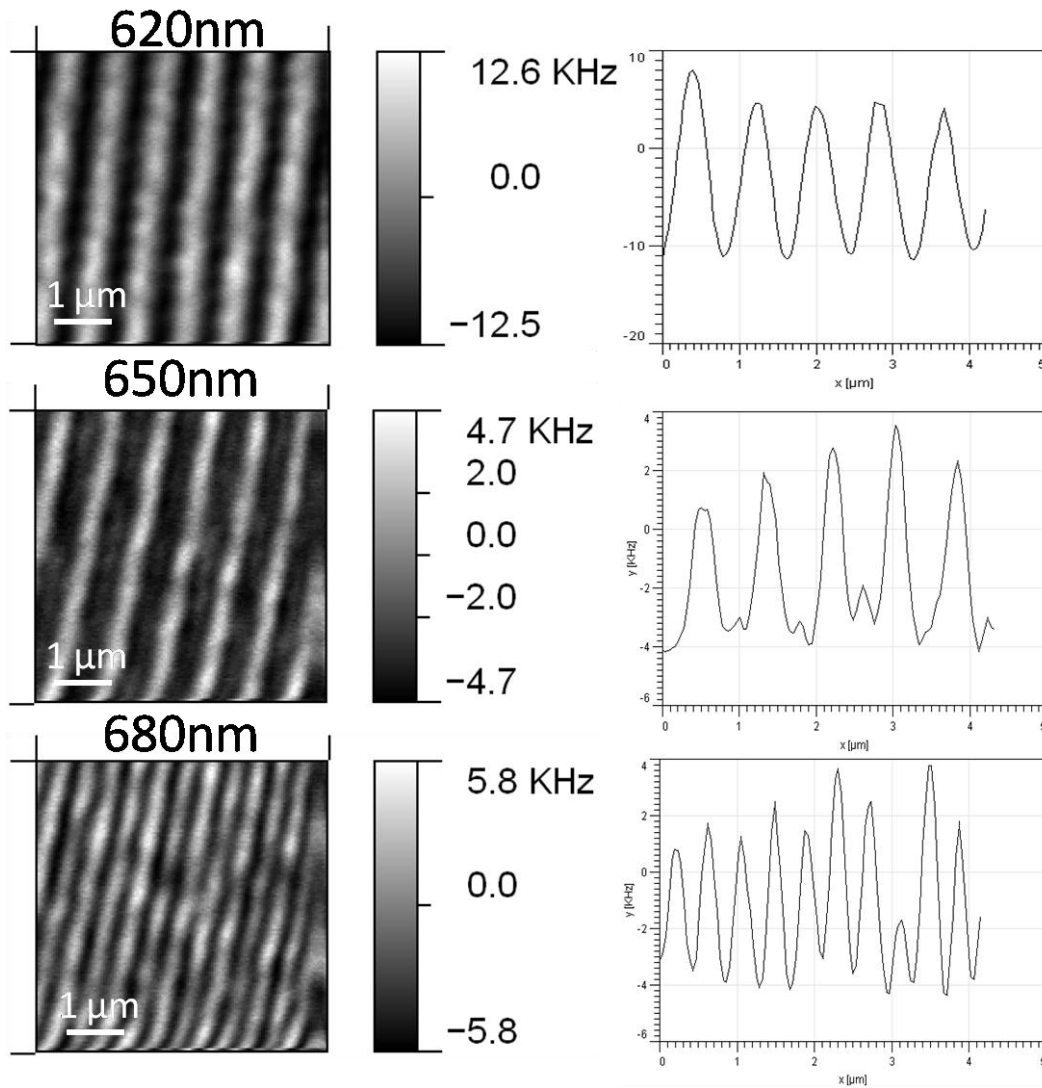


Figure 49. SNOM scans of the intensity profile for three different wavelengths. At 620nm only the propagating mode is seen, at 650 nm a second weaker mode starts to appear, and at 680nm it has grown in strength to equal the propagating mode.

In addition to the appearance of this second resonance, it can also be seen that the width of the intensity peak drops significantly.

In order to investigate the origin of this second resonance, a scan was performed using the same wavelength but perpendicular polarization, and the results show no sign of the resonance was seen. Furthermore, identical scans were taken on the reference sample, to see if this effect was related to a superlensing effect, and once again no secondary resonance was observed. These scans can be seen in figure 50.

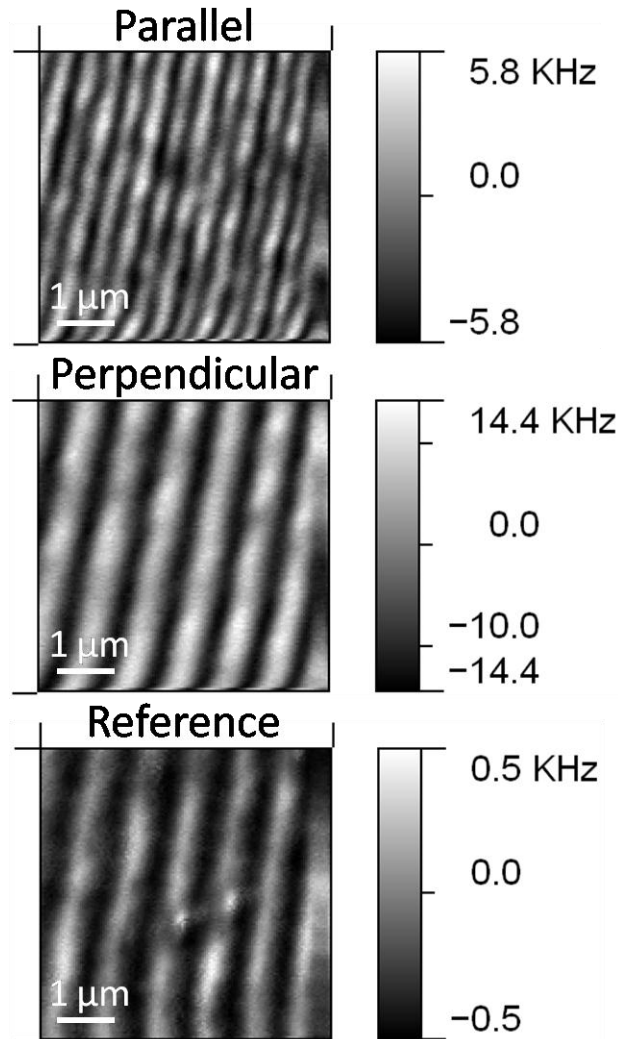


Figure 50. Comparison of the intensity profile for the same array under three different conditions. In addition to the propagating mode, a second mode is observed for parallel polarization on a superlens sample (top), which causes the appearance of a frequency doubling. No such mode is observed for perpendicular polarization on the same sample (middle), or parallel polarization on a reference sample (bottom).

Thus there are two main phenomena to be considered: The appearance of the second resonance, which occurs only at a specific wavelength and polarization, and the narrowing of the intensity peaks.

There are three possible contributions to the intensity pattern seen here:

1. Light transmitted through the sample in areas between the antennas
2. The grating-coupled propagating mode
3. The localized field enhancement from the nanoantennas

Since the secondary resonance appears very close to the expected resonance frequency of the nanoantennas, and only at the correct polarization, it appears to be the nanoantenna resonance. Furthermore, the narrowing of the intensity peaks would be consistent with an increased extinction cross-section for the nanoantennas at resonance, which would have the effect of “stealing” light from the surrounding area.

These results suggest that this new field enhancement is the localized nanoantenna resonance, and that the superlens allows it to be resolved, which is not possible on the reference sample. However, due to the close similarity to the propagating mode, no firm conclusions can be made at this point, as further experiments are needed, which will be discussed in the outlook portion of the conclusion.

Chapter 5 - Metal-dielectric composites

This chapter will deal with the experiments to investigate the properties of metal dielectric composites, and their potential use as a superlensing material instead of conventional metals like silver.

Permittivity calculations

In order to calculate the permittivity for a variety of MDC materials and investigate, how it depends on wavelength and filling factor, a matlab script was written based on Bruggeman's EMT formula [32]. Since the permittivity, wavelength and filling factor are inherently interconnected, the results cannot be easily summarized in a single 2D graph. However, some clear conclusions emerge from the calculations, which will be shown here.

#1. Permittivity matching

By selectively altering the filling factor of a MDC, it is possible to tune the permittivity. As a result, it is possible to match the permittivity of a given host material, by simply changing the filling factor accordingly [13]. Since these are dispersive materials, the match will only exist at one particular wavelength.

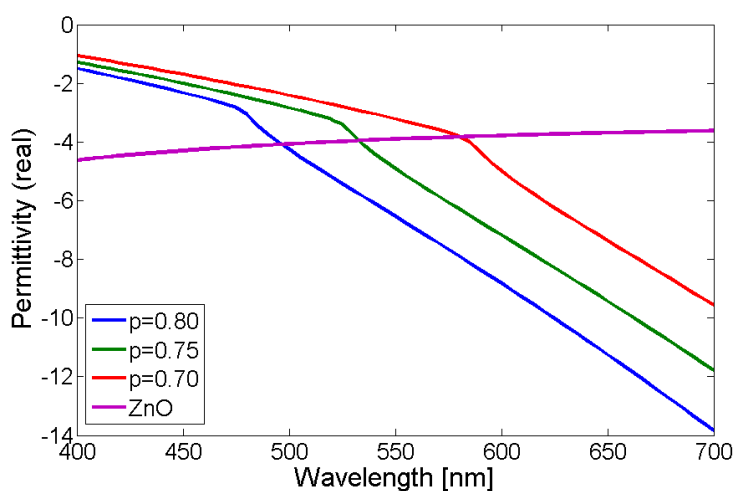


Figure 51. Graph showing the permittivity for 3 different Ag/SiO₂ MDCs. As seen the permittivity can be tuned to match a potential zinc oxide host at various wavelengths, ranging from 495 to 585 nm in the examples shown. The sudden shift in permittivity, which can be seen for each of the composites, corresponds to a change in the imaginary part.

#2. Absorption band

The EMT calculations show a distinct, increase in the imaginary part of the permittivity below a certain wavelength, which depends on composition and filling factor. This region, which will be referred to as the absorption band, has a loss that is far too high to be useful for superlensing, which arises from surface-plasmon interactions between individual grains [57]. Above this wavelength the loss is quite low, and very similar to that of pure silver.

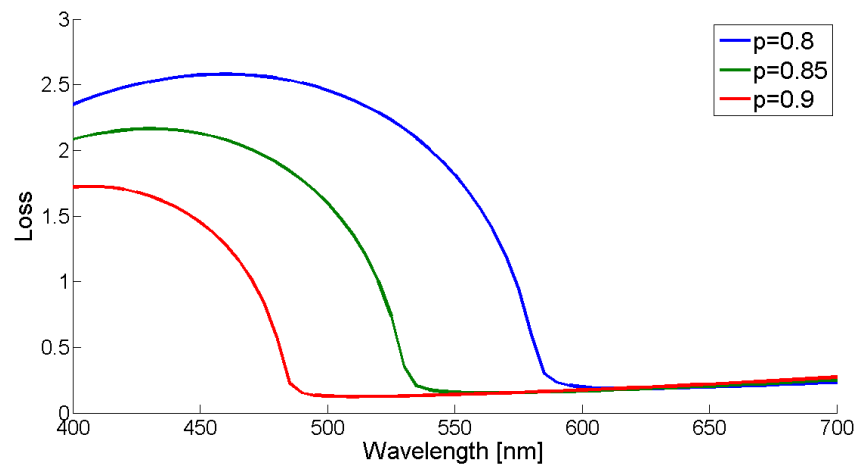


Figure 52. Graph showing the loss (imaginary part of the permittivity with reversed sign) for an Ag/ZnO MDC with various filling factors. A broad absorption band is seen at lower wavelengths, while higher wavelengths exhibit low loss.

Theoretical studies have shown that this absorption band is particularly large for spherical particles, and that adjusting the shape to any other form may help lower it [57].

#3. Superlens design

Using the EMT calculations it is possible to design a superlens system for a particular application. While the permittivity of the MDC can be changed over a wide range, the tunability is not unlimited. However, the range can be extended significantly by employing different host materials depending on the desired operational wavelength, an illustration of which can be seen in figure 53.

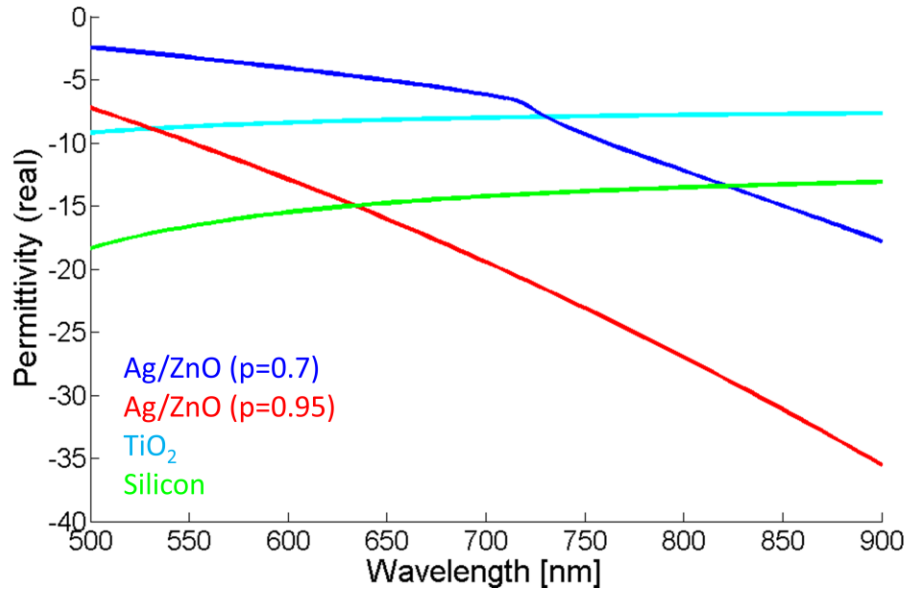


Figure 53. Graph showing the permittivity for two different Ag/ZnO MDCs, with filling factors that correspond to the outer limits of the usual range. For a TiO_2 host, this would enable tuning between 530nm and 730nm, while a silicon host would enable tuning between 635 and 820nm. Thus by changing the host material, it is possible to extend the range of tunability.

For the purpose of this thesis, an operational wavelength of 633nm was desired (see chapter 3), which can be realized by using a Ag/ZnO MDC with a TiO_2 host, as shown in figure 54

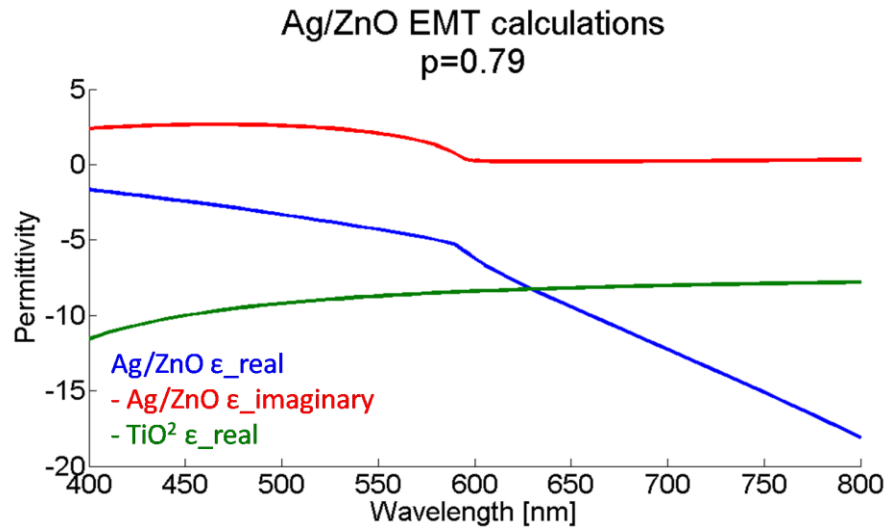


Figure 54. Graph showing the calculated permittivity for an Ag/ZnO composite with $p=0.79$. The permittivity matches a TiO_2 host at 633nm, and shows a low (-0.2) loss.

Fabrication method

Previous studies of MDCs have used a variety of fabrication methods, including sequential electron-beam deposition of the metal/dielectric layers [58], pulsed laser beam deposition from mixed metal/dielectric targets [59], and alternating deposition from several sputtering targets [60]. The fabrication method developed here, was based on the desire to allow a wide variety of materials to be combined in a way, which would create a uniform distribution in 3D, while at the same time allowing the filling factor to be adjusted freely. In order to achieve this, sputtering was chosen as the deposition method, and multiple guns were employed at the same time to create a uniform distribution, an illustration of which can be seen in figure 55. Since the guns are placed at different locations in the chamber, the substrate was continuously rotated during deposition, so as to avoid variation across the sample.

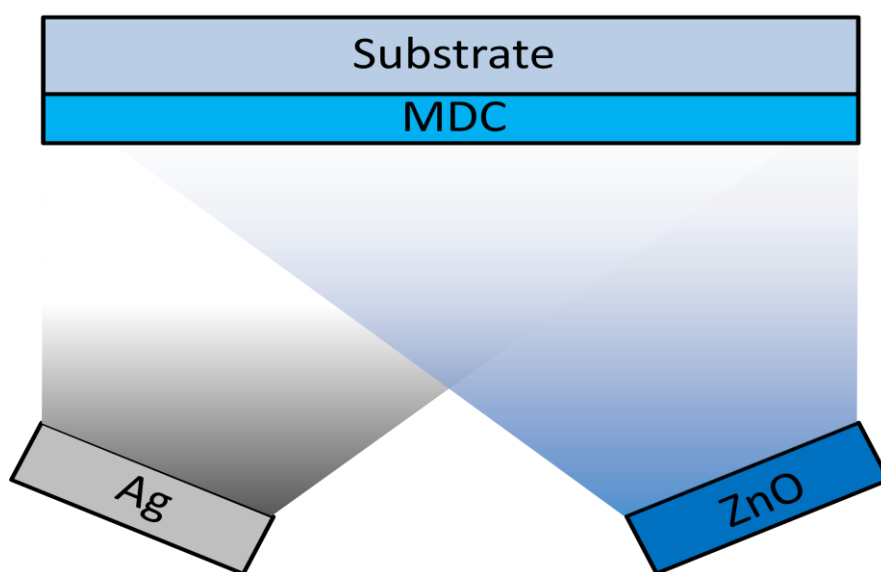


Figure 55. Schematic of the fabrication method. Metal-dielectric composites were fabricated by simultaneous sputtering from both a metallic and dielectric source, thus ensuring a uniform mixture. The filling factor, p , can be adjusted by altering the individual sputtering rates.

Material choice

The choice to use silver as the metal for our MDC was an easy one, since it has the lowest loss in the visible range, and no suitable alternatives could be found. For the dielectric, however, a number of materials were considered, with parameters such as availability, compatibility with

the fabrication method and permittivity. From these considerations we decided to test three dielectric materials: Silicon dioxide, aluminum oxide and indium tin oxide (ITO).

#1. Silicon dioxide

Silicon dioxide had been used previous by our collaborators at Purdue, and seemed like an obvious choice. However, it proved problematic when using co-sputtering. The reason for this is, that while silicon dioxide can easily be RF sputtered, the deposition rate is extremely low (less than $0.1\text{\AA}/\text{s}$), since the power has to be limited to avoid cracking the target. Meanwhile the silver deposition rate could not be decreased below $0.5\text{\AA}/\text{s}$, while maintaining stabile plasma. As a result, the filling factor would be limited to a range between 0.9 and 1, which results in an insufficient range of tunability for the permittivity.

Alternatively silicon dioxide can be deposited at a higher rate by using a silicon source, and employing a reactive sputtering method with oxygen present in the chamber. This would considerably widen the range of possible filling factors, but the presence of oxygen in the chamber would also result in significant oxidization of the silver present, which would drastically alter the properties of the deposited material.

#2. Indium Tin Oxide

ITO is conductive, which allows the use of DC sputtering rather than RF sputtering, and results in a much higher deposition rate. The filling factor can therefore be adjusted over a much wider range than that of a silver/silicon dioxide mixture, and would be suitable according to our calculations. Nonetheless, ITO was discarded as a material choice for two reasons: Firstly, mixtures of silver and ITO were determined to have a surface roughness well above our requirement of 1 nm RMS or lower. Secondly, a silver/ITO combination proved problematic when attempting to measure the composition with EDX, since tin was present in too small a concentration to be reliable, oxygen could be present in several forms (silver oxide, indium oxide, silicon dioxide, tin oxide) thus making it an inaccurate indicator, and indium has a characteristic energy very similar to silver, which makes it difficult to distinguish the two peaks.

#3. Zinc Oxide

Pure zinc oxide is semiconductor, while doped zinc oxide is a transparent conductive metal oxide [61]. It can be DC sputtered fairly easily, and the deposition rate can be varied over a large range. Furthermore our tests showed that it produces MDC films with a suitably low roughness, when combined with silver, and can easily be distinguished from silver in EDX measurements. As a result of these factors, we decided to make it the focus of our MDC study.

Fabrication details

The composite films described in this paper were fabricated in a Lesker sputtering chamber with 6 available guns, which allowed simultaneous sputtering of both materials, thus ensuring a uniform distribution.

Both silver and zinc oxide were DC sputtered with no substrate bias or heating, at a constant pressure of 5mTorr. No gases were present in the chamber aside from the argon plasma. In order to vary the composition of different films, the sputtering power for each material was varied, in order to change the individual deposition rates. With no crystal monitor present in the chamber, thickness was controlled by time alone, based on calculated deposition rates from previous samples, which had been measured using a Dektak 8 stylus profilometer.

Films used for EDX and ellipsometry were deposited on silicon wafers with thicknesses of 100-150 nm. This was done in order to provide a sufficient thickness for EDX measurements, and a metal layer thick enough to be considered a bulk material for ellipsometry purposes. Films used for roughness measurements were deposited on quartz wafers with a thickness of 35nm, in order to provide conditions close to those in the desired superlens application, and easy comparison to previous results for pure silver.

Composition measurements

In order to determine the composition of the deposited films, EDX characterization was performed using FEI Nova 600 NanoSEM and Oxford INCA software. The excitation voltage was kept constant at 10 kV with a working distance of 5 mm, in order to allow direct comparison between samples.

The EDX data shows a detailed atomic composition of the films, an example of which can be seen in figure 56. However, the data does not provide the volume composition, which is what is needed for EMT calculations. In order to convert the data from atomic composition to volume composition, bulk density and molar weight parameters were assumed for both silver and zinc oxide, and the number of atoms per unit volume was calculated. Using this value, the atomic composition was converted into the needed volume composition. Since oxygen might be on the substrates in various forms, including silver oxide, zinc oxide and silicon dioxide, it was ignored for the purpose of these calculations, and the filling factor was derived based on the amount of silver and zinc present.

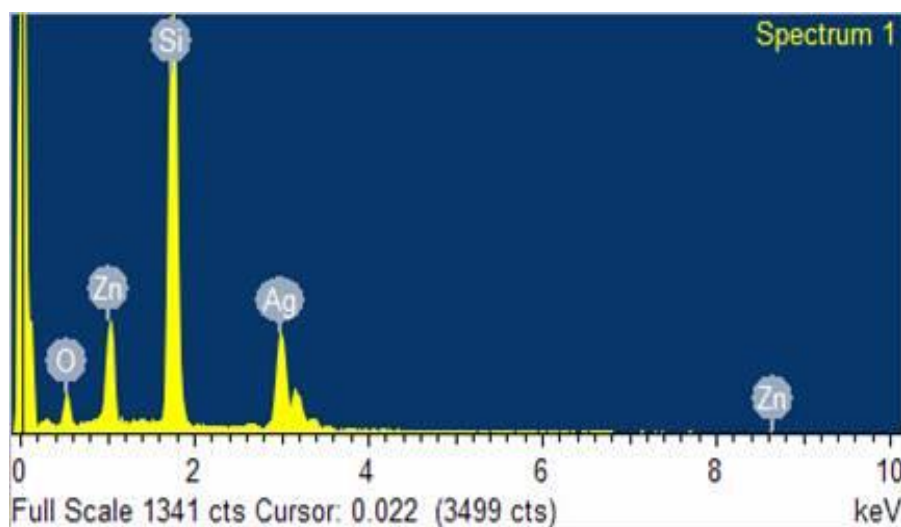


Figure 56. Results from EDX measurements on an Ag/ZnO composite film showing the number of counts as a function of energy. The large silicon peak is due to the substrate, and no contaminants were found. By evaluating the amount of silver and zinc present, it is possible to accurately calculate the filling factor.

By using the EDX data as a guideline, we were able to fabricate films with a wide range of filling factors, by altering the sputtering power for the individual guns. As seen in table 2, the fabricated films cover a range of filling factors from 0.55 all the way to 0.88, which covers the entire range of interest.

The filling factor of 0.55 represents the lowest that could be achieved with current methods, since the zinc oxide deposition rate was maxed, and the silver deposition rate was at its lowest stable value at minimum. If necessary it might have been possible to achieve a filling factor

below 0.55, but no attempts were made since such a film would be dielectric in nature, and thus of no interest for our studies. Films with a filling factor above 0.88 were not fabricated because they would be too similar to pure silver, and therefore of little interest.

Table 2. Individual sputtering powers and corresponding filling factors for different Ag/ZnO MDC films.

Ag power [W]	20	30	40	50	60	70	80
ZnO power [W]	75	75	75	75	75	75	50
P	0.55	0.65	0.72	0.77	0.79	0.84	0.88

For most films a zinc oxide sputtering power of 75W was used, since this was the maximum power allowed in order to avoid the risk of cracking the target. Even at this power the deposition rate remained fairly low, at around 0.3Å/s. The silver deposition rate, on the other hand, could be ramped very high (over 50Å/s), but could not be lowered further than around 0.5 Å/s while maintaining a reasonably stable plasma. This being the case, the different ratios were achieved by keeping the zinc oxide deposition rate constant, while varying the silver deposition rate accordingly.

The only deposition that used a zinc oxide power other than 75 W was the one for a filling factor of 0.88. Here the power was lowered to 50 W. This was done because it would otherwise have been necessary to use a high silver deposition rate, which was found to increase roughness.

Film roughness

AFM measurements of the composite films were carried out in tapping mode, with a constant field size of 2x2 μm^2 , and a scan rate of 1 Hz. Some additional scans with a smaller field size of 500x500 nm^2 were carried out in order to determine the grain size, an example of which can be seen in figure 57. The results show that the roughness remains below 1 nm RMS for filling factors between 0.7 and 0.9, generally considered a good benchmark for a high quality metal

film. Outside this range the roughness appears to increase for lower filling rates, and it is important to note that the roughness is also significantly higher for a filling factor of 1, corresponding to pure silver.

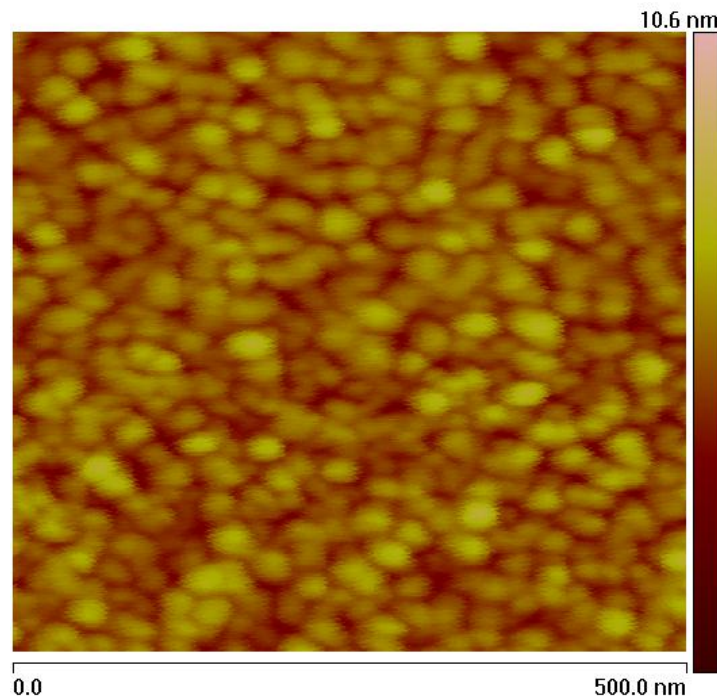


Figure 57. AFM scan of Ag/ZnO MDC film with a filling factor of 0.88. The measured RMS roughness is 0.8 nm, and the grain size is ~20 nm.

This behavior can be ascribed to a fairly simple phenomenon. Normally, when silver is deposited on a surface with a large wetting angle, like the fused silica substrates used here, it will form islands that grow until the percolation threshold is reached, at which point they merge and form a continuous but very rough film [62]. This island growth leads to a large grain size, which results in a high surface roughness. If, however, zinc oxide is deposited simultaneously, it appears to have the effect of interrupting island growth, leading to the formation of many small grains, rather than a few large grains.

In an effort to test the feasibility of further reducing the roughness, experiments were performed using a thin germanium wetting layer, which has proven effective for pure silver [63]. In the case of an Ag/ZnO composite, however, no significant effect of the wetting layer could be observed, and the roughness stayed constant the same for a given filling factor with

and without the Germanium. This indicates that the roughness is inherent to the composite growth, rather than being dominated by the surface interaction, as is normally the case for thin metallic films.

Optical characterization

For the optical characterization a M-2000V spectroscopic ellipsometer from J.A. Woollam was used. This ellipsometer was mounted directly on the sputtering chamber, meaning that measurements could be performed in vacuum conditions immediately after deposition. Unfortunately, the in-situ mounting meant that the angle was fixed at 70° , and could not be varied between measurements to get additional data.

The deposited films were thick enough to be opaque, meaning only a single interface could be probed. As a result, no thickness parameter was used, since the films could be treated as bulk material, and all fits were carried out on a wavelength by wavelength basis.

The ellipsometry measurements confirm, that it is possible to tune the real part of the permittivity, with the fabricated films covering practically all of the range between the value for pure silver and zero, as seen in figure 58. Thus, for any desired combination of permittivity and wavelength in this range, it would be possible to calculate the required filling factor, and fabricate a composite material, that meets this goal.

Unfortunately, the loss is quite a different story. Here we find that for all of the fabricated films, the loss is far higher than that of pure silver, with lower filling factors showing the highest loss. Thus, the further the permittivity is shifted from that of pure silver, the higher the resulting loss gets. This appears to be an innate tradeoff when working with an Ag/ZnO composite, and it differs greatly from the predictions made by effective medium theory. Similar behavior was seen for the Ag/SiO₂ composites fabricated by our collaborators at Purdue University [58] [64].

Unfortunately, at present there is no theory available to accurately describe this behavior.

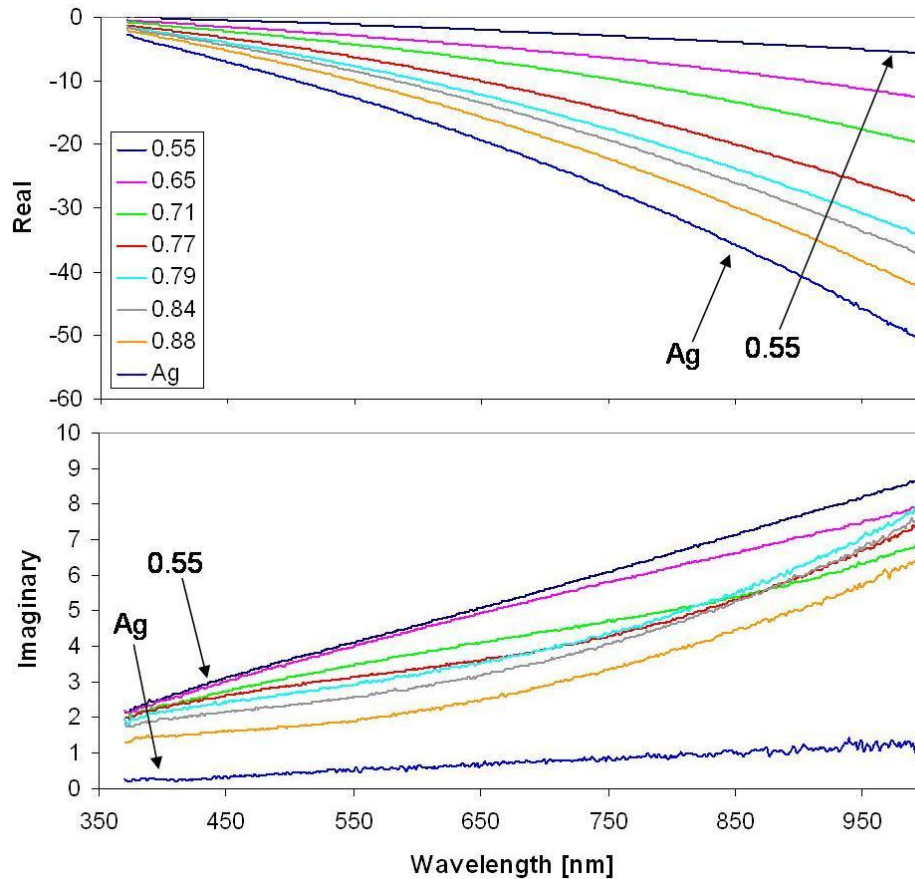


Figure 58. Graph showing the real and imaginary parts of the permittivity Ag/ZnO films for a variety of filling factors. The real part is seen to be smoothly tunable, covering a range from zero all the way to that of pure silver. The imaginary part (loss) increases with decreasing filling factor, and remains much higher than for pure silver at all times.

In addition to looking at the properties of composite films in vacuum, a study of their change, once exposed to air, was also carried out, the results of which can be seen in figure 59. The measurements show that the composite film undergoes an immediate change, once the chamber has been vented, and continues to gradually change over the next hours and days. Exposure to air has the effect of making the real part of the permittivity less negative, as well as reducing the loss. This behavior is consistent with a gradual oxidation of the silver.

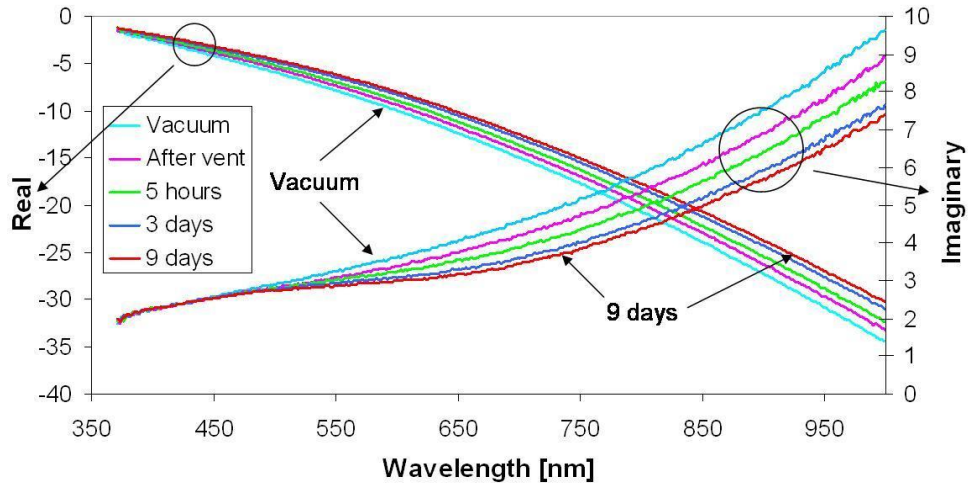


Figure 59. Graph showing the change in permittivity over time, for a composite with $p=0.77$. The real part is seen to increase over time, while the loss decreases. This is thought to be caused by gradual oxidation of the silver.

Nanoantennas

In order to create a reference for comparison, the nanoantenna characterization started with pure silver antennas. The silver antennas fabricated all showed a clear size dependant resonance, when using light with the E-field oriented across the gap between nanoantennas, and no resonance for the orthogonal polarization. The resonance wavelength ranged from near UV to telecom wavelengths, depending on the size of the antennas. Unfortunately, the setup used only allowed measurements at wavelengths from 500 nm and upwards, meaning the near-UV resonances could not be properly characterized. They were, however, clearly visible in a standard microscope, with the array appearing violet in color, due to increased reflection at the resonance wavelength.

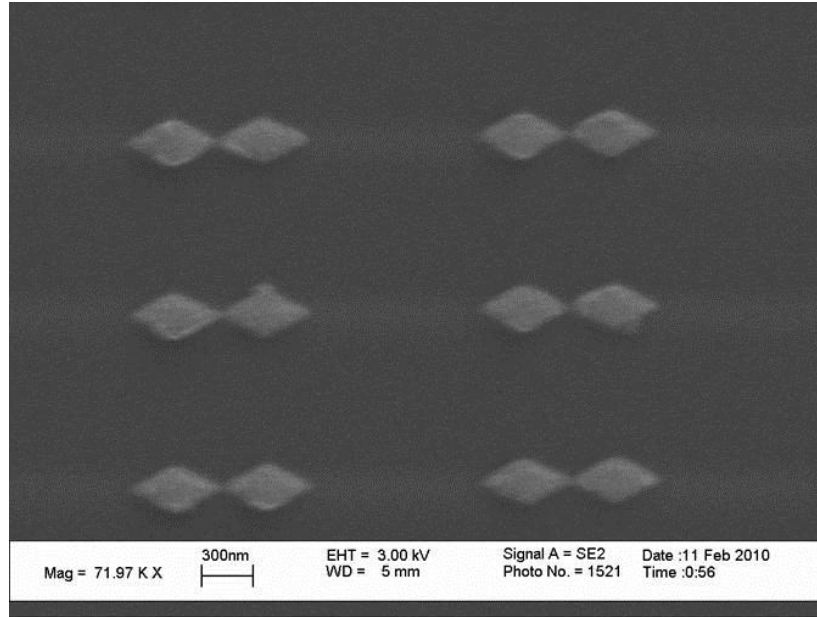


Figure 60. SEM images of the fabricated composite nanoantennas. The image shows antennas with X equal to 250 nm.

Optical characterization of composite antennas shows similar behavior to pure silver antennas, which shows that this can indeed be seen as a diluted metal, but there are two clear differences. For arrays of the same size, the resonance for composite antennas is red shifted several hundred nanometer, which is consistent with ellipsometry measurements showing that the real part of the permittivity is less negative. Additionally, the resonances are much wider than those for pure silver, which can be attributed to higher loss, also consistent with ellipsometry results shown earlier. An additional broadening effect might arise from local variations in permittivity, which would cause each antenna pair to resonate at a slightly different frequency than that of its neighbors. These trends can be seen in figure 61.

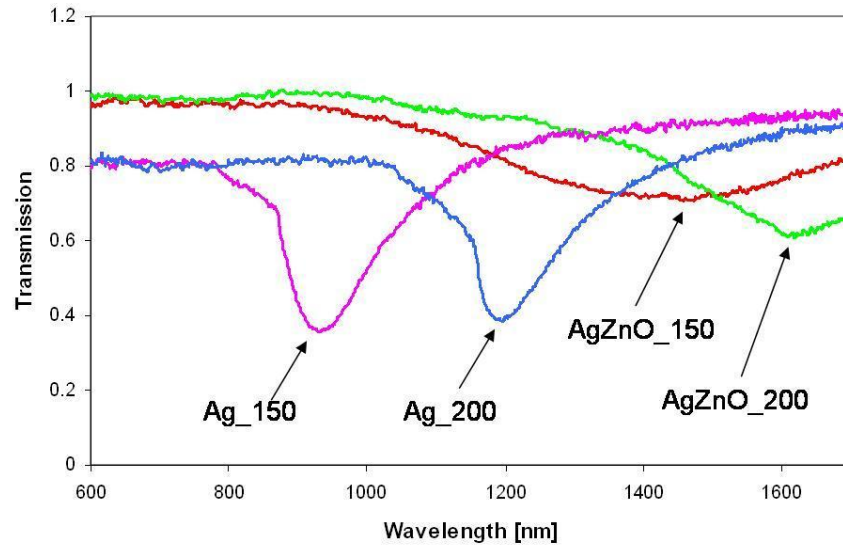


Figure 61. Graphs showing spectroscopic transmission on nanoantenna arrays X equal to 150 nm and 200 nm, made from both silver and composite. The size-dependent resonances observed show that Ag/ZnO composites can support a plasmon resonance like a true metal. Compared to pure silver the resonance is red shifted, which indicates a decrease in the real part of the permittivity, and broadened indicating an increase in loss. This is consistent with the material parameters found from ellipsometry.

Much like the thin films characterized earlier by ellipsometry, the nanoantennas displayed significant degradation after prolonged exposure to air. This effect was particularly pronounced for smaller antennas, which is to be expected since they have a smaller volume, thus making them more sensitive to surface changes. The effect of this degradation was seen as a slight red shift, and a strong reduction of resonance strength.

Chapter 6 - Multilayer structures

This chapter will focus on multilayer silver lenses operating at 365nm, and the experiments carried out to test their performance. The detection scheme uses a photoresist layer identical to that of the single layer superlens.

Multilayer superlenses have been shown theoretically to produce enhanced resolution compared to single layer lenses [20] [21], and are they can be designed for a specific wavelength by altering the thicknesses ratios between the metallic and dielectric layers [14] [15]. The design of multilayer lenses involves a lot of considerations with regards to the number of layers, the individual layer thickness, the total lens thickness and the order of layers [21].

Here we have chosen silicon dioxide for the dielectric layers, a choice that was made based on permittivity, availability and compatibility with the fabrication method. Germanium adhesion layers were used to reduce silver roughness [63].

Modeling

Comsol modeling to determine the optimal lens design was carried out by Zhengtong Liu at Purdue University. For the modeling a material system comprised of SiO₂, germanium and silver was used, and the results can be found in appendix B.

While the results show the highest contrast is achieved for 5 layers, it should be kept in mind that there is an inherent compromise with transmission, which decreases with the number of layers. Furthermore our experiment show that the roughness increases as the total lens thickness grows, which leads to a loss that is higher than theoretical predictions. For this reason lenses with 2 or 3 silver layers were chosen as the initial test subjects.

Multilayer fabrication

Since multiple layers are needed, and the thin silver layers are very prone to degradation in air, it proved necessary to find a fabrication method in which all the layers could be deposited at

once. This being the case, polymers could not be used as the dielectric layers. Silicon dioxide was chosen as a replacement, since it can be deposited in a PVD chamber along with the silver and germanium, and has suitable optical properties at the design wavelength of 365nm.

Electron-beam evaporation was chosen as the deposition method. This choice was mostly based on availability, since at the time there was only one chamber available with the necessary material combination. Later on sputtering was also used, which will be discussed in the next section.

The evaporation was carried out at a pressure of $2 \cdot 10^{-6}$ mbar, and the deposition rates were kept low to more accurately hit the desired thickness of each layer. For silver 2 \AA/s was used, for germanium it was 0.5 \AA/s , and for SiO_2 it was 1 \AA/s . These were all based on optimization performed for previous experiments (see appendix A).

The roughness measured for a lens with 2 silver layers (including 4 dielectric layers for a total thickness of 54nm) was very low at 0.4nm RMS, which is consistent with results achieved elsewhere [63]. For a lens with 3 silver layers (total of 9 layers and a thickness of 73nm) this increased slightly to 0.5nm RMS.

Planarization

In an effort to improve the planarization of the grating, a series of etch tests were carried out to more accurately match the depth with the deposited metal thickness. As a result of these tests, the peak to valley height was reduced from the 12nm used for previous single layer superlenses, to 3-5 nm for the multilayer lenses.

Further reduction proved unattainable, mainly due to variation in the etch rate, both across the sample and between samples. These variations arose as the result of fluctuation in the platen power at values below 50W, an inherent shortcoming of the available equipment.

Unlike the polymer planarization layers used earlier (see chapter 3), which conform to the surface contours, the SiO_2 layers were deposited by a highly directional method, which means they have very little planarizing effect. The SiO_2 layers have the same thickness all over the grating, thus resulting in an unchanged surface morphology. In an attempt to solve this

problem, tests were carried out using sputtering rather than electron-beam evaporation, since the inherent increase in chamber pressure should lead to a less directional deposition. However, the results show no significant improvement in the planarization for samples using sputtering.

While the height variation was known to be problematic, optical characterization of the lens was still carried out, since it could not be ruled out, that the lens might still function.

Optical characterization

In order to examine the optical properties of a multilayer lens, a number of test exposures were carried out. These exposures were performed in a similar way to the experiments using a single layer silver lens (see chapter 3), though the dosage had been adjusted to account for the difference in transmission between lens designs. The goal was to show that using a multilayer lens would result in improved resolution compared to the 80 nm achieved earlier, and to study the effect of using multiple layers on the image quality. If successful, the exposures should result in formation of a periodic pattern in the photoresist. After the exposure, AFM scans of the surface were performed, an example of which can be seen in figure 62.

Unfortunately the tests proved inconclusive, with no noticeable difference between the exposed and unexposed samples. This problem ultimately arises from insufficient planarization, since the grating structure has a peak-to-valley height around 5 nm, with variation in the order of a few nanometers. In the earlier single layer experiments, it was shown that the exposed resist may have a height variation as low as 1nm, which would be below the detection limit for these experiments.

In an effort to improve on this result, higher exposure doses were used (up to the full clearing dose), in the hope of increasing the thickness of the exposed photoresist pattern, but no such pattern could be detected.

At this time, it is unknown whether the height variations in the underlying grating rendered the lens non-functional, or if superlensing is taking place and simply cannot be distinguished due to the non-flat surface.

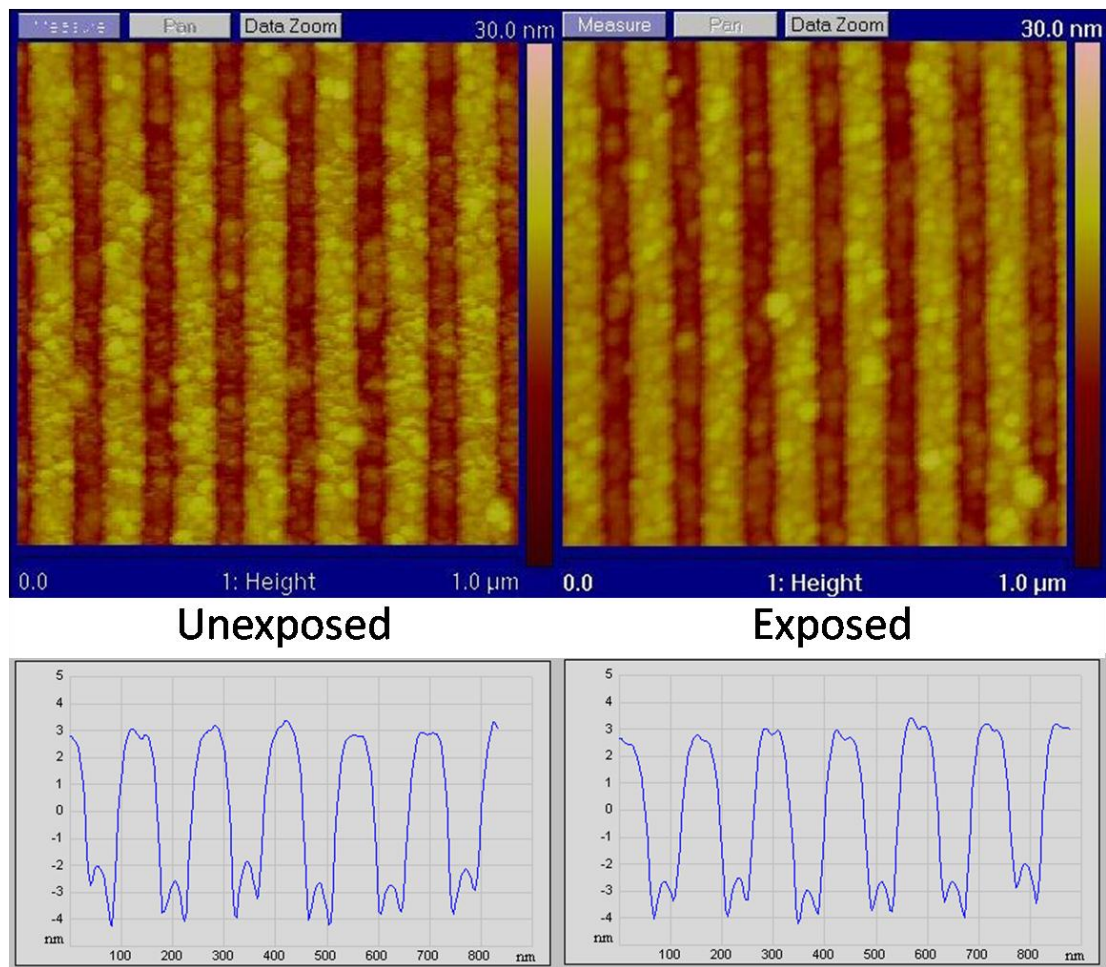


Figure 62. AFM scans before and after exposure for a 2 layer lens. No significant change can be observed.

A method for possibly solving this problem will be discussed in the outlook section of the conclusion.

Chapter 7 - Conclusion

Superlenses are a new class of optical components that rely on negative refraction and enhancement of evanescent fields to provide subwavelength imaging. This ability is of great interest in a range of applications, including ultraviolet lithography, surface enhanced Raman spectroscopy, enhanced fluorescence, focusing of light for sensors or solar cells and many more.

Here, it was shown that an 80 nm half pitch grating can be resolved using 365 nm light, which breaks the diffraction limit, and demonstrates the subwavelength imaging made possible by superlenses. However, optimization and tests on arbitrary objects still need to be carried out.

In order to further develop uses for superlensing in lab-on-a-chip devices, the use of a superlens to transfer an optical hotspot was tested. The results indicate a successful transfer, though complications with the presence of propagating modes on the periodic nanoantenna arrays, made it difficult to fully characterize the lens performance.

The advantage of using an integrated silver superlens, is that it provides all the benefits of surface enhanced spectroscopy, without the requirement of close vicinity between the sample molecules and metallic structures. Using a microfluidic device with an integrated thin film superlens and plasmonic nanoantennas, will enable field enhanced remote interaction with biomolecules, without disturbing the electrochemical environment of the suspended biomolecules. Therefore, lab-on-a-chip devices with such an integrated superlens, have a high potential impact on chip based protein detection, where the spatial separation of the biomolecules and nanoantennas, which is made possible through the use of a superlens, may prevent structural or functional changes of the biomolecules, such as the denaturation of proteins.

Furthermore, metal-dielectric composites were tested with regards to superlensing, since their adjustable permittivity opens up the possibility of creating a tunable superlens. MDC films were fabricated and characterized, with variations in material choices and composition, and their structural and the optical properties were characterized. The results show that the permittivity can be tuned within a wide range, and that the film roughness can be kept within acceptable limits. However, the optical losses far exceed the theoretical predictions, which highlights the need for a more comprehensive theory, and renders such films currently unsuitable for use in superlensing.

Finally, the performance of a multilayer lens was tested, with a negative photoresist as the detection method. However, complications arising from insufficient planarization made it impossible to verify whether or not the lens worked as intended.

Outlook

In order to conclusively prove, that a near-field transfer of the optical hotspots is indeed taking place, some additional experiments are needed. These experiments would start with eliminating the propagating mode, which could be done in a couple of ways: A non-periodic array could be used, or the periodicity could be changed to a value that differed greatly from the wavelength of the incident light. Once the propagating mode had been removed, it would be possible to study the localized resonance more closely, and characterize the superlens transfer function in detail. Furthermore, experiments are needed on a variety of lens configurations, including multilayered structures, in order to determine the optimum design. After establishing an optimized design for the lens configuration, it would then be possible to test its use in SERS or other applications.

Further testing is also needed for metal dielectric composites, since the experimental data thus far only covers two material combinations, and remains insufficient to make broad conclusion about the optical properties of MDCs. The goal should be developing a more accurate theoretical model, as well as establishing possible applications for the tunable permittivity, which would be enhanced tremendously, if a means of drastically lowering the loss could be found.

For the multilayer superlens experiments, a different test structure is needed, in order to enable the study of such lenses. Using RIE to embed the structures proved unfeasible, when the requirement is sub-nanometer planarization. A possible alternative might be found in a form of template stripping [65]. Here the grating could be fabricated on a sacrificial layer, surrounded by a dielectric medium, and then transferred to another substrate, in such a way that the flat bottom of the grating would become exposed, and serve as the new surface for a multilayer deposition.

The difficulty is realizing such a design, is finding a way to release the original substrate, without damaging the chrome grating or the dielectric medium. This is complicated by the need to maintain compatibility with electron-beam lithography, which means the sacrificial layer has to be insoluble in organic solvents.

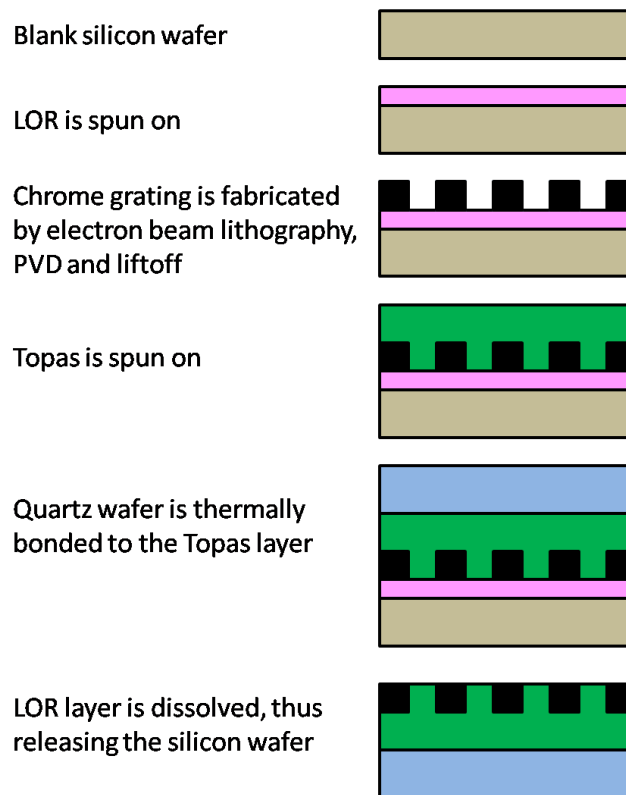


Figure 63. Proposed fabrication scheme for grating structure.

A possible material combination would consist of lift-off resist [66] for the sacrificial layer, and Topas for the dielectric medium. This would work by fabricating the gratings on the LOR layer, covering them with a Topas, thermally bonding a quartz wafer to the Topas layer, and then dissolving the LOR layer to release the grating from the original substrate. When completed, this would yield a flat surface, consisting of gratings imbedded in a Topas film. An illustration of this proposed fabrication scheme can be seen in figure 63

The main advantage of such a fabrication scheme is that the chrome grating and its surrounding medium would be perfectly planarized, since the bottom facet is used, and it conforms to the underlying LOR layer. The surface roughness would be given by the LOR layer.

Bibliography

- [1] W. Cai and Vladimir Shalaev, *Optical Metamaterials: Fundamentals and Applications.*: Springer, 2009.
- [2] Victor Veselago, "The electrodynamics of substances with simultaneously negative values of ϵ and μ ," *Sov. Phys. Usp.*, vol. 10, no. 4, pp. 509-514, 1968.
- [3] J. B. Pendry, "Negative Refraction Makes a Perfect Lens," *PHYSICAL REVIEW LETTERS*, vol. 85, no. 18, pp. 3966–3969, 2000.
- [4] Nicholas Fang, Hyesog Lee, Cheng Sun, and Xiang Zhang, "Sub-Diffraction-Limited Optical Imaging with a Silver Superlens," *Science*, vol. 308, no. 5721, pp. 534-537 , 2005.
- [5] David O. S. Melville and Richard J. Blaikie, "Super-resolution imaging through a planar silver layer," *OPTICS EXPRESS*, vol. 13, no. 2127, pp. 2127-2134 , 2005.
- [6] D.R. Smith, D. Schurig, Marshall Rosenbluth, S. Schultz, S. Anantha Ramakrishna, J. B. Pendry, "Limitations on Sub-Diffraction Imaging with a Negative Refractive Index Slab," *Appl. Phys. Lett.*, vol. 82, no. 10, pp. 1506 - 1508, 2003.
- [7] Viktor A. Podolskiy and Evgenii E. Narimanov, "Near-sighted superlens," *OPTICS LETTERS*, vol. 30, no. 1, pp. 75-77, 2005.
- [8] Zhaowei Liu, Hyesog Lee, Yi Xiong, Cheng Sun, and Xiang Zhang, "Far-Field Optical Hyperlens Magnifying Sub-Diffraction-Limited Objects," *Science*, vol. 315, no. 5819, p. 1686 , 2007.
- [9] Zhaowei Liu, Stéphane Durant, Hyesog Lee, Yuri Pikus, Nicholas Fang, Yi Xiong, Cheng Sun, Xiang Zhang, "Far-Field Optical Superlens," *Nano Letters*, vol. 7, no. 403, pp. 403–408, 2007.
- [10] Zhengtong Liu, Mark D. Thoreson, Alexander V. Kildishev, and Vladimir M. Shalaev,

- "Translation of nanoantenna hot spots by a metal-dielectric composite superlens," *APPLIED PHYSICS LETTERS*, vol. 95, no. 3, p. 033114, 2009.
- [11] K. Kneipp, M. Moskovits, and H. Kneipp, *Surface-Enhanced Raman Scattering*. Berlin: Springer, 2006.
- [12] Alexander V. Kildishev and Vladimir M. Shalaev, "Engineering space for light via transformation optics," *OPTICS LETTERS*, vol. 33, no. 1, pp. 43-45, 2008.
- [13] Wenshan Cai, Dencho A. Genov, and Vladimir Shalaev, "Superlens based on metal-dielectric composites," *PHYSICAL REVIEW B*, vol. 72, no. 19, p. 193101, 2005.
- [14] Pavel A. Belov and Yang Hao, "Subwavelength imaging at optical frequencies using a transmission device formed by a periodic layered metal-dielectric structure operating in the canalization regime," *PHYSICAL REVIEW B*, vol. 73, no. 11, p. 113110, 2006.
- [15] I. I. Smolyaninov, Y.-J. Hung, and C.C. Davis, "Magnifying superlens in the visible frequency range," *Science*, vol. 315, no. 5819, pp. 1699-1701, 2007.
- [16] Pratik Chaturvedi, Wei Wu, Vijay Logeeswaran, Zhaoning Yu, Yu Xiong, Saif Islam, Shih-yuan Wang, Xiang Zhang, Nicholas Fang, "Molecular Scale Imaging with a Smooth Superlens," in *Photonic Metamaterials: From Random to Periodic, OSA Technical Digest*, 2007.
- [17] Thomas Taubner, Dimitriy Korobkin, Yaroslav Urzhomov, Gennady Shvets, and Rainer Hillenbrand, "Near-Field Microscopy Through a SiC Superlens," *Science*, vol. 313, no. 5793, p. 1595, 2006.
- [18] E. Plum, J. Zhou, J. Dong, V. A. Fedotov, T. Koschny, C. M. Soukulus, N. I. Zheludev, "Metamaterial with negative index due to chirality," *PHYSICAL REVIEW B*, vol. 79, no. 3, p. 035407, 2009.
- [19] Shumin Xiao, Vladimir P. Drachev, Alexander V. Kildishev, Xingjie Ni, Uday K. Chettiar, Hsiao-Kuan Yuan, Vladimir M. Shalaev, "Loss-free and active optical negative-index

- metamaterials," *Nature letters*, vol. 466, pp. 735–738, 2010.
- [20] E. Shamonina, V. A. Kalinin, K. H. Ringhofer, and L. Solymar, "Imaging, compression and Poynting vector streamlines for negative permittivity materials," *ELECTRONICS LETTERS*, vol. 37, no. 20, pp. 1243 - 1244 , 2001.
- [21] David O.S. Melville and Richard J. Blaikie, "Analysis and optimization of multilayer silver superlenses for near-field optical lithography," *Physica B*, vol. 394, no. 2, pp. 197-202, 2007.
- [22] Max Born and Emil Wolf, *Principles of Optics*.: Cambridge University Press, 1997.
- [23] Stefan Maier, *Plasmonics: Fundamentals and Applications*.: Springer, 2007.
- [24] H. Raether, *Surface plasmons*.: Springer, 1988.
- [25] http://en.wikipedia.org/wiki/Snell's_law.
- [26] Laszlo Solymar and Ekatarina Shamonina, *Waves in Metamaterials*.: Oxford, 2009.
- [27] F. D. M. Haldane, *Electromagnetic surface modes at interfaces with negative refractive index make a 'not-quite-perfect' lens*.: arXiv:cond-mat/0206420v3, 2002.
- [28] Mikkel Schøler and Richard J. Blaikie, "Simulations of surface roughness effects in planar superlenses," *J. Opt. A*, vol. 11, no. 10, p. 105503, 2009.
- [29] K.-H. Su, Q.-H. Wei, and X. Zhang, "Interparticle Coupling Effects on Plasmon Resonances of Nanogold Particles," *NANO LETTERS*, vol. 3, no. 8, pp. 1087-1090, 2003.
- [30] W. Rechberger, A. Hohenau, A. Leitner, J.R. Krenn, B. Lamprecht, F. R. Aussenegg, "Optical properties of two interacting gold nanoparticles," *Optics Communications*, vol. 220, pp. 137-141, 2003.

- [31] Tuck Choy, *Effective Medium Theory*.: Oxford, 1999.
- [32] G. A. Niklasson, C. G. Granqvist, and O. Hunderi, "Effective medium models for the optical properties of inhomogeneous materials," *APPLIED OPTICS*, vol. 20, no. 1, pp. 26-30, 1981.
- [33] J. C. M. Garnett, "Colours in metal glasses and in metal films," *Philos. Trans. R. Soc. London*, vol. 203, pp. 385-420, 1904.
- [34] D. A. G. Bruggeman, "Berechnung Verschiedener Physikalischer Konstanten von Heterogenen Substanzen," *Ann. Phys. Leipzig*, vol. 24, no. 7, pp. 636-664, 1935.
- [35] Richard C. Jaeger, *Lithography*.: Prentice Hall, 2002.
- [36] M. A. McCord and M. J. Rooks, "Handbook of Microlithography, Micromachining and Microfabrication," 2000.
- [37] *Plasma etching and reactive ion etching*.: American Institute of Physics, 1982.
- [38] John E. Mahan, *Physical Vapor Deposition of Thin Films*.: John Wiley , 2000.
- [39] Richard C. Jaeger, *Film Deposition*.: Upper Saddle River: Prentice Hall, 2002.
- [40] William D. Westwood, *Sputter Deposition*.: AVS Education Committee Book Series, 2003.
- [41] S. Wolf and R. N. Tauber, *Silicon Processing for the VLSI Era Vol. 1*.: Lattice Press, 1999.
- [42] Franz J. Giessibl, "Advances in atomic force microscopy," *Reviews of Modern Physics*, vol. 75, no. 3, pp. 949-983, 2003.
- [43] Joseph Goldstein, Dale E. Newbury, David C. Joy, Charles E. Lyman, Patrick Echlin, Eric Lifshin, Linda Sawyer, J. R. Michael, *Scanning Electron Microscopy and X-ray Microanalysis*.: Springer, 2003.
- [44] H. G. Tompkins and W. A. McGahan, *Spectroscopic Ellipsometry and Reflectometry*.: John

Wiley & Sons Inc , 1999.

- [45] <http://www.olympusmicro.com/primer/techniques/nearfield/nearfieldintro.html>.
- [46] Edwin Oosterbroek and A. van den Berg, *Lab-on-a-Chip: Miniaturized systems for (bio)chemical analysis and synthesis.*: Elsevier Science, 2003.
- [47] H. Lee, Y. Xiong, N. Fang, W. Srituravanich, S. Durant, M. Ambati, C. Sun, X. Zhang, "Realization of optical superlens imaging below the diffraction limit," *New J. Phys.*, vol. 7, p. 255, 2005.
- [48] R. R. Lamonte and D. McNally, "Uses and processing of cyclic olefin copolymers," *Plast. Eng.*, vol. 56, no. 6, pp. 51-55, 2000.
- [49] www.topas.com.
- [50] Zhengtong Liu, Alexandra Boltasseva, Rasmus H. Pedersen, Reuben Bakker, Alexander V. Kildishev, Vladimir P. Drachev, Vladimir M. Shalaev, "Plasmonic nanoantenna arrays for the visible," *Metamaterials*, vol. 2, no. 1, pp. 45-51, 2008.
- [51] R. Holt and T. Cotton, "Surface-enhanced resonance Raman and electrochemical investigation of Glucose oxidase catalysis at a silver electrode," *J. Am. Chem. Soc.*, vol. 111, pp. 2815–2821, 1989.
- [52] M. Yang, M. Chung, and F. Thompson, "Acoustic network analysis as a novel technique for studying protein adsorption and denaturation at surfaces," *Anal. Chem.*, vol. 65, no. 24, pp. 3713–3716, 1993.
- [53] Pascal Anger, Palash Bharadwaj, and Lukas Novotny, "Enhancement and Quenching of Single-Molecule Fluorescence," *Phys. Rev. Lett.*, vol. 96, no. 11, p. 113002, 2006.
- [54] <http://www.ioffe.ru/SVA/NSM/nk/GermaniumCompounds/Gif/ge.gif>.

- [55] Thomas W. Ebbesen, Cyriaque Genet, and Sergey I. Bozhevolnyi, "Surface-plasmon circuitry," *Physics Today*, vol. 61, no. 5, pp. 44-50, 2008.
- [56] Olivier Parriaux, Vladimir A. Sychugov, and Alexander V. Tishchenko, "Coupling gratings as waveguide functional elements," *Pure Appl. Opt.*, vol. 5, no. 4, pp. 453–469, 1996.
- [57] Lihong Shi, Lei Gao, Sailing He, and Baowen Li, "Superlens from metal-dielectric composites of nonspherical particles," *PHYSICAL REVIEW B*, vol. 76, no. 4, p. 045116, 2007.
- [58] R. B. Nielsen, M. D. Thoreson, W. Chen, A. Kristensen, J. M. Hvam, V. M. Shalaev, A. Boltasseva, "Toward Superlensing with Metal-Dielectric Composites and Multilayers," *Applied Physics B*, vol. 100, no. 1, pp. 93-100, 2010.
- [59] Bo Chen, Dongfang Yang, and Chii-Wann Lin, "Surface plasmon resonance response of Au–WO₃–x composite films," *Applied Physics A*, vol. 97, no. 2, pp. 489-496, 2009.
- [60] S. Esposito, A. Antonaia, M. L. Addonizio, and S. Aprea, "Fabrication and optimisation of highly efficient cermet-based spectrally selective coatings for high operating temperature," *Thin Solid Films*, vol. 517, no. 21, pp. 6000-6006, 2009.
- [61] C. Klingshirn, "ZnO: Material, Physics and Applications," *ChemPhysChem*, vol. 8, no. 6, pp. 782-803, 2007.
- [62] Charles T. Campbell, "Ultrathin metal films and particles on oxide surfaces: structural, electronic and chemisorptive properties," *Surface Science Reports*, vol. 27, no. 1, pp. 3-111, 1997.
- [63] Weiqiang Chen, Mark D. Thoreson, Satoshi Ishii, Alexander V. Kildishev, and Vladimir M. Shalaev, "Ultra-thin ultra-smooth and low-loss silver films on a germanium wetting layer," *OPTICS EXPRESS*, vol. 18, no. 5, pp. 5124-5134, 2010.
- [64] W. Chen, M. D. Thoreson, A. V. Kildishev, and V. M. Shalaev, "Fabrication and optical characterizations of smooth silver-silica nanocomposite films," *Laser Phys. Lett.*, vol. 7, no.

9, pp. 677-684, 2010.

- [65] L. Todd Banner, Andrew Richter, and Eugene Pinkhassik, "Pinhole-free large-grained atomically smooth Au(111) substrates prepared by flame-annealed template stripping," *Surf. Interface Anal.*, vol. 41, no. 1, pp. 49-55, 2009.
- [66] <http://www.microchem.com/products/pmgi.htm>.

Appendix A: Fabrication schemes

Ultraviolet superlens

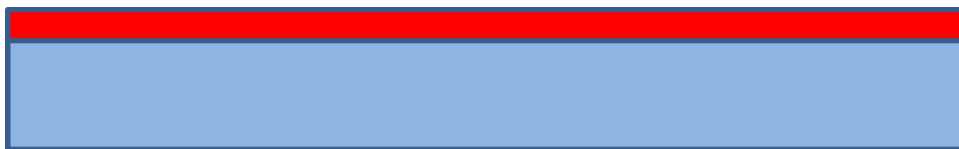
This section will describe the method developed for making a near-field silver superlens, and the test substrate needed to validate its performance. It will serve as the basis not only for experiments using a simple silver superlens, but also for the later attempts at using superlenses based on multilayer structures or metal dielectric composites. This describes only the final fabrication scheme, and the reasons for each of the steps listed.

Step 1: 4-inch Fused Silica substrate



A 4-inch fused silica substrate is used as the starting point for a couple of reasons. Firstly, a substrate with good transparency in the ultraviolet range is needed for the later exposure through the substrate (step 19). Secondly most of the equipment in the Danchip cleanroom is designed for 4-inch substrates. And finally cheaper glass substrate are not compatible with RIE (step 7), because they contain trace elements of substances that are not allowed in the chamber in order to avoid possible cross contamination.

Step 2: Spin on ZEP 520A



The positive electron-beam resist ZEP 520A was chosen, because it has excellent contrast and high sensitivity, which cuts down write time for electron-beam lithography. Furthermore, it has much better dry-etch resistance than other positive resists, like PMMA, which is needed, when it is used as an RIE etch mask (step 7).

The resist is delivered at a standard concentration of 11% in Anisole. This is diluted 1:2 in Anisole to achieve a 3.7% volume concentration, which results in a thinner resist layer after being spun on.

Process parameters are:

500 rpm pre-spin with a 100 rpm/s acceleration for 10 seconds

2000 rpm spin with a 1500 rpm/s acceleration for 30 seconds

180°C bake on a hotplate for 5 minutes

The pre-spin is needed in order to ensure complete coverage of the wafer. This is particularly important for ZEP 520A on quartz because the adhesion is poor, and failure to do a pre-spin will result in large areas of the wafer uncovered by any resist. For the same reason, it is important to cover most of the wafer with resist prior to the pre-spin. A total volume of around 2 ml is needed to achieve adequate coverage of a 4-inch wafer.

Spinning the wafer at 2000 rpm results in a uniform resist thickness of around 105 nm.

The hotplate was covered by aluminum foil prior to baking the wafer, in an attempt to avoid any contamination from the hotplate onto the wafer.

After baking, the wafers were inspected for possible defects, and re-processed if the result was not satisfactory. Backside particles are particularly problematic, since they can result in wafer bowing when clamped to the electron-beam chuck, and will result in height differences across the wafer, thus causing pattern distortion due to the very short focal length of the electron-beam.

Step 3: Deposit thermal aluminum



Since fused silica is non-conductive, it is necessary to deposit a conductive layer on top of the electron-beam resist, in order to avoid charging during exposure. A thin aluminum layer was chosen for its high conductivity, compatibility with subsequent fabrication steps and ease of removal. Deposition was done in the Wordentec chamber, using thermal evaporation, to a thickness of 20 nm. This represents a good tradeoff between conductivity requirements, and the need to allow electrons to pass through unaffected.

For optimal results an aluminum heat sink was placed on the backside of the wafer to reduce the temperature during deposition, and a waiting period of 10 min was used between depositions and venting, in order to avoid excessive oxidization of the still hot aluminum layer.

Step 4: Electron-Beam Lithography



The electron-beam lithography was performed at 100 kV, with a 4 nm beam spot and a current of 0.63 nA. Aperture 6 (50 μ m) was used, since it provides a good compromise between current and focal depth.

In order to accurately write the fine details of the grating pattern, proximity-correction software was used. The large alignment marks do not need correction, and were placed in a separate file.

Step 5: Etch Aluminum

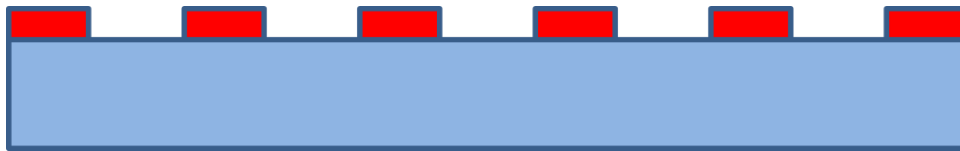


After electron-beam lithography the aluminum layer is no longer needed, and is removed by a wet etch using MF-322, which takes place in a Petri dish with manual agitation. Typical etch

time is around 45 seconds, and is easily verifiable by simply observing the process, but may increase to as high as 90 seconds, if the aluminum layer is exposed to air for a prolonged period of time.

Once the etch process is completed, the water based MF-322 is removed by rinsing with DI water for 30 seconds in another Petri dish. The DI water gun should not be used at this point, since it can cause the ZEP to peel off from the substrate. Finally the wafer was dried using a nitrogen gun.

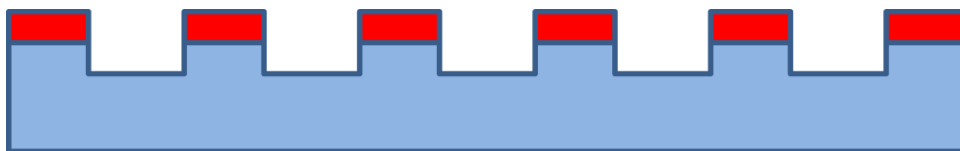
Step 6: Develop ZEP 520A



The resist was developed by using N-50 in a Petri dish, for a period of 120 seconds with manual agitation. Afterwards the N-50 is rinsed off by IPA immersion, and the wafer is dried using a nitrogen gun.

Following development a microscope inspection of the wafer was performed, in order to verify that the results were adequate before proceeding. Furthermore AFM inspection was used to get more detailed information about the results.

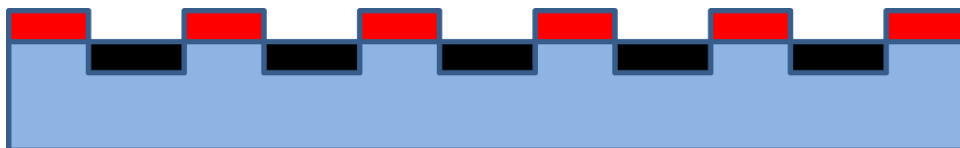
Step 7: Reactive-Ion Etch



In order to embed the chrome grating it is necessary to etch holes in the silica substrate prior to metal deposition. For this purpose an anisotropic RIE process was chosen. The process is based on a mixture of CF_4 and CHF_3 gasses in order to etch silica effectively, while at the same time

maintaining acceptable etch selectivity. For silica versus ZEP the etch selectivity is roughly 2:1. The etch parameters were: 42 sccm CHF_3 , 24sccm CF_4 , with a power of 24W, and a chamber pressure of 16mTorr for 270 seconds. Prior to beginning the etch itself, a brief O_2 etch was used to ensure that no residual polymer layer remains in the mask openings.

Step 8: Deposit chrome



Chrome was chosen as the masking material for its excellent adhesion to silica, low skin depth and very low roughness. Deposition was done by electron-beam evaporation, either in the Wordentec or the Alcatel. The deposition rate was relatively high at $10\text{\AA}/\text{s}$, in order to minimize the resist heating due to thermal radiation from the source. This is especially critical, since the silica substrate conducts heat very poorly, and overheating of the resist can occur.

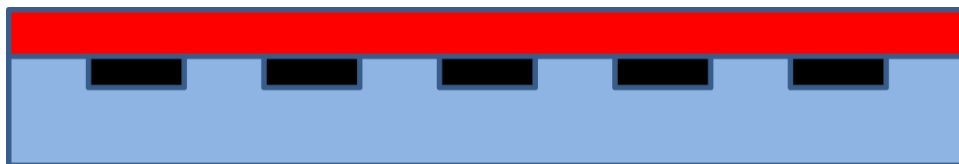
Step 9: Lift-off #1



The lift-off of chrome was performed in Remover 1165 (1-methyl-2-pyrrolidinone), which works well with ZEP 520A. Since chrome has excellent adhesion to silica, it is possible to use high intensity ultrasound for the lift-off, which helps decrease the duration significantly. The lift-off was carried out in a Petri dish, which had been placed in an ultrasonic bath, and the duration was 1 hour. The use of ultrasound causes gradual heating of the solvent, typically rising from around 20°C to 55°C over the duration. This helps speed up the process, and poses no risks since the boiling of Remover 1165 point is around 200°C .

After lift-off, the substrate was cleaned by immersion in acetone followed by an IPA rinse. Finally, the substrate was dried with a nitrogen gun.

Step 10: Spin on AZ5214E



The photoresist chosen for the UV lithography step was AZ5214E, which was spun on with the following parameters:

4500 rpm for 30 seconds

60 seconds bake on a hotplate at 90°C

Prior to spinning on the resist, the wafers underwent a surface treatment with hexamethyldisilazane (HMDS), in order to improve adhesion, which can otherwise be very poor on fused silica substrates.

Step 11: Ultraviolet Lithography



The UV exposure was performed in a Karl Süss MA6 mask aligner, using the included alignment marks from the EBL grating pattern, and an exposure dose of 70 uC/cm^2 at a wavelength of 365nm (I-line). Hard contact mode was used for maximum pattern fidelity.

Step 12: Develop AZ5214E



The AZ5214E was developed in one of the dedicated wet benches using a 1:5 solution of AZ351B. Manual agitation was used, since no mechanical means are available, and the process time was 70 seconds. After immersion in the developer, the substrate was cleaned in DI water with a nitrogen flow for agitation, and then spin dried in a nitrogen oven.

Step 13: Deposit aluminum



A 40 nm aluminum layer was deposited in order to shield the resist from stray light in subsequent UV lithography steps (step 19). Aluminum was chosen for its compatibility with reactive ion etching (step 16).

The quality of the aluminum layer in this step is not especially crucial, so no particular deposition chamber or method is required. As a result the method used depended mostly on which process chamber was available at the time.

Step 14: Lift-off #2



Lift-off of aluminum was done in an acetone bath with ultrasonic agitation, which was followed by a water rinse, and a spin dry in a nitrogen chamber. Since the areas without aluminum are very small (20x20 μm) they are not immediately visible, so lift-off results have to be confirmed with an optical microscope.

Step 15: Spin on Topas



For the spacing layer the polymer Topas (Cyclic Olefin Copolymer) was chosen. It was chosen for its low roughness, low loss for UV light, and compatibility with subsequent UV lithography steps (step 18 and 19).

The two components of the copolymer have different polarity, which causes it to form micelles in solution, and results in higher roughness after spinning. To avoid this problem it is critical to use ultrasound on the resist for several hours immediately prior to use, which helps break up the micelles.

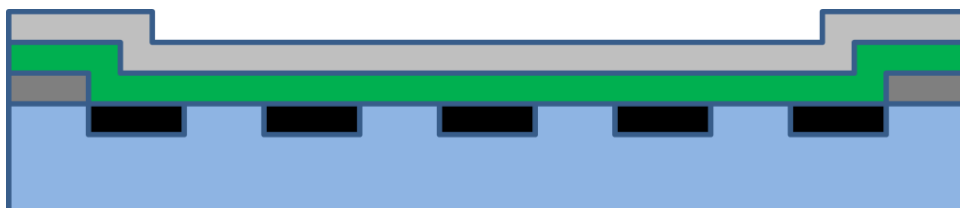
Step 16: Etch down Topas



The Topas layer was etched down to a thickness of 40nm a series of RIE steps, with ellipsometry measurements in between to determine the exact thickness.

In addition to the RIE the substrate was treated with a brief etch in a plasma asher each time, which was done because the isotropic nature of the etch works to reduce roughness by etching protrusions faster than bulk material.

Step 17: Deposit silver



Silver was deposited by electron-beam evaporation in the Alcatel chamber. This particular chamber was chosen, because it has a crystal monitor, which is placed in front of the shutter, which means the deposition rate can be measured before deposition on the wafer begins.

An exact etch rate of 1.5 \AA/s was used in order to lower the roughness, and the silver was changed prior to each deposition.

Step 18: Spin on Negative resist



The negative resist mr-UVL 6000 from micro resist technology GmbH was chosen due to its low design thickness, high resolution and compatibility with our process. It was spun on using the following parameters:

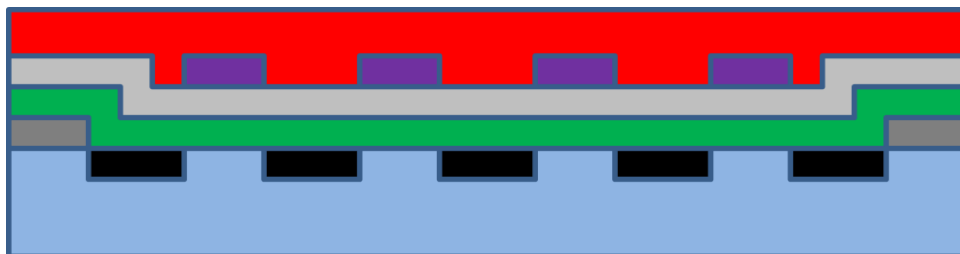
500 rpm pre-spin with a 100 rpm/s acceleration for 10 seconds

5000 rpm with an acceleration of 1500 rpm/s for 30 seconds

110°C bake on a hotplate for 3 minutes

The resulting photoresist layer is only 70nm thick, which is more than adequate for our purposes, and helps to prevent any possible waveguiding effect in the resist layer.

Step 19: UV exposure

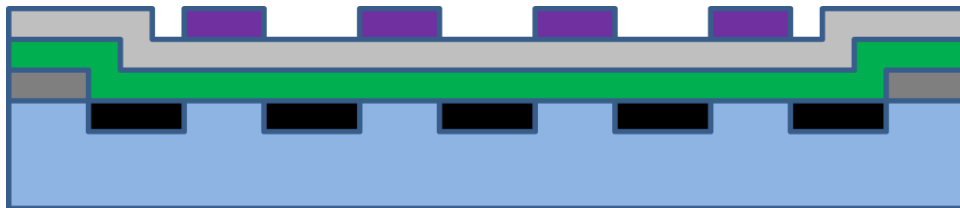


The resist was exposed through the superlens, in order to determine if the subwavelength features of the grating could be reproduced. To do this, the wafer was placed upside down in the aligner and flood exposed. A chuck with an open center was used to avoid any abrasive damage to the resist layer.

The exposure dose of 750 uC/cm^2 is not the normal full exposure dose, instead it is the dose that corresponds to 50% residual height. This was done because the contrast is highest at this dose, which helps create a more accurate depiction of the intensity profile in the resist.

After UV exposure, the resist was baked at 110°C on a hotplate for 3 minutes.

Step 20: Develop negative resist



The mr-UVL 6000 was developed in two steps, first a 1-minute submersion in Propylene Glycol Methyl Ether Acetate (PGMEA) to remove the majority of the unexposed resist, then a second 1-minute fine rinse also in PGMEA, but in a different tank. Stirring of the solvent was provided by built-in mechanical agitation. Afterwards, the substrate was rinsed in IPA and dried with a nitrogen gun.

Near-field transfer of optical hotspot

Some of the steps are identical to those used in the initial superlens fabrication scheme, so rather than describing them yet again, a reference will be made to the previous description.

Step 1: 4 inch Fused Silica substrate



See superlens fabrication scheme step 1.

Step 2: Spin on ZEP 520A



See superlens fabrication scheme step 2.

Step 3: Deposit thermal aluminum



See superlens fabrication scheme step 3.

Step 4: Electron-Beam Lithography



For the nanoantennas no proximity correction is needed since the area coverage is relatively low at 6.7%, and the array is much larger than the backscattering distance, which means the background dose is fairly uniform across the array. A relatively high current of 1.38nA was used in order to reduce the write time, which would otherwise be extensive given the size and number of arrays needed. A voltage of 100kV was used, with a grid size of 4nm, and aperture 6.

Two different exposure doses of 300 and 350 $\mu\text{C}/\text{cm}^2$ were used. The difference in dose creates a slight difference in the size of the antennas pattern created, which shifts the resonance frequency.

Step 5: Dice wafer



Wafers were diced prior to developing, with the aluminum layer still on. This was done because experiments with dicing after developing found that the resist pattern suffered significant damage during dicing. The damage occurred because the polymer tended to stick to other surfaces it came into contact with, and would peel off in flakes when separated. The aluminum on the other hand does not stick, and also serves as a protective layer against contamination during the dicing process, which takes places outside the cleanroom.

The need to dice the wafers before developing poses some challenges to alignment, since no patterns are visible yet. As a result the location of each cut had to be aligned to the edge of the wafer, and rotational alignment was done using the major flat as a reference.

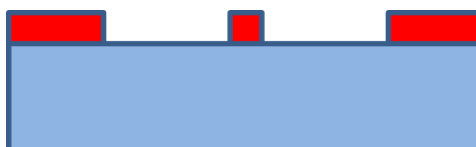
After dicing the wafers were initially cleaned with DI water and air dried. Then they were brought into the cleanroom for a second cleaning step, which was done using IPA and a nitrogen gun.

Step 6: Etch aluminum



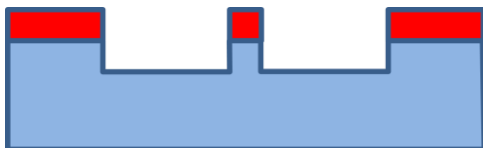
See superlens fabrication scheme step 5.

Step 7: Develop



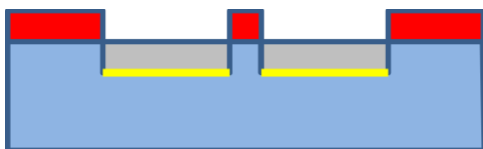
See superlens fabrication scheme step 6.

Step 8: Reactive Ion Etch



The RIE process used was identical to that developed for the initial superlens experiments (see superlens fabrication scheme step 7) except for the duration, which was altered to 3m30s due to the change in etch depth.

Step 9: Deposit Ge+Ag



The nanoantennas used consist of silver with a germanium adhesion layer. This particular combination of materials was only available in the III-V dielectric evaporator, so all depositions were carried out in this chamber.

For the germanium deposition an extremely low deposition rate had to be used, in order to accurately deposit a layer thickness of just 1.5nm. The rate chosen was 0.5Å/s, which was lowest stable rate that could be achieved. The thickness of 1.5nm was based on the need to use ultrasound in the lift-off (see step 10), while at the same time introducing as little optical loss as possible. Lower adhesion layer thicknesses did not provide sufficient adhesion to prevent antennas from peeling off.

The silver layer deposition was carried out at a relatively high rate of 10Å/s. This proved necessary because the heat conductance away from the samples is very limited in this chamber, and using lower depositions rates tended to cause overheating from extended exposure to the radiated heat from the source.

Step 10: Lift-off



Lift-off was carried out in two distinct steps: First a 10 minute rough strip using acetone and ultrasound, then a 1 hour fine strip using Remover 1165. After each step the wafers were cleaned with IPA and dried with a nitrogen gun. The rough rinse serves to remove all excessive silver, and the subsequent rinse prevents any re-deposition of silver during the lift-off. The fine rinse removes all remaining resist.

Prolonged periods of immersion in Remover 1165, or the use of ultrasound in Remover 1165, were found to cause some problems with adhesion between the antennas and the substrate, which forced the use of this two-step lift-off process.

Step 11: Deposit $\text{SiO}_2 + \text{Ge} + \text{Ag} + \text{SiO}_2$



The deposition of the silicon dioxide spacer/cover layers, the germanium adhesion layer and the silver superlens layer, were all carried out in a single step using the III-V dielectric evaporator. The silicon dioxide was deposited with a low deposition rate of $1\text{\AA}/\text{s}$. After each deposition a fresh supply of silicon dioxide pellets were placed in the crucible, since the source material was found to change properties after prolonged use, and a high level of consistency was desired.

Germanium was deposited with the same parameters used earlier, though the thickness was reduced to 1nm. This was done to lower optical loss, and could be used since the samples would not undergo any further ultrasonic steps.

Silver was deposited at 2 \AA/s , which was found to slightly lower the roughness, and since no polymer is present at this point, heating of the sample was not a concern.

In addition to the ordinary samples with a superlens coating, some reference samples with an equivalent thickness SiO_2 coating were also made. For these a single 63nm silicon dioxide layer was deposited, with the same deposition parameters used previously.

Step 12: Spin on PMMA



After finishing the fabrication, each sample is coated with a PMMA film, which helps protect against environmental damage. This proved necessary because weeks or even months can pass between fabrication and characterization, and the silver layer would be hopelessly degraded if exposed to air for such a length of time.

The film was made using a 5% solution of 950k PMMA in acetone, which was spun on at 1000 rpm, and baked on a hotplate at 180°C . The resulting film thickness is estimated at around 600nm.

Once the samples are about to undergo characterization, the PMMA layer can be easily removed using acetone.

Appendix B: Comsol modeling

365 nm design

Germanium layers were kept at a constant thickness of 1nm, due to previous fabrication experience.

A minimum thickness of 8nm was used for the silver layers, since this corresponds to threshold at which continuous films are formed when using a germanium adhesion layer [63]. This also proved to be the optimal thickness, with thinner layers showing improved performance theoretically, but discarded for their infeasibility from a fabrication standpoint. Thus the silver thickness was kept at a constant 8nm for all further simulations.

With these limitations in mind the tunable parameters were the number of layers, the thickness of individual silicon dioxide layers, and the thickness of the grating.

The contrast 20nm above the superlens surface was chosen as the optimization parameter, since it is a good measure for the performance of the lens.

The modeling used the same material parameters as the earlier single layer superlens results, and a permittivity for germanium of $9.9 + 21i$.

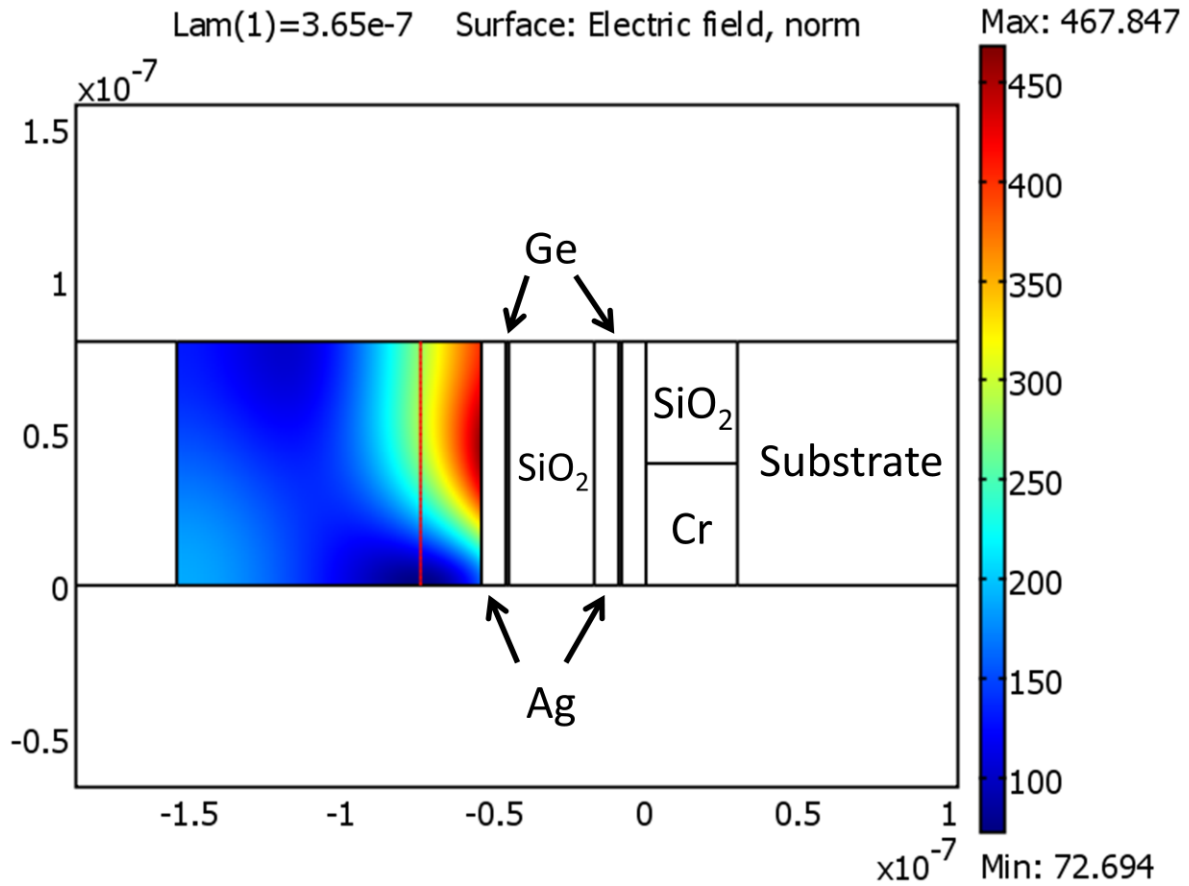


Figure 64. Comsol modeling of a 2 layer superlens structure. The model shows a single unit cell consisting of one 80nm grating period.

From the modeling results, an ideal design was establish for 1-5 layers, the results of which can be seen in table 3

Table 3. Summary of the results from comsol modeling of multilayer lenses with 1-5 layers.

Layers	Duty	Grating (nm)	Spacer (nm)	Host (nm)	Contrast	Contrast w/o Ag	T
1	0.5	30	24	N/A	7.1	2.0	9%
2	0.5	30	8	28	4	1.2	7%

3	0.5	30	30	8	2.5	1.01	4%
4	0.5	60	21	25	3.1	1.04	4%
5	0.5	60	21	22	8	1.01	2.6%

633 nm design

Interference effects from the periodic grating cause the image to be reversed, with the highest intensity regions directly behind the chrome grating.

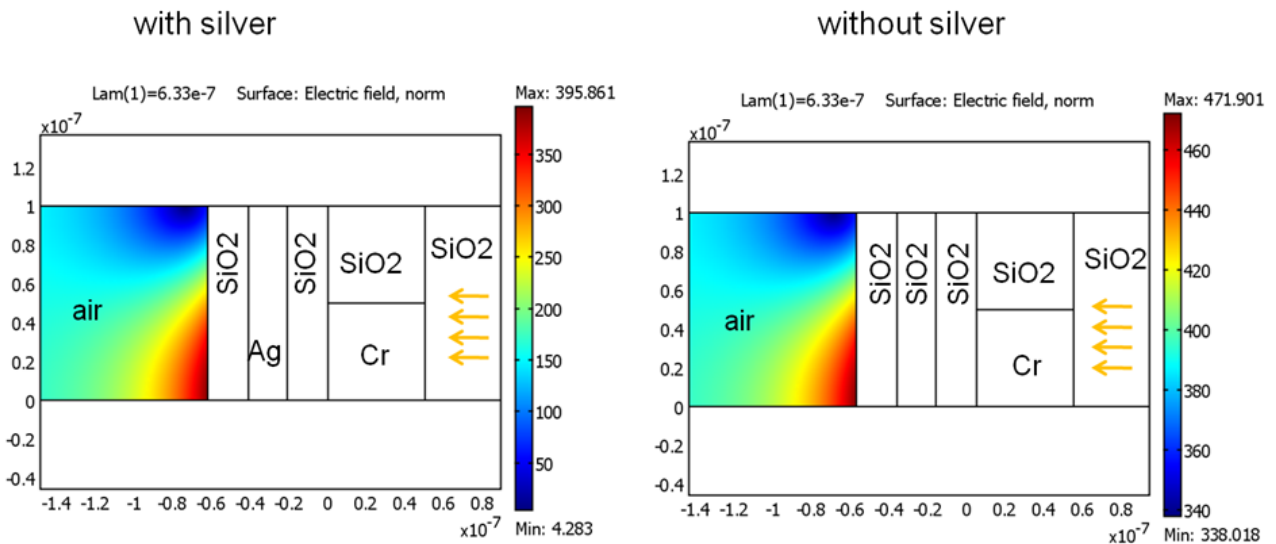


Figure 65. Comsol modeling of the field distribution with (left) and without (right) a superlens layer. As expected the lossy silver causes a drop in average intensity, but it also has the effect of greatly increasing the contrast.

The simulated results are very similar to those of a silver lens operating at 365 nm, with the silver lens demonstrating superior contrast compared to an equivalent thickness dielectric layer, though it comes at the cost of a reduced average intensity.

A summary of the simulation results can be seen in table 4

Table 4. Table showing the simulation results for multilayer lenses at 633nm. The grating layer, spacer/cover layers and host layer thicknesses have all been tuned to achieve the optimal contrast for each number of layers.

Layers	Grating (nm)	Spacer /cover (nm)	Host (nm)	Contrast	Contrast w/o Ag	Transmission
1	50	21	N/A	43	1.25	7.50%
2	37	25	40	52	1.02	0.92%
3	37	27	42	278	1.01	0.09%
4	60	26	44	55	1	0.01%
5	43	30	43	32	1	0.00%

Appendix C: SNOM setups

Erlangen University setup

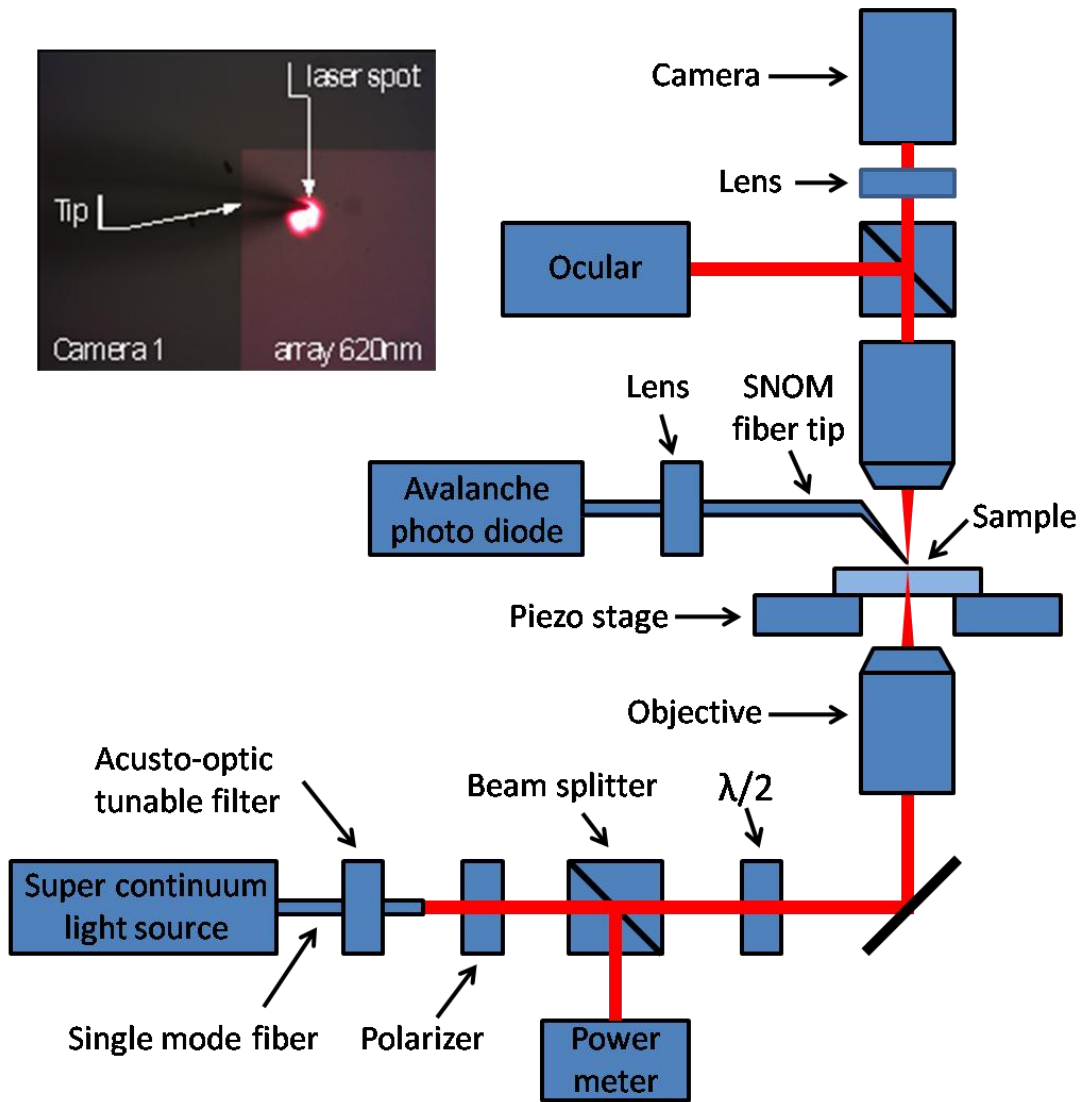


Figure 66. Schematic of the SNOM setup used at Erlangen University

Procedure

- A single wavelength is selected from the supercontinuum with an acusto-optic tunable filter (range from 450 to 700 nm).
- The beam is coupled into a single mode fiber.
- The beam is coupled out and collimated, then sent through a polarizer.

- A non-polarizing beam splitter allows for referencing the probe power and for observing the back-reflected beam for an exact adjustment.
- The probe polarization is adjusted with a broadband visible half wave plate.
- The beam is focussed on the sample with an objective. For these measurements a 4x magnification Olympus objective with a numerical aperture of 0.1 was used.
- The sample is placed on a xyz piezo stage, and accessed from the top with a multimode SNOM tip. A metal coated tip with a nominal diameter of 200 nm was used. For adjustment the beam, sample, beam and tip are observed from the top with a microscope and camera.
- The fiber at the end of the NSOM tip is connected, collimated and fed into a visible avalanche photo diode from Perkin Elmer.

Scans:

The beam is focussed on the top surface of the sample in the area of an antenna array

The tip is adjusted to detect maximum intensity in the spot region

The piezo stage is used to scan the sample in the xy-plane. The tip remains at the same position relative to the beam spot, which scanned over the sample surface. Force feedback is applied to the tip in order to keep it at a constant distance from the sample surface.

Feedback adjustments are optimized for low topography sample surfaces, as is the case for this sample. This enables faster scans with less distance variations between the tip and surface.

Scan size were 5x5 or 10x10 μm^2

The resolution was kept constant at 128 points per 5 μm .

Purdue University setup

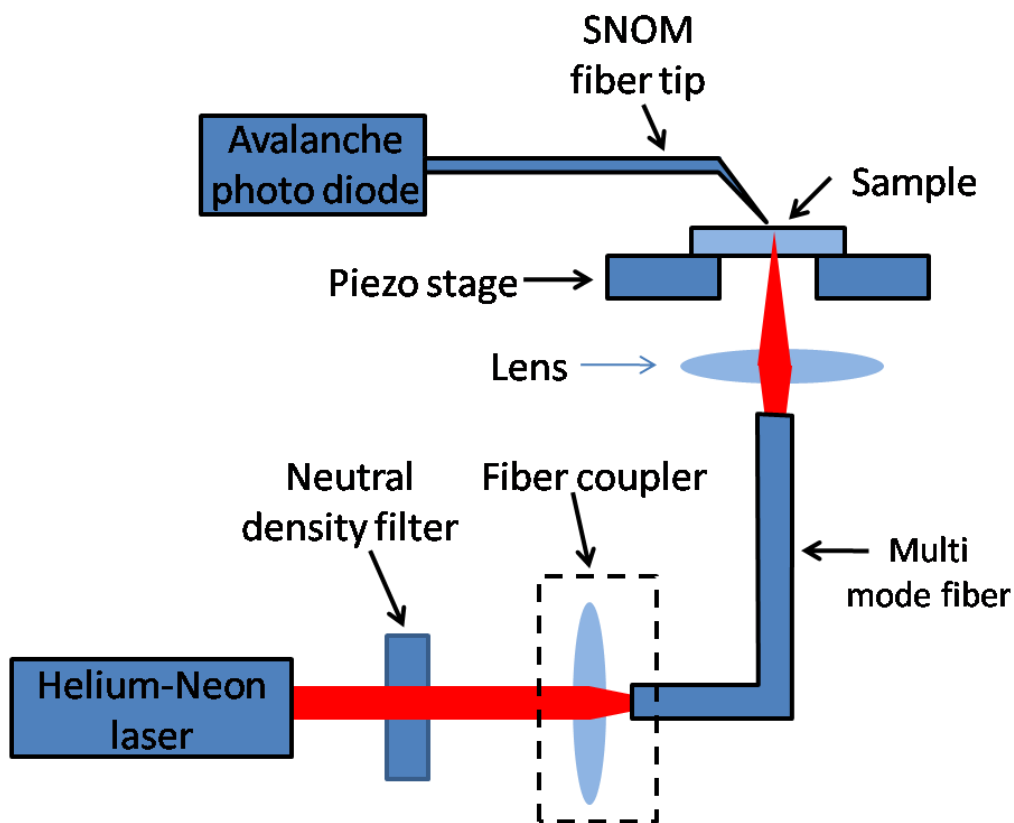


Figure 67 Schematic of the SNOM setup used at Erlangen University

Light from a 633-nm laser was coupled to a multimode fiber and fed into the lower microscope of the confocal Nanonics 2000 system. The laser light was coupled into the fiber with a 20x microscope objective, and it was coupled out of the fiber and focused through the sample with a 10x objective. Neutral density filters were used in combinations that gave consistent output readings on the avalanche APD with each sample.

During the scan, the sample was raster scanned while the fiber input and the NSOM tip remained stationary in the x-y plane, in order to avoid any intensity distribution associated with the beam profile.

The samples were scanned with the same NSOM tip in all cases. The tip was a non-coated, 150 nm diameter collection and transmission mode tip with a resonant frequency of about 45.49 kHz. All images were obtained in tapping mode with height (AFM) and NSOM intensity channels

for both trace and retrace scans. A significant shift between the NSOM and AFM data was observed, which can be attributed to the size of the tip.

The data was obtained at different scan sizes (5x5, 10x10 and 20x20 μm^2), in areas near the middle or at edge of the array.

All scans were taken with 256 or 512 points per line, giving either 256x256 pixels or 512x512 pixels per scan.

Due to the lack of wavelength or polarization control, the focus was on slow high-resolution scans.